FINITE ELEMENT BASED DESIGN AND OPTIMAL VIBRATION CONTROL OF SMART FIBER REINFORCED COMPOSITE SHELL STRUCTURES USING GENETIC ALGORITHM

A Thesis Submitted

in Partial Fulfillment of the Requirements

for the Degree of

DOCTOR OF PHILOSOPHY

by

Tarapada Roy

Under the guidance of

Dr Debabrata Chakraborty

Department of Mechanical Engineering

Indian Institute of Technology Guwahati

Guwahati-781 039, INDIA

March 2009

DEPARTMENT OF MECHANICAL ENGINEERING
INDIAN INSTITUTE OF TECHNOLOGY GUWAHATI
GUWAHATI-781 039

CERTIFICATE

It is certified that the work contained in the Thesis entitled "**Finite Element based Design and Optimal Vibration Control of Smart Fiber Reinforced Composite Shell Structures using Genetic Algorithm**" submitted by **Mr. Tarapada Roy** to Indian Institute of Technology Guwahati for the award of the degree of Doctor of Philosophy has been carried out under my supervision in the Department of Mechanical Engineering. This work has not been submitted elsewhere for the award of any other degree or diploma.

(Debabrata Chakraborty)
Professor
Department of Mechanical Engineering
Indian Institute of Technology Guwahati
Guwahati – 781 039

6th March, 2009

DEDICATION

The author wishes to dedicate this work

to his grandfather

Late Sri Mahananda Roy

ACKNOWLEDGEMENTS

This thesis is the result of four and half years of work during which I have been accompanied and supported by many people. I do consider it as a pleasant opportunity to express my gratitude to all of them.

I would like to express my heartfelt gratitude to Dr. Debabrata Chakraborty for his patient guidance and encouragement throughout my doctoral degree course. As my supervisor, his insight, observations and suggestions helped me to establish the overall direction of the research and contributed immensely to the success of the work. The research would not have been possible without his invaluable support, advice and encouragement.

I would like to thank my doctoral committee members, Prof. A. Dutta, Prof. S. K. Dwivedy and Prof. K.S.R.K. Murthy for their valuable discussions and help whenever I needed. I would like to render thanks to them for their much-needed feedback during my research work. I am also grateful to all the faculty members of Mechanical Engineering Department for giving me a comfortable and active environment for pursuing my research. I would also like to thank my friends Mr. Ramakrishna and Manikandan for their cooperation during the course of my Thesis work.

I am grateful to my family members, relatives and friends for their constant encouragement and moral support. I would like to offer my thanks to them for their affection, tolerance, support and endless encouragement for which I could consummate my work successfully.

At last but not least I am grateful to Indian Institute of Technology Guwahati for providing me financial support to carry out the present thesis work during my Ph.D. course.

6th March, 2009

Tarapada Roy

IIT Guwahati

ABSTRACT

Active vibration control of smart fiber reinforced polymer (FRP) composite structures finds use in high performance structures especially in lightweight composite structures. Proper implementation of such smart structure systems demands complete understanding of their responses and design of an appropriate control system. The present work deals with first development of an improved shell finite element (FE) formulation for coupled thermo-electro-mechanical analysis of smart FRP shell structures followed by development of genetic algorithm (GA) based methodologies for optimal actuators placement as well as optimal feedback controller. Stress resultant-type Koiter's shell theory has been used and no restriction has been imposed on the magnitude of curvature components to capture the deep and shallow shell cases. The twist curvature component has been incorporated along with the normal curvatures to keep the strain equations complete**.** The transverse shear effect has also been considered according to the Mindlin's hypothesis. An improved integer coded genetic algorithm (GA) based open loop procedure has been implemented for optimal placement of collocated sensors and actuators in order to maximize the controllability index incorporating control spillover. Once, the optimal sensor/actuator locations have been obtained, an improved real coded GA based linear quadratic regulator (LQR) control scheme has been developed for optimal vibration control of the smart shell structures under combined thermo-mechanical loading in order to maximize the closed loop damping ratio while keeping actuators voltages within limit. The FE formulations developed in the present work has been compared with analytical solutions for smart shell structures subjected to electrical, mechanical, thermal as well as combined electro-thermo-mechanical loading. It is observed that the developed FE could analyze coupled thermo-electro-mechanical of shell structures for both deep and shallow shells. Results obtained from the present work also show that this combined GA based optimal sensor/actuator placement and GA based LQR control scheme is far superior to conventional active vibration control using LQR control schemes. It is observed that the proposed GA based LQR control scheme along with the optimal placement of actuators could control both the dynamic oscillation due to mechanical load as well as the static displacement due to thermal gradient which was not possible with conventional LQR control scheme. The proposed GA based combined optimal placement and LQR control scheme not only lead to increased closed loop damping ratio but also shows a drastic reduction in input/actuation voltage.

TABLE OF CONTENTS

LIST OF FIGURES

Figures Page

Figures Page

Figures Page

LIST OF TABLES

NOMENCLATURES

A_1, A_2	Lame's parameters
$R_1,\ R_2$	Normal curvatures
R_{12}	Twist curvatures
α_1, α_2	Curvilinear coordinates
$\{d^e\}$	Elemental displacement vectors
$\{\varepsilon\}$	Strain components
E_z	Electric field
ϕ	Electrical potential
$\{\theta_t\}$	Vector of top and bottom surface temperatures
$\{F\}$	Global nodal forces
$\{G\}$	Global nodal charges
ω	Circular frequency
$\eta(t)$	Modal coordinates
$[\psi]$	Truncated modal matrix
$\{d_{com}\}$	Combined thermo-mechanical displacement
ξ_d	Damping ratio
n_a	Number of actuators
Ω	Measure of controllability for the optimal actuators location
$\{u_d\}$	Disturbance input vector
$\{y\}$	Sensors output vectors
f_c	Modal control force
γ'	Weight constant for optimal placement
$\eta_c,\ \eta_m$	Distribution indices for real coded GA

CHAPTER 1

Introduction

1.1 Smart structures

Increased use of fiber reinforced polymer (FRP) composite structures in aerospace and allied industries led to considerable interest in their analysis and design. These laminated composite structures exhibit high strength to weight and stiffness to weight ratios, which make them ideally suitable for use in weight sensitive structures, especially in space applications. Lightweight space structures however, inherently possess low internal damping, higher flexibility and are susceptible to large vibration with long decay time. These structures, thus require suitable integration of active control means to show better performance under operation. With the available of active materials and feasibility of embedding or bonding them to composite structures, new smart structural concepts have emerged to be attractive for potentially high performance structural applications. These structures are capable of sensing and reacting/actuating to their environment in a predictable and desired manner through the integration of various elements, such as sensors, actuators, power sources, signal processors, and communications network. The technological implications of this class of materials and structures have enormous applications such as structures that monitor their own health, process monitoring, vibration isolation and control, medical applications, damage detection, noise and shape control. These structures are called smart structures and it can be defined as a structure with bonded or embedded sensors and actuators as well as an associated control system, which is capable of sensing the undesired changes and taking remedial action to control the changes. Fig. 1.1 shows a schematic representation of a smart structure system.

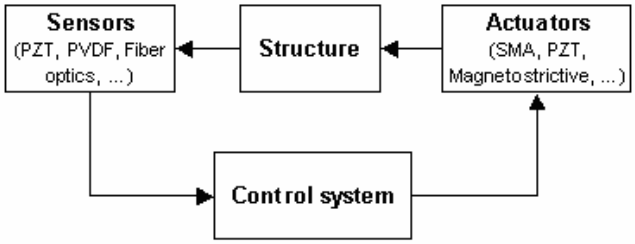

Fig.1.1 Smart structure schematic diagram

1.2 Smart materials

The best known among the smart materials are certainly the piezoelectric materials and more precisely the piezoceramics. However, several others are also available. Different types of smart materials used are described in the next few subsections.

1.2.1 Shape memory alloys

Shape memory alloys (SMA) are a class of materials exhibiting a shape memory effect. This is the effect by which a material, apparently plastically deformed, recovers its original undeformed shape after heating. SMAs utilize a solid–solid phase transformation. These alloys undergo a change in crystal structure from a cubic austenitic phase to a number of martensitic variants depending on the cooling or the application of stress. The reverse phase change occurs with increasing temperature and/or decreasing stress. The phase changes are accompanied by significant deformations, and a large actuation force can be generated.

1.2.2 Electro / magneto-strictive materials

Magnetostriction is the process by which a ferromagnetic material transforms from one shape to another in the presence of a magnetic field. Most ferromagnetic materials exhibit some measurable magnetostriction. Conversely, if an external force produces a strain in a magnetostrictive material, the material magnet state will change. This bi-directional magnetomechanical coupling of a magnetostrictive material provides a transduction capability that is used for actuation and sensing devices. This solid state phenomenon is a result of the rotation of small magnet domains causing internal stains in the material inducing an expansion in the field direction. As the field is increased, more domains tend to align with the magnetic field until magnetic saturation is achieved. If the field is reversed, the direction of the domains is also reversed but the strains still result in an expansion. These materials have improved stroke and force capabilities in comparison to piezoceramics but obtaining these parameters is more complex compared to that for piezoelectric or piezoceramic materials.

1.2.3 Electro / magneto-rheological fluids

Magnetorheological (MR) fluids and electro-rheological (ER) fluids are materials that respond at an applied magnetic or electric field with an important change in rheological behaviour. This is more of a semi-smart behaviour in the sense that the application of a third party field (here electric or magnetic) will act on a classical coupling (viscosity) and that there is no reciprocal effect. These fluids are non-colloidal suspension of polarisable small particles. Their essential characteristic is their ability to reversible change from a free-flowing, linear viscous liquid to a semi-solid with a controllable yield strength in milliseconds when exposed to a magnetic or electric field. In the absence of an applied field, controllable fluids are reasonably well approximated as Newtonian fluids. The magneto-rheological response results from the polarization induced in the suspended

particles by application of an external field. The interaction between the resulting induced dipoles causes particles to align and form chain-like structures parallel to the applied field. These chain-like structures restrict the motion of the fluid, thereby increasing its apparent viscosity. The mechanical energy needed to break these chain-like structures increases with the applied field.

1.2.4 Fiber optics

A fiber-optic sensor system consists of a fiber-optic cable connected to a remote sensor, or amplifier. The sensor emits, receives, and converts the light energy into an electrical signal. The cable is the mechanical component that transports the light into and out of areas that are either too space constrained or too hostile back to the sensor. Fiber-optic cable consists of a plastic or glass core surrounded by a layer of cladding material. The difference in densities between these two components enables the cables to act in accordance with the principle of total internal reflection.

1.3 Piezoelectric materials

With the growing applications of smart materials systems in innovative technical areas, the analysis of piezoelectric materials has received considerable attention in the recent years. The coupled electromechanical properties of piezoelectric materials and their availability in the form of thin sheets make them well suited for use as sensors and actuators. These lightweight materials under deformation generate an electric charge proportional to the strain field experienced by the material integrated over the coverage area. Conversely, these materials deform when supplied with an electric signal, generating forces and moments when bonded to existing structures.

The piezoelectric effect can be seen as transfers between electrical and mechanical energy. Such transfers can only occur if the material is composed of charged particles and can be polarized. For a material to exhibit anisotropic property such as piezoelectricity, its crystal structure must have no centre of symmetry. Twenty one crystal structures out of thirty two are non-centro symmetric. A crystal having no center of symmetry possesses one or more crystallographically unique directional axes. All twenty one non-centro symmetric crystal classes, except one, show piezoelectric effect along the direction axes. Out of the twenty piezoelectric classes, ten have only one unique direction axis. Such crystals are called polar crystal as they show spontaneous polarization. The value of this spontaneous polarization depends on temperature. This is called the pyroelectric effect. The pyroelectric crystals for which the magnitude and direction of the spontaneous polarization can be reversed by an external electric field are said to show ferroelectric behavior. Most of the

piezoelectric materials are crystalline solids. They can be single crystal either formed naturally or by synthetic processes, or polycrystalline materials like ferroelectric ceramics which can be rendered piezoelectric and given, on a macroscopic scale, a single crystal symmetry by the process of poling (by subjecting to a high electric field not far below the Curie temperature). Above a certain temperature, called the Curie temperature, the crystal structure of a ferroelectric material does have a centre of symmetry and has therefore no electric dipole moment. Below this temperature, it undergoes a phase change to a more complex structure which is non-centro symmetric. In this phase, the crystal presents a natural electric dipole (pyroelectricity), which may be reversed (ferroelectricity) and also switched in certain allowed directions by the application of a sufficiently high electric field.

The direct and converse piezoelectric effects govern the electromechanical interaction in these materials. In direct piezoelectric effect, when a mechanical force is applied to a piezoelectric material, an electrical voltage can be generated. The direct piezoelectric effect is used in sensor applications. The converse piezoelectric effect, on the other hand, produces a mechanical strain when a voltage is applied to the material and is used in actuator design. In sensor applications, mechanically or thermally induced deformations can be determined from measurement of the induced electrical potential (direct piezoelectric effect), whereas in actuator applications, deformations can be controlled through the introduction of appropriate electric potential (converse piezoelectric effect). By integrating distributed piezoelectric sensors/actuators and advanced composites, the potential exists for forming high specific strength and stiffness, lightweight structures capable of self-monitoring and self-controlling. But thermal effects such as temperature-induced deformation and the pyroelectric effect are especially important for many smart ceramic materials. A natural extension of the coupled electromechanical models is to also incorporate thermal effects. These coupled thermo-electro-mechanical models include temperature as an additional state variable to account for thermal effects in addition to the piezoelectric effects. Thermal effects become important when the piezoelectric structure has to operate in either extremely hot or cold temperature environments, e.g. in space applications. These extreme conditions may severely affect the response of piezoelectric structures in three distinct ways viz.

(i) induction of thermal stresses resulting from differences in the coefficients of thermal expansion

(ii) pyroelectric phenomena and

(iii) temperature dependence of the elastic, piezoelectric, and dielectric properties.

Pyroelectric effect is the generation of pyroelectricity as a result of a temperature change in a crystal. Pyroelectricity is the ability of certain materials to generate an electrical potential when they are heated or cooled. As a result of this change in temperature, positive and negative charges move to opposite ends through migration (i.e. the material becomes polarized) and hence, an electrical potential is established. Piezoelectric ceramics and piezoelectric polymers, which are extensively utilized in engineering, all belong to pyroelectric materials.

Piezoelectric materials have also a recoverable strain of 0.1% under electric field; they can be used as actuators as well as sensors. There are two broad classes of piezoelectric materials used in vibration control viz. ceramics and polymers. The piezoplymers are used mostly as sensors, because they require high voltages and they have a limited control authority. The best-known piezoplymer is the polyvinylidene fluoride (PVDF). Piezoceramics are used extensively as actuators and sensors, for a wide range of frequency including ultrasonic applications. They are well suited for high precision applications. The best-known piezoceramic is the Lead Zirconate Titanate (PZT).

1.4 Design analysis of smart fiber reinforced polymer (FRP) composite structures

The design process of a smart structure/system encompasses three main phases such as structural design, optimal placement of sensors and actuators and controller design and demands improved sensing and actuation both at the material and systems level. Figure 1.2 shows a schematic representation of a smart laminated composite structure having two thin patches of piezoelectric material bonded on the top and bottom surfaces of the base structure. One patch acts as sensor and the other as actuator. Signal from the sensor is used as a feedback reference in a closed–loop feedback control system. The control laws determine the feedback signal to be given to the actuator. In Figure 1.2, *F(t)* is the excited force, ϕ_s is the voltage generated by the sensor and ϕ_a is the voltage input to the actuator in order to control the displacement by developing effective control force.

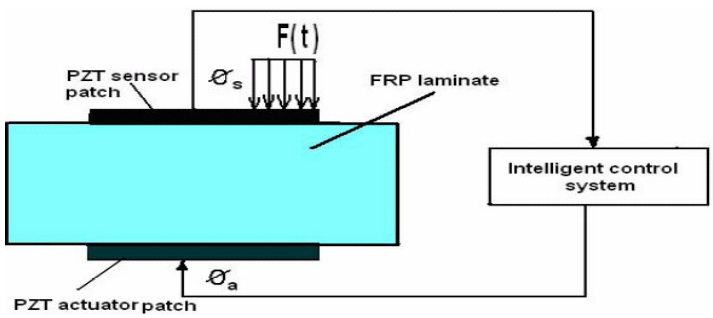

Fig. 1.2 PZT patches bonded to laminated composite with feedback control.

1.4.1 Analysis of smart FRP structures

The mathematical modeling of smart structures using piezoelectric layers/patches as distributed sensors and actuators requires a virtual overall model, which includes the main functional parts. In the analysis of piezo-laminated smart structures, the coupling issues associated with mechanical, electrical and thermal fields play an important role. Thermal effects, such as temperature-induced deformation and pyroelectric effect are also important for piezoelectric sensors and actuators. Finite element method (FEM) is a well known numerical tool for determining structural mass, stiffness, thermo-electro-mechanical coupling matrices and system eigenvalue and eigenvectors and have extensively been used for analysis of such smart structures. The plate/shell type structures are important in various applications. These are a particular form of a three dimensional solid. An enormous amount of effort has been devoted to the development of finite elements for the plate and shell analysis. There are many theories developed for the mechanical and electro-mechanical analysis of plates/shells. The importance of composite shell structures complexity leads to the use of finite element (FE) method. In the context of FE analysis, numerous elements have been proposed for the analysis of composite shell like structures. The generality of the shell formulation has been reduced in many of the situations to obtain better performance over a certain class of physical problems with greater accuracy and efficiency.

1.4.2 Optimal placement of sensors and actuators

The development of smart structures technology in recent years has provided numerous opportunities for active vibration control applications. The use of piezoelectric ceramics or films has shown great promise in the development of this technology. The use of piezoelectric material as actuators in vibration control is also beneficial because these actuators only excite the elastic modes of the structures without exciting the rigid body modes. This is important since very often only elastic motions of the structures need to be controlled. The continuous nature of structures allows one to choose where the piezoelectric patches are to be placed so that the performance and the efficacy of smart structures controlled is optimized. The locations of actuators also decide the input voltage requirement for desired damping effect. One can find locations of piezoelectric sensors and actuators on a structure where the controllability and observability measures of important modes are maximized. So, it is also important to have an optimization scheme for determination of optimal placement of sensors and actuators. Two basic approaches namely open loop and closed-loop are normally used for optimal placement of sensors and actuators. The open-loop procedure significantly simplifies the problem because the selection is performed

independently of any control law. In active vibration control of structures, only a few critical modes (lowest modes) are generally considered due to the computational overhead and modeling error. But the controller/actuator is likely to excite relatively higher critical modes, which will lead to control spillover. The control spillover is a significant problem of active vibration control implementation on real structures because it can lead to degradation as well as instability of the system response.

1.4.3 Control of smart structures

Undesired vibration is since ever a major problem in many structures and systems. The control of vibration can therefore be considered as one of the most relevant technological challenge. Vibration control of structures/systems can be achieved by passive and active damping methods. The passive approach requires the detailed understanding of structural dynamics and materials properties. The performance may be limited by the environment and choices of material, which reduce the vibration of structures/systems by simply dissipating energy as heat. Unfortunately their damping performance is generally quite poor because they are unable to adapt or retune to changing disturbance or structural characteristics, over time. On the other side, recent technological advancements such as the availability of high–power and low–cost computing, smart materials, and advanced control techniques have led to a growing use of active vibration control systems. It may offer better performance and adapt to different environments compared to passively damped structures. The implication of active control is that desirable performance characteristics can be achieved through flexible and intelligent strategies, whereby actuators excite the structure based on the structure's response measured by sensors. Control of structures involves a number of disciplines, including structural dynamics and control theory. The control of intelligent structures is performed by implementing various control methodologies. Different types of control strategies are available and generally, active vibration control can be performed by using two completely different strategies, namely feed forward control and feedback control.

1.4.3.1 Feedforward control

When a signal correlated to the disturbance is available, feedforward adaptative filtering constitutes an attractive alternative to feedback for disturbance rejection. It was originally developed for noise control, but it may be very efficient for vibration control too. Fig. 1.3 shows the schematic diagram explaining the principle of feed forward control.

Feed forward control relies on the availability of a reference signal correlated to the primary disturbance. This signal is passed through an adaptive filter, the output of which is applied to the system by secondary sources. The filter coefficients are adapted in such a way that the error signal at one or several critical points is minimized. The idea is to produce a secondary disturbance such that it cancels the effect of the primary disturbance at the location of the error sensor. Of course, there is no guarantee that the global response is also reduced at other locations and, unless the response is dominated by a single mode, there are places where the response can be amplified. This method, therefore, can be considered as a local one, in contrast to feedback control, which is global. Unlike active damping which can only attenuate the disturbances near the resonances, feedforward works for any frequency and attempts to cancel the disturbance completely by generating a secondary signal of opposite phase.

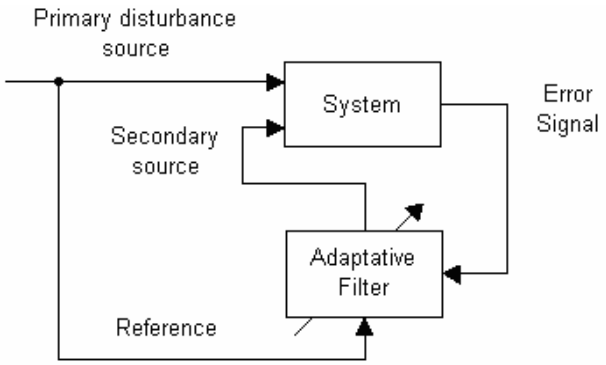

Fig.1.3 Principle of feedforward control

This method does not need a model of the system, but the adaptation procedure relies on the measured impulse response. This approach works better for narrow-band disturbances, but wide-band applications have also been reported. Because, it is less sensitive to phase lag compared to feedback, feedforward control can be used at higher frequency (a good rule of thumb is $w_c = w_s$ /10, where w_c and w_s are the bandwidth and sampling frequencies respectively) and that is why it has been so successful in acoustics. The main limitation of feed forward adaptive filtering is the availability of a reference signal correlated to the disturbance and other disadvantages of feedforward control principles are

i) it is effective only for near resonance

ii) limited bandthwidth ($w_c << w_s$)

iii) disturbances outside bandwidth are amplified and

iv) spillover

1.4.3.2 Feedback control

The principle of feedback control is presented in Fig. 1.4, the output y of the system is compared to the reference input r and the error signal, $e = r - y$, is passed into a compensator $H(s)$ and applied to the system $G(s)$. The design problem consists of finding

the appropriate compensator *H(s)* such that the closed-loop system is stable and behaves in the appropriate manner.

1.4.3.2.1 Classical feedback control

Classical control theory was naturally couched in the frequency domain and in the *s*-plane. A typical feedback control system consists of a sensor, which measures the response of a mechanical system to primary disturbances. The sensor signal is then fed via a controller back into the system by the secondary actuators. If the transfer function of the system, defined as the ratio of response amplitude to disturbance amplitude, is known, then the controller can be designed to improve the dynamic properties of the system.

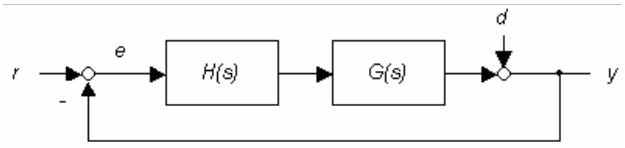

Fig.1.4 Principle of feedback control

The most obvious way to positively influence the dynamic behaviour is to locate the poles of the closed loop transfer function on the left side of the imaginary axis, which denotes a stable oscillation. This is equivalent to increasing the damping of the mechanical system. Many feedback control methods are available such as velocity, acceleration, positive position, and integral force feedback.

Classical control focuses on single input, single output (SISO) systems, but may become cumbersome when multiple input multiple output (MIMO) systems are to be considered. These methods impart a great deal of intuition and afford the controls designer with a range of design possibilities, so that the resulting control systems are not unique.

1.4.3.2.2 Modern feedback control

Rather than directly transforming the differential equation that describes the dynamic system into Laplace domain, the differential equation can be first described by internal state variables. The choice of the state variables is arbitrary, but for structural mechanics the second order differential equations are transformed into first order equations by choosing the deflections as well as their velocities as state variables. Theoretically, for continuous structures, an infinite number of state variables are required to describe the dynamics, which in practice is impossible. Even if the system is described by discrete quantities, the number of quantities required to obtain an accurate resolution is still too large be controlled. A way to overcome this deficiency is to perform modal decomposition of the structure and to describe the differential equation in terms of modal amplitudes.

Modern controls design is fundamentally a time-domain technique where a first-order vector differential equation representing an exact state space model of the system to be controlled. One may easily treat MIMO systems in state space representation. Optimal control problems, in which one chooses a control to minimize some cost functions (i.e total energy of the system), are formulated and solved in state space setting. Important system properties, such as "controllability" and "observability", are well defined in state space setting and the performance of the closed-loop system can also be attacked by investigating open-loop properties.

There are a many modern control techniques and one of these is optimal control theory. It is well known that the design of an optimal controller avoids the tasks of arbitrarily finding the gain of the controller to meet the design objectives and overcomes the problems of instability and actuator saturation. Linear Quadratic Regulator (LQR) is an optimal control method with the quadratic performance indexes and these indexes have specific physical concepts. At the same time, LQR has simple math disposal process and can achieve closed loop optimal control with the linear state feedback or output feedback. LQR has been applied in engineering widely. The cost function or performance index (function to be minimized) may be defined in a number of ways that can simultaneously include several performance-based criteria. Another important advantage of using the LQR is that it can be formulated for the case when the overall plant is described by a set of linear systems that span a particular range of operating conditions. The selection of weight matrices in LQR is very important and it straight affects the control effect. In general, the weight matrices are set by designers, who need to be familiar with the control system. The weight matrices are set by experience first and then are adjusted by simulation till obtaining the satisfying output responses. To this process, if the designer known poor about the system, the optimal weight matrices could not be obtained and so the control performances also could not be optimal. Linear Quadratic Gaussian (LQG) is another optimal control method. It concerns uncertain linear systems disturbed by additive white Gaussian noise, incomplete state information (i.e. not all the state variables are measured and available for feedback) also disturbed by additive white Gaussian noise and quadratic costs. Moreover the solution is unique and constitutes a linear dynamic feedback control law that is easily computed and implemented. The LQG controller is simply the combination of a Kalman filter i.e. a Linear-Quadratic Estimator (LQE) with a Linear-Quadratic Regulator (LQR). The separation principle guarantees that these can be designed and computed independently.

1.5 Optimization algorithms

There are many optimization techniques for solving engineering problems but the choice of an optimization strategy is crucial for successful solution of the problem. There are many important parameters such as the type of design variables (continuous, discrete or mixed), the type of objective function (smooth, non-smooth, differentiable, concave, convex, etc.), constrained or unconstrained problem, shape of feasible design space, the number of design variables, the number of constraints, cost of each evaluation, linear or nonlinear functions, availability of first-order and second-order derivatives, local and global optima, etc. Optimization algorithm can be divided into two classes.

1. Deterministic methods:

   These methods use function and/or gradient information to construct mathematical approximation of the functions, and then find an optimum point employing hill-climbing methods. These methods work normally with continuous design variables and need a small number of function evaluations, but they may not find a global optimum point.

2. Nondeterministic methods:

   The most common method in this class are random search, genetic algorithms (GAs), evolutionary programming (EP), evolution strategies (ES), simulated annealing (SA), and particle swarm optimization (PSO). These methods work entirely using only function values. These methods can work with discrete variables and find a global optimum in the presence several local optima. However, the number of function evaluations can be high even when global optimum is not found.

Genetic algorithms (GAs) have been extensively used in different fields as a means of doing global optimization in a simple yet reliable manner. GAs are adaptive methods and they are based on the genetic processes of biological organisms. Over many generations, natural populations evolve according to the principles of natural selection and survival of the fittest. By mimicking this process, genetic algorithms are able to evolve solutions to real world problems, if they have been suitably encoded. GAs work with a population of individuals, each representing a possible solution to a given problem. Each individual is assigned a fitness score according to how good a solution to the problem it is. The highly-fit individuals are given opportunities to reproduce, by cross breeding with other individuals in the population. This produces new individuals as offspring, which share some features taken from each parent. The least fit members of the population are less likely to get selected for reproduction, and so die out. A whole new population of possible solutions is thus produced

by selecting the best individuals from the current generation, and mating them to produce a new set of individuals. This new generation contains a higher proportion of the characteristics possessed by the good members of the previous generation. In this way, over many generations, good characteristics are spread throughout the population. By favouring the mating of the more fit individuals, the most promising areas of the search space are explored. If the GA has been designed well, the population will converge to an optimal solution to the problem.

1.6 Scope of the present work

Active vibration control of structures is aimed at reducing or modifying the undesired vibration level of structure/system. An efficient finite element procedure for coupled thermo-electro-mechanical analysis of FRP structures with piezoelectric sensors and actuators patches is very crucial in order to derive the system matrices those are required for designing active vibration control of such piezolaminated smart structure. It is a known fact that sensors and actuators placed inappropriately can lead to a loss of observability and controllability, which, in turn, may render the sensors and actuators ineffective. So the optimal placements of sensor/actuator on intelligent structures are important to improve control effect. Overall design of active (smart) structures represents a broad and complex field with many directions of development where, besides modeling and optimal placement, controller design for finding appropriate gain plays an important role. In view of this, the present work aims at

i) development of FE formulation for analysis and designing of smart FRP composite structures
ii) development of optimal placement scheme for sensors/actuators in FRP composite structures
iii) development of suitable optimal control scheme for active vibration control of such structures

1.7 Organization of the thesis

The present thesis has been organized as follows.

Chapter 1 discusses the brief introduction to smart FRP structures and significance of structural design, optimal placement and appropriate optimal control scheme of such structures. In order to understand the state of art in the broad field of active vibration control of smart structures a comprehensive literature review has been done and presented in chapter 2. Chapter 3 presents the development of an improved eight noded layered shell finite element formulation for piezo-thermo-elastic analysis of smart FRP laminated

composite shell structures with bonded piezoelectric sensors and actuators patches. Chapter 4 presents the details of the proposed GA based optimal sensors and actuators placement as well as LQR control scheme applied to smart FRP structures. Chapter 5 describes the validation of the integrated shell FE code and GA based optimal placement and control code, and also the study of influence of different important parameters on the thermo-electro-mechanical responses of such shell structures. Chapter 6 presents the results for optimal placement of collocated sensors and actuators in the different smart FRP laminated composite shell structures using integer coded GA and the superiority of the present method over existing methods. Chapter 7 presents the results of optimal vibration control of different types of smart shell structures under mechanical as well as thermo-mechanical loading using GA based LQR optimal control scheme and the superiority of the present method over conventional optimal control schemes. Chapter 8 concludes the thesis outlining the important conclusions drawn from the present work and it also discusses the scope for the future work.

CHAPTER 2

Literature Review

Smart materials and structures, intelligent structures are a new rapidly growing interdisciplinary technology embracing the fields of materials and structures, sensor and actuator systems and information processing and control. Rapid advances in each of these fields independently have been responsible for impact of this new interdisciplinary technology. Smart structure systems involve the synergism of materials with embedded or surface mounted sensors whose information is controlled and processed by intelligent system, which controls the actuator to perform the corrective action.

With the consolidation of composite materials for the construction of aerospace structures, enormous effort is currently being focused on the development of smart or intelligent structures. This technological development has created new avenues of research particularly in the areas of health monitoring, vibration and shape control of flexible structures, using distributed sensing and actuation by embedding piezoelectric materials in the host structure. Implementation of such FRP laminated smart structures demands complete understanding of behaviour of such structures subjected to loading, optimal placement of sensors and actuators in the structures and finally the design of an appropriate control algorithm for active vibration control of such structures. In this chapter, review of existing literature in the area of active vibration control of smart piezolaminated structures has been presented in three sections. First section discusses the reported research carried out on finite element (FE) modeling of piezolaminated structures. Second section presents the literatures published on optimal placement of piezoelectric sensors and actuators. The last one reviews the control schemes used for active vibration control of piezolaminated structures. Motivation and objective of the present work have been given at the end of this chapter.

2.1 FE modeling of piezolaminated structures

In the last two decades, one of the advances in material and structural engineering is in the field of smart structures that incorporates adaptive materials. Piezoelectric materials play an increasingly important role in smart technologies due to its inherent advantages over other smart materials. Some of the important works on piezoelectric materials are presented in the following paragraph.

The first generations of piezoelectric materials were crystals such as tourmaline, rochelle salt (tartaric acid) and quartz. The piezoelectric effects of quartz and some other materials were first demonstrated by Pierre and Jacques Curie [1] way back in year 1880. But the utility of piezoelectricity was not utilized till as late as 1918. In that year, Langevin type transducer was the first piezoelectric transducers. During the period between 1950 and 1970, Fukada [2] extensively studied the piezoelectric behavior and used them in transducers. The first applications appeared during the First World War with the sonar in which the piezoelectric quartz was used to produce the ultrasonic waves. The development of electronics, especially during the Second World War, and the discovery of ferroelectric ceramics increased the use of piezoelectric materials and the major breakthrough in the piezoelectric field came with the discovery of Polyvinylidene Fluoride (PVDF) by Kawai [3] in 1969. In late 1970's the application of PVDF was used in many transducer application e.g., Ultrasonic equipment, Sonar, strain gages, etc.

The use of piezoelectric materials as actuators and sensors for vibration and noise control of structures/systems has been demonstrated extensively over the past few years. Many articles concerning the use of different displacement models for the theoretical formulation of piezolaminated structures are found in the literature. There have been various mathematical models for pizeolaminated structures such as electro-mechanical models and piezo-thermo-elastic models, developed to describe the behavior of this type of structure. Some of the important works in the direction on FE modeling of piezolaminated structures are presented in the following subsections.

2.1.1 Electro-mechanical modeling

Some of the important works in the direction of coupled electro-mechanical analysis of piezolaminated structures are presented here. Allik and Hughes [4] proposed a tetrahedral volume element accounting for the piezoelectricity. Stating from Hamilton's principle, and the constitutive equations for piezoelectric media, a simple volume element (tetrahedron) having four nodes and four degrees of freedom per node (three translations and one electric potential) with a linear shape function was developed. Crawley and Luis [5] proposed an analytical model of the static interaction between a beam and segmented piezoelectric actuators, which were symmetrically bonded to the top and bottom surfaces of a beam. They used classical beam theory for the substrate.

Tzou and Tseng [6] analyzed smart beams, plates and shells based on a new finite element with internal degrees of freedom and demonstrated the applications to distributed

dynamic measurement and control of advanced structures. Lee [7] described theory of laminated piezoelectric plates with governing equations and reciprocal relations for the design of distributed sensors/actuators. Hwang and Park [8] proposed a pure bending rectangular plate element with a multilayered plate element having a single electrical degree of freedom per piezoelectric layer. This multilayer element had four nodes with three degrees of freedom per node (one translation and two rotations) and one electrical degree of freedom for each piezoelectric layer (voltage across the layer). This element however neglected the transverse shear and was therefore not suitable for modeling thick plates/shells and it also did not account for the extension, modeling only the bending behavior. Bimorph pointer was modeled numerically and the results were compared to an analytical solution and showed a good agreement.

Saravanos [9] presented a multilayer piezoelectric thin plate using the Kirchhoff-Love assumption (linear displacement field through the thickness) and bilinear shape functions. It had one electrical degree of freedom per piezoelectric layer, with an assumption of a constant electric field through the thickness for each layer. Abramovich and Pletner [10] studied the piezolaminated sandwich cantilever beam using CLT model. Faria and Muller [11] investigated static and frequency analyses of anisotropic cylindrical thin shells with one and two perfectly bonded ring piezoelectric actuators. They showed that the analysis was greatly simplified if the special relationship involving the membrane and the membrane-bending coupling stiffness matrices existed. In such a situation, simple closed form solutions of the equilibrium equations were obtained for the case of an infinite shell with one or two actuators. The authors performed the frequency analysis in a broad range to investigate the effect of mass properties on the response of a simply supported cylindrical shell. Yang [12] developed equations for the analysis of thick plates. The authors used CLT for displacement in piezoelectric layers and a quadratic variation of electric potential along the thickness of the actuators. Robbin and Reddy [13], Lee et al. [14], Agarwal et al. [15], Tiersten [16], Preiswerk and Venkatesh [17], Miller et al. [18], Yang [19, 20] and Tong et al. [21] and Lam and Ng [22] have also used CLT to model piezolaminated structures.

However, in most of the studies, the displacement field of the laminate was modeled according to CLT and the electric field in the piezoelectric layers was assumed to be constant in the thickness direction and orthogonal to the middle plane of the laminate. Ha et al. [23] developed an eight-node three-dimensional composite brick finite element for modelling the dynamic and static response of laminated structures containing piezoelectric

sensors and actuators. Ray et al. [24] presented the static analysis of simply supported piezolaminated plate by two-dimensional eight-noded quadratic quadrilateral isoparametric element. They considered distributed sensors and actuators layers made of piezoelectric polymer (PVDF) and a laminated substrate of a graphite/epoxy composite.

Suleman and Venkayya [25] and Suleman and Goncalves [26] proposed a four noded plate finite element using bilinear shape functions and the Mindlin assumption to accommodate thick as well as thin plates. Each node had five degrees of freedom (three translations and two rotations), the element had one additional electrical degree of freedom per piezoelectric layer (voltage across the thickness). Reduced integration scheme was used for the transverse shear stiffness to avoid the transverse shear locking phenomenon. Detwiler et al. [27] developed a finite element model to estimate the response of laminated composite plates containing distributed piezoceramic actuators and sensors. The finite element formulation was developed based on the QUAD 4 plate finite element used in COSMIC/NASTRAN and ASTROS. Two additional degrees of freedom per element were included in the QUAD 4 to represent the electrical voltages of two different piezoelectric layers. A cantilever bimorph beam was modeled numerically and the results were compared with theoretical solution showing a good agreement.

Some of the important works based on shell finite elements are presented here. Tzou and Ye [28] developed a piezoelectric triangular shell finite element using constant shear angle theory and studied a piezoelectric bimorph pointer and semicircular ring shell. The investigations on the natural frequencies and distributed control effects of the ring shell with piezoelectric actuators of various lengths suggested that the inherent piezoelectric effect had little effect on the natural frequencies of the ring shell. Piefort et al. [29] developed the theory of piezolaminated shells deriving fundamental equations governing the equivalent piezoelectric loads and sensor output. The reciprocity between piezoactuation and piezosensing was pointed out. Piezoelectric shell finite elements were developed based on Mindlin elements and different electrical boundary conditions were examined.

Chee et al. [30] developed a mathematical model for beams based on a higher order displacement field coupled with a layer wise linear electric potential. This model was developed using Hamilton's variational principle and was facilitated by the finite element formulation. The performance of the element was demonstrated by numerical investigations on the static analysis of a beam. Chen et al. [31] presented a finite element model of an eight noded shell element for modeling thin-shell structure containing integrated distributed

piezoelectric sensors and actuators. One electrical degree of freedom was used per node of an element and each node had six degrees of freedom (three translations, two rotations and one electric potential). Reduced integration technique was used to improve the performance of shell element. Sze and Yao [32] developed a number of finite element models for comprehensive modeling of smart structures with segmented piezoelectric sensing and actuating patches. These included an eight-noded solid-shell element for modeling homogeneous and laminated host structures as well as an eight-noded solid-shell and four-node piezoelectric membrane elements for modeling surface bonded piezoelectric sensing and actuating patches.

Benjeddou [33] presented a survey of different piezoelectric solid finite elements those have been developed over the years. Wan and Tao [34] presented design method for 1-3 anisotropy piezocomposite sensor to differentiate each strain component. Piefort and Premont [35] presented a general finite element formulation for piezoelectrically coupled systems. Piezoelectric finite elements were developed based on Mindlin shell elements and integrated in the FE package SAMCEF. Balagurugan and Narayanan [36] developed a piezoelectrically laminated nine noded quadrilateral shell finite element and applied to a semicircular shell with distributed layers of PZT sensor and actuator on the top and bottom surfaces. Mukherjee et al. [37] presented the active vibration control of stiffened plates. A stiffened plate finite element with piezoelectric effects was formulated. A nine noded assumed strain shell element formulation was modified and extended to solve for the behaviors of distributed actuators embedded thin cylindrical arch by Lee et al. [38].

Finite element modeling of degenerate shell element using higher order shear deformation theory considering distributed piezoelectric layers has been presented by Kulkarni and Bajoria [39]. A refined hybrid piezoelectric element formulation has been developed for vibration of laminated structures bonded to distributed piezoelectric sensors and actuators by Zheng et al. [40]. A finite element formulation using first-order shear deformation theory was introduced with an embedding technique for composite plate with distributed piezoelectric layer by Kusculuoglu and Royston [41]. They also used a combination of four-noded Lagrange bilinear and eight noded serendipity quadratic elements for deriving the matrices and vector necessary for approximating the solution.

Lentzen and Schmidt [42–45] developed a finite element code for the simulation of nonlinear vibration control of smart isotropic or composite laminated beams, plates and shells with integrated piezoelectric actuator and sensor layers based on a moderate rotation

first-order shear deformation model. Polit and Brant [46] developed piezoelectric eight noded plate finite element, where, electrical potential was approximated using layerwise approach. Two kinds of finite element approximations for the electric potential with respect to the thickness coordinate were presented viz. a linear variation and a quadratic variation in each layer. Balagurugan and Narayanan [47] presented a higher-order shear-flexible piezolaminated multi-layer smart composite plate finite element with 48 elastic degrees of freedom and 9 electric degrees of freedom per piezoelectric layer in the element. Lentzen et al. [48] presented geometrically nonlinear finite shell element incorporating piezoelectric layers. The finite element was implemented in a total Lagrangian approach and strain–displacement relations were based on the assumption of small strains and moderate rotations.

A new finite element model for elastic porous materials was introduced by Akl and Baz [49]. Sabbagh et al. [50] presented a finite element model and used along with an optimization algorithm that accounts for the periodicity constraint in order to determine the optimal topologies of plates with various periodic configurations. Static behavior of laminated composite spherical shell cap with distributed piezoelectric layers was investigated using eight noded degenerated isoparametric shell element based on first-order shear deformation theory by Ram and Kiran [51]. Marinković et al. [52] proposed a degenerate shell element and a simplified formulation that relied on small incremental steps for the geometric nonlinearity analysis of the piezoelectric composite structures. A nine-noded piezolaminated degenerated shell element for modeling and analysis of multi-layer composite structures with bonded/embedded distributed piezoelectric sensors and actuators was proposed by Balagurugan and Narayanan [53].

The shell type structures are known as the most desired structural elements in modern world. Numerous theoretical models have been developed, with the development of finite element method, for the electro-mechanical analysis of smart structures and applied to the various practical circumstances. Unfortunately, no single theory has been proven to be general and comprehensive enough for the entire range of applications for the electro-mechanical analysis of shells. There are number of important stress-resultant shell theories [54-60] available for thin elastic shells, in linear domain, based on the Love-kirchhoff assumptions, but each theory is different since it either neglects or approximates one or more terms. Amongst them, the Koiter's shell theory has been found to be satisfying the following necessary invariants i.e. strain equations remain invariant under transformation of

middle surface coordinates and also remain unaffected by any arbitrary rigid body motion. The constitutive relations have been found to be consistent with all conservation laws and equations resulting therefrom.

Recently, Sk and Sinha [61] developed the finite element model for the static and free vibration analysis of doubly curved, laminated composite shells. They used the stress resultant-type Koiter's shell theory and no restriction was imposed on the magnitude of curvature components to capture the deep and shallow shell cases. The transverse shear deformation was considered according to Mindlin's hypothesis. Five DOF (three translations and two rotations) were considered per node and twist and normal curvature components were incorporated to keep the strain equations complete. They reported this improved shell element yielded accurate results with a relatively smaller number of elements.

2.1.2 Piezo-thermo-elastic analysis

Modelling and analysis of adaptive piezothermoelastic laminated structures represent high level of sophistication and complexity. Recently, an increasing number of investigators have addressed piezothermoelasticity. Tauchert et al. [62] examined the response of laminated plate embedded with piezoelectric lamina to stationary thermal and electric loads using the classical lamination theory. They assumed temperature to be linearly distributed in the thickness direction. Jonnalagadda et al [63] developed the formulation to study the static response of composite plates constructed of graphite/epoxy laminae with an attached PVDF layer subjected to mechanical, thermal and electric field loading. They extended the first-order shear deformation theory to include the piezothermoelastic response of composite plate structures. Temperature variation was assumed to vary linearly in the thickness direction. Influences of temperature on piezoelectric sensors and actuators of beam-type precision devices have been studied based on a thin piezothermoelastic solid finite element by Tzou and Ye [64].

Xu and Noor [65] investigated the response of a laminated cylindrical shell to mechanical loading, temperature change and electric potential by three dimensional analytical solutions. A new three-dimensional thin hexahedron piezothermoelastic solid finite element with three internal degrees of freedom was formulated using a variational formulation by Tzou and Ye [66]. In their work, a system equation for the piezoelectric continuum exposed to combined elastic, electric and thermal fields was formulated. Distributed sensing equations were derived and pyroelectric and thermal strain effects of the

piezoelectric transducers of a laminated plate were investigated. Lee and Saravanos [67] derived a thermo piezoelectric multilayer beam element using linear shape functions along the beam and linear through the thickness of each layer (layerwise linear). A reduced integration scheme for the transverse shear stiffness was used and the element took into account the effect of constant thermal load (constant gradient of temperature). Shang et al. [68] studied the thermal buckling of a laminated piezoelectric plate with uniform temperature. Batra *et al* [69-70] dealt with shape and vibration control of plates at finite deformations, also taking into account nonlinear constitutive equations for piezoelectric patches.

A coupled thermo-piezoelectric-mechanical model of composite laminates with surface bonded piezoelectric actuators was developed by Chattopadhyay et al. [71] and Jingmei et al. [72]. Blandford et al. [73] developed a hierarchical finite element approximation of the governing equations using reduced material stiffness coefficient to study static response of beams. Beam displacement theory was based on Reissner-Mindlin shear deformation theory and the electric potential was assumed to vary linearly through each piezoelectric lamina. Temperature was assumed to vary linearly through the beam thickness. Fundamentals of piezothermoelasticity was reviewed first and followed by the development of a new piezothermoelastic triangle composite shell finite element including the temperature effect, extended from the piezoelastic triangular shell element by Ye and Tzou [74].

Among the investigations in piezothermoelasticity, the static and dynamic problems of different structures were discussed by Tauchert et al. [75]. A general solution for dynamic piezothermo-elastic problems of transversely isotropic piezoelectric materials was derived by Haojiang et al. [76]. Kim et al. [77] developed the coupled thermo-piezoelectric-mechanical theory, based on layerwise displacement field and higher order electrical and temperature fields, to study dynamic response and control of smart cylindrical composite shells. Altay and Do¨kmeci [78] formulated the fundamental equations of thermopiezoelectricity in variational form, and systematically derived the system of one-dimensional (1D) equations for the high-frequency vibrations of a cylindrical rod. Vel and Batra [79-80] developed a three-dimensional analytical solution in terms of an infinite series for the thermo-piezoelectric deformations of laminated thick plates with various support edges.

The numerical and experimental study of active compensation of thermal deformation of a composite beam using piezoelectric ceramic actuators was considered by Song et al. [81]. Altay and Do¨kmeci [82] modified the Mindlin's equations of thermopiezoelectricity, by introducing a thermal field vector, and obtained the consistency, both mathematically and physically, the universal gradient equations in thermopiezoelectricity. Liew et al. [83] investigated the behaviour of multilayered composite plates subject to thermo-piezoelectric-mechanical loading. The analysis was performed using the three-dimensional equations of thermo-piezoelasticity and the differential quadrature (DQ) numerical technique. Heidary and Eslami [84] outlined the equations governing the linear response of piezothermoelastic plate based on the Hamilton's principle and finite element methods. Newmark time marching method was use to solve the governing equations. Kumar et al. [85] presented the piezo-thermo-elastic model of cylindrical shell using nine noded degenerated shell element. They also studied the active vibration control of cylindrical panel under sudden change in temperature using simple negative feed back controller. Jiang and Li [86] recently developed a finite element model for piezothermoelastic composite beam considering higher order displacement field, higher order electrical field and linear temperature field. Two nodes Hermitian beam element was used. Constant-gain negative velocity feedback control approach was used for active vibration control of a beam.

2.2 Optimal placement of piezoelectric sensors and actuators

Vibration suppression performance in both active and passive damping decisively depends on the number, shape, size and location of the piezoelectric ceramic elements used as sensors and actuators [87, 88]. The same holds for shape control, vibroacoustic control and structural health monitoring. Depending on the complexity of the structure, analytic or numerical models might prove more appropriate to describe its behavior. A number of different objective functions, design variables, constraints and solution methods can be applied for the optimization of a target application. The following subsections reviews a representative portion of the work performed in the last decade towards the optimal placement of sensors and actuators for vibration suppression. The articles reviewed here have been classified based on the optimization algorithm used.

2.2.1 Parameter variation

Informal optimization consisting of parameter variation studies can deliver useful insight into the optimization task, in particular if the solution space can be explored with a

reasonable number of configurations. This is the case for simple structures such as beams. While investigating the multiple mode passive vibration suppression with piezoelectric materials and resonant shunts, Hollkamp [89] estimated the generalized electromechanical coupling coefficient of a pair of piezoelectric ceramic tiles attached to a cantilever beam at different locations. Kang *et al* [90] optimized the placement of piezoelectric collocated sensor/actuator pairs for active vibration control of laminated beams by maximizing the structural damping index, a weighted sum of the achieved modal damping of each vibrational mode. Parametric studies were presented for the damping ratio as a function of the location of piezoelectric ceramic elements with given length and various outer-layer fiber orientations. Vibration suppression analysis of cantilever beam with piezoelectric sensors/actuators subjected to an exciting force has been performed by Zhang and Kirpitchenko [91]. They considered two sets of surface bonded piezoelectric patches with three locations of patches and experimentally showed that the damping of combined beam-piezoelectric patches system increased by 8-10 times in comparison to that of mechanical system. Formal optimization techniques, on the other hand, can be classified into deterministic methods and stochastic methods.

2.2.2 Deterministic methods

Most mathematical programming methods work locally and are very efficient given that the assumptions on continuity, differentiability and convexity of the solution space are satisfied. Aside from the convexity assumption, this is mostly the case for basic structures such as beams and plates. Classical beam and plate structural models were used to derive cost functions for determining the optimum placement and thickness of embedded and surface mounted piezoactuators by Main et al [92]. An optimization procedure was used to develop a design guide for simplified determination of piezoactuator size and placement. Li *et al* [93] presented an optimal design methodology for piezoelectric ceramic actuators/sensors and feedback gains towards the vibration suppression in flexible structures and studied the influence of the actuator/sensor pairs on the mass and stiffness properties of the composite structure. The proposed composite objective function included the control performance as well as the added mass.

However, the gradient based optimization methods applied to the simple case of a beam structure, was prone to getting trapped in local optima. Kang *et al* [94] carried out an investigation on laminated plates where the optimization was carried out using the gradient method. Haramoto et al [95] presented the optimal placement of two pairs of sensors and

actuators in order to maximize the H_2 norm of the closed loop system for a simply supported beam using quasi-Newton method. Mukherjee and Joshi [96] obtained the actuator layout by minimizing the power consumption in order to achieve a specified displacement of plate structure using iterative procedure. Wang and Wang [97] proposed a controllability index for optimal locations and size of piezoelectric actuators for the beam model in order to maximize modal control forces and reported that higher the controllability index, the smaller would be the electrical potential required for active control. However, they did not consider control spillover of the higher order modes, which would give closed loop instability by maximizing modal control forces of the higher order modes. Seeger and Gabbert [98] proposed an optimization algorithm for the optimal positioning of collocated actuator/sensor patch pairs on a simply supported plate structure. Conjugate gradient method was applied to minimize the H_2-norm of the transfer function between an external excitation disturbance and the plate vibration amplitude. The constrained optimization algorithm used the augmented Lagrangian function in order to avoid patch overlapping.

The quasi-modal sensor and quasi-modal actuator were developed for finding optimal placement and sizes of sensors and actuator on rectangular plate by Sun *et al* [99]. Sun and Tong [100] extended the investigation to simply supported closed- and open-form cylindrical shell structures. An energy based approach for optimal positioning of piezoelectric actuators and sensors on a flexible structure was presented by Leleu et al. [101]. First, a two-dimensional (2–D) model of a piezoelectric actuator bonded to a plate was obtained and then, a Ritz formulation was used to find a state model of the system in view of its control.

Selection process for piezoelectric transducers (PZT) used as actuator elements for suppressing vibrations in a flexible beam system was discussed by Kermani et al. [102]. The effects of changing physical parameters such as the relative thickness of the piezoelectric ceramic with respect to the beam, the optimum location of the PZT actuator, and the length of the PZTs were studied based on the singular value decomposition of the controllability Grammian of the resulting system. Modal based correction methods were applied by Rose [103] for the placement of piezoelectric ceramic modules on a circular plate. These methods allow the negotiation of changes introduced by the piezoelectric element's mass and stiffness. Generalized electromechanical coupling coefficient was maximized by applying gradient-based methods in a two-step approach. Halim and Moheimani [104] suggested a criterion for the optimal placement of collocated piezoelectric ceramic actuator/sensor pairs

on a thin plate using modal and spatial controllability. The spatial controllability was used to find the optimal placement of collocated actuator/sensor pairs for effective average vibration reduction over the entire structure, while maintaining modal controllability and observability of selected vibration modes.

Sun and Tong [105] presented an investigation into design optimization of actuator patterns for static shape control of composite plates with piezoelectric actuator patches. An energy optimization based method for finding the optimal control voltages that can actuate a structure shape close to the desired one within a given error was described. Emilio et al. [106] proposed a simultaneous search for an optimal topology of a flexible structure as well as the optimal position of the piezoceramic in the design. The method was implemented based on the SIMP ('Solid Isotropic Material with Penalization') material model and the examples presented were limited to two-dimensional models.

2.2.3 Stochastic methods

Engineering design problems, are often of a discrete nature (e.g. the number of actuators), so that the above methods described in the previous subsection are not applicable or tend to get trapped in local optima. In order to overcome these limitations, the scientific community has put significant effort into the investigation of stochastic optimization methods. Stochastic optimization methods can handle search spaces involving both discrete and continuous domains, non-convex objective functions, and objective functions or constraints lacking differentiability. A drawback is that stochastic search methods are often computationally expensive.

Genetic algorithm (GA) has been extensively used for optimization of engineering problems in recent times and some of the important works in this direction are described here. Rao *et al* [107] were the first to apply genetic algorithms to the problem of optimal actuators placement in an actively controlled two-bay truss. The dissipation energy of the active controller was maximized for a fixed number of three actuators. A strategy for determining the optimal number of actuators and their respective locations in the active vibration control of a 72-bar space truss was presented by Yan and Yam [108] where the eigenvalues of the energy correlative matrix of the input control force were used to determine an optimal number of actuators for vibration control. They reported that depending on the desired controllability level, these can be equal to or less than the number of degrees of freedom to be controlled. Using a binary-encoded genetic algorithm, Bishop and Striz [109] demonstrated the optimal placement of passive ideal viscous dampers on

space trusses subjected to different loading. The kinetic and strain energy remaining in a system at the end of a full time-domain transient analysis, as well as the number of actuators, were combined to form a penalty function.

Abdullah et al. [110] used genetic algorithm to simultaneously place collocated sensor/actuator pairs in multi-storey building while using output feedback as the control law in terms of minimizing the quadratic performance i.e. weighted energy of the system. They found optimal gain using Davidon-Fletcher-Powell gradient-based optimization algorithm by choosing weighting matrices [Q] and [R] using trial and error and concluded that the decision variables in this optimization problem were greatly dependent on the selection of weighting matrices. They also used binary coded GA with the length of the gene string as the number of floors in multi-storey building, which led to large number of function evaluations and large number of generations to reach near optimal solution. Richardson and Abdullah [111] used a real-encoded genetic algorithm for optimal placement of sensors and active tendon mechanisms on high-rise civil structures which were susceptible to vibrations due to earthquakes, hurricanes or other abnormal loads such as explosions. The proposed method allowed for the simultaneous determination of the optimal controller gains. However, real-encoded genetic algorithm is more suitable for continuous search space where structural responses are obtained analytically. Results by Gaudenzi *et al* [112] provided insight into the problem of optimal placement, sizing and loading of piezoelectric actuators for damping beam vibrations. A fundamental solution, formulated for a single piezoelectric actuator pair, was used in the framework of a genetic algorithm optimization.

A float-encoded genetic algorithm for the integrated optimization of piezoelectric actuator and sensor locations and feedback gains for active vibration control was introduced by Zhang *et al* [113] and concluded that the float-encoded genetic algorithm was less likely to become trapped in local minima compared to the adaptive binary genetic algorithm and converged faster to the solution. A cantilever beam was presented as an optimization example, for which the performance function is based on maximizing the dissipation energy of the active controller. However, float-encoded genetic algorithm was also appropriate for continuous search space. A similar problem was tackled by Yang *et al* [114] and they presented a simultaneous optimization method considering several design variables such as placement of collocated piezoelectric sensors/actuators, size of sensor/actuator and feedback control gain for vibration suppression of simply supported beam by minimizing the equivalent total mechanical energy of the system. However, they did not consider input

energy in the used objective function i.e. equivalent total mechanical energy. This type of chromosome representation used will not be feasible for multi input system with more sensors and actuators and it will also lead to more trial and error to impose bound for the entire feedback control gain matrix elements. The same authors later extended the method cited above to the investigation of plates and cylindrical shells [115] with dynamic constraints, included directly in the modified real-encoded genetic algorithm, and penalizes overlapping piezoelectric patches.

Binary coded genetic algorithms based on the open loop performance were used by Han and Lee [116] to find efficient locations for six sensors and two actuators out of 99 possible sub-areas on a cantilever composite plate. Two criteria for the optimal placement of piezoelectric actuators for vibration control were suggested by Sadri *et al* [117] using modal controllability and the controllability Grammian. The number of actuators, their sizes and their optimal locations for maximum controllability of isotropic plates were determined using genetic algorithms. They used Gray coded genetic algorithm to find the eight coordinates of two piezoelectric actuators in a simply supported plate based on the open loop performance. However, this type of Gray coded GA leads to increased string length. The authors later applied the modal controllability as a criterion for optimal placement of piezoelectric actuators for panel flutter suppression [118].

Quek *et al* [119] used the classical direct pattern search method to maximize the active damping of a laminated composite plate. The starting point for the pattern search was selected based on the maxima of integrated normal strains consistent with the size of the collocated piezoelectric sensor/actuator pair used. Optimization performance indices were based on modal and system controllability. Guo et al. [120] presented a sensor placement optimization performance index based on the damage detection in the two dimensional truss structures using binary coded genetic algorithm. Li et al. [121] proposed two level genetic algorithms (TLGA) for optimal placement of active tendon actuators in multi storey building by minimizing the maximum top floor displacement. This proposed TLGA might be feasible for this type of optimization problem and for active vibration control of large-scale structures with complete electromechanical analysis considering PZT sensors/actuators but this will not be computationally feasible because there will more possible actuators locations. The positions of four piezoelectric patches for adaptive feed-forward control were chosen out of 64 candidate locations on a cantilever aluminum plate by [122] and concluded that the maximization of the controllability Grammian through a

genetic algorithm guaranteed a minimum control force for minimizing the vibration response at three selected points of the plate.

Wang *et al* [123] addressed the topology optimization of collocated sensors/ actuators pairs for torsional vibration control of a laminated composite cantilever plate using output feedback control. They used binary coded genetic algorithm for optimization, which was not computationally efficient for actuator/sensor location in terms of number of function evaluations, and generations for convergence. Liu et al. [124] used a spatial H_2 norm of the closed loop transfer matrix for finding the optimal nodal points for sensing displacement and applying actuation for the control of a fixed-fixed plate. This method did not address a complete coupled electromechanical analysis and used binary coded genetic algorithm leading to very large number of generations for convergence. Optimal placements and sizes of sensors and actuators attached to an inflated torus were found by Jha and Inman [125] using a binary encoded genetic algorithm. Performance indices were defined using modal controllability (minimum energy requirement) and observability (maximum output energy for a good signal to-noise ratio). Belloli and Ermanni [126] presented optimum placement of piezoelectric ceramic elements for vibration suppression of rear wing of a race car. The optimization procedure included a knowledge-based CAD model, an FE model and an evolutionary algorithm optimization loop controlled by the proprietary software tool DynOPS.

2.3 Control schemes for active vibration control

Vibration control of structures/systems is essential to achieve optimal design with desirable performance. Passive damping treatments have been used extensively in many structural systems to reduce vibration response. Once the damping treatments are installed, the damping cannot be adjusted. Recently, active damping control has received increasing attention of its ability to provide adjustable and significant damping that traditional passive damping treatments cannot.

The recent advances in digital signal processing and sensors and actuators technology have prompted interest in active vibration control [127–132]. In the past two decades, various strategies to actively control the vibrations of structures with piezoelectric layers/patches acting as sensors or actuators have been applied. The different algorithms utilized in active vibration control can be classified under two general categories: feedforward and feedback control. Variations of the two general methods exist, each with advantages, disadvantages and limitations. An analytical and experimental study utilizing

classical and optimal feedback control techniques for the vibration control of beams and plates was performed by Han et al. [133]. A review about the active structural vibration control was presented by Alkhatib and Golnaraghi [134]. Together with examples of their applications, various topics was briefly introduced, such as feedback control, feedforward control, controllability and observability, spillover, eigenstructure assignment (pole placement), coordinate coupling control, robust control, optimal control and state observers (estimators).

Recently, optimal feedback control techniques such as Linear Quadratic Regulator (LQR) and Linear Quadratic Gaussian (LQG) have vividly been studied due to the generality and stability guaranteed properties and good performance. Some of the important works in the direction of optimal feedback control using LQR and LQG are presented in the following paragraph. Chen and Dong [135] employed a robust LQG optimal control design technique to stochastic linear dynamic system with uncertain parametric perturbations and noise covariance. Ray [136] obtained a closed-form solution for the optimal control of vibrations of a simply supported symmetric thin laminated plate integrated with piezoelectric layers. Alam *et al*. [137] presented an active control scheme for the control of galloping related vibrations in the long span of bridge tower. The Kalman filter technique was used for the state variable estimation. In the approach, the covariance of error vector between the model state vector and the actual state vector was minimized through a filtering process.

Moore *et al.* [138] studied LQG models where the stochastic models depended both on the states and the controls, and the measurements were bilinear in the noise and states/controls. Chen *et al.* [139] presented a new smart structure optimal design strategy applied to robust vibration control of a piezoelectric laminate beam. The optimization of the smart material layout and the control law were performed simultaneously to extract maximum performance from the system. A homogenization approach was used to allocate sensor material, while a LQR was used for the control law. The method was applied to a pinned–pinned beam where two cost functions were considered, both focusing on increasing the stability margin of the closed-loop system. The first was based on the observability gramian and the second on the control weighting parameter of the LQR cost function. Trindade *et al*. [140] designed and analyzed the piezoelectric active control of damped sandwich beams. The control design and performance were evaluated using three control algorithms applied to the reduced order model, namely LQR, LQG and derivative feedback.

It was shown that, in optimal hybrid configuration, the LQR algorithm improved the first modal damping while retaining the passive damping of the remaining modes, even uncontrolled ones. Derivative feedback controller was less effective in optimal geometrical configuration compared to LQR controller. In LQG algorithm, the control parameterization, robustness and performance of the LQR could be obtained while measuring only the output instead of all state variables.

Bhattacharya *et al.* [141] developed shell element and considered the shear deformation effects and they used LQR strategy for vibration suppression of spherical shells made of laminated composites by trial and error selection of [*Q*] and [*R*] matrices. Ang et al. [142] proposed the use of total weighted energy method to select the weighting matrices. Sadri *et al*. [143] presented theoretical modelling of active flutter suppression of plate components of an aerospace structure. The investigation of performance of LQG was carried out for various Mach numbers using the developed model. Results showed the suitability of LQG design and optimization approach. Balamurugan and Narayanan [144] worked with the active vibration control of beams with smart constrained layer damping (SCLD) treatment. Using LQR optimal control, the effects of SCLD on vibration suppression performance and control effort requirements were investigated.

Petersen and Pota [145] presented a practical robust controller design methodology based on theoretical results on minimax LQG control. The controller design methodology was illustrated with the design of a robust feedback controller for the control of vibrations in a flexible cantilever beam. The minimax LQG control approach was used to design a controller which minimized the total vibration energy of the beam subjected to white noise disturbances. The results indicated minimax LQG methodology combined with the spatial LQG approach led to a useful controller design methodology for the design of robust controllers for flexible structures.

Narayanan and Balamurugan [146] again presented a finite element modeling of laminated structures with distributed piezoelectric sensor and actuator layers and control electronics. Lyapunav feedback as well as LQR approach by trial and error selection of [*Q*] and [*R*] matrices was used for active vibration control. They reported that LQR approach was found to be more effective in vibration control with lesser peak voltages applied in the piezo actuator layers as in this case the control gains were obtained by minimizing a performance index. Chen *et al.* [147] introduced a new smart structure optimal design strategy and applied to robust vibration control of a piezoelectric laminate beam. The

optimization of smart material lay out and the control law was performed simultaneously to extract maximum performance from the system. A homogenization approach was used to allocate sensor material while a LQR was used for the control law. To demonstrate the advantages of the optimal control design, LQG control approach and an experimental study were conducted.

Chandiramani et al. [148] presented optimal vibration control of a rotating composite blade. A modified Galerkin method using admissible functions was considered and the optimal control problem was studied via the classical and instantaneous LQR methods. Stavroulakis *et al.* [149] presented the design of a vibration control mechanism for a beam with bonded piezoelectric sensors and actuators. LQR control strategy was considered and was observed to be effective for the vibration control of the structure. Moon and Hwang [150] employed LQR to suppress the flutter of a supersonic composite panel using piezoelectric actuators. The study showed that the controller based on the nonlinear model could produce a rapid and complete suppression of flutter motions with a lower control input as compared to a controller based on linear model.

Kumar *et al*. [151] presented experimental adaptive identification and control of a smart structure featuring piezoelectric based sensors/actuators. An inverted L structure with surface bonded piezoseramic sensors/actuators was used for analysis, and the state-space presentation with control input voltages to output sensor voltage, was established in multivariable form. A multi-input multi-output (MIMO) LQR was designed for an unique canonical form. A thorough study was done to see the effect of updated system parameters and control gains. A pair of interdigital electrode (IDE) piezoceramics was used to simultaneously suppress multimode vibrations of a cantilever beam by Park and Baz [152]. Moon [153] presented a general finite element formulation for LQR optimal control scheme with output feedback. The scheme was used for nonlinear flutter suppression of a composite panel with piezoelectric actuators and sensors. They reported that LQR with output feedback gave a simple and practical implementation.

Vasquess and Rodrigues [154] presented a numerical study concerning the active vibration control of smart piezoelectric beams. A comparison between the classical control strategies, constant gain and the amplitude velocity feedback, and optimal control strategies such as LQR and LQG controller, was performed in order to investigate their effectiveness to suppress vibrations in beams with piezoelectric patches acting as sensors and actuators.

Wang *et al.* [155] presented the application of methods for active control of vibration of a plate-like structure with discontinuous boundary conditions.

Modal LQG optimal control method was used to determine controller gains for each sensor/actuator pair. Good agreement between simulated and experimental results was obtained. Hsiao *et al*. [156] considered an LQG optimal problem and employed Minimax theory and Bellman-Gronwall lemma to derive a robust criterion which guaranteed the asymptotic stability of the discrete time delay systems under both parametric uncertainties and uncertain noise covariances. On the basis of this criterion, a robust minimax controller composed of Kalman filter and the optimal regulator (LQR) was synthesized to stabilize the uncertain stochastic systems. King *et al.* [157] investigated and compared LQG balanced truncation with Minimax control design to the distributed parameter system.

Zarei *et al*. [158] designed and compared LQG/LTR and H_∞ methods for robust stability margins and good performances in step response of a Vertical Short Take-off and Landing (VSTOL) aircraft system. It was observed that both controllers had good stability margin in the output of the system. Ho and Ma [159] provided an active control method based on LQG and input estimation approach. The simulation demonstrated better control performance of the method for structures than that of conventional LQG approach.

2.4. Motivation and objectives of the present work

Even though many works have been reported in the broad area of active vibration control of smart structures, there are still scopes and need for improvement in better understanding of behavior of smart shell structures especially under thermo-mechanical loading as well as achieving better actuation and superior control performance of such structures. From the exhaustive literature review, the following important observations have been made.

i) A large number of works are available in the form of beam and plate finite elements for analysis of piezo-laminated smart FRP structures, not many works are available in the form of shell finite element for such structures. There are few literatures available which also did not consider the complete electro-thermo-mechanical analysis of smart shell structures.

ii) Many existing literatures in optimal placement of sensors/actuators have used GA but they require large number of generations and function evaluations for reaching near optimal solution. Most of them did not consider control spillover of higher modes.

iii) Most of the existing literatures have used LQR and LQG control schemes for optimal vibration control of smart structures where weighting matrices have been selected by trial

and error method even though choice of weighting matrices decides the optimal gain. Moreover, in most of these cases control was done under mechanical loading only and not under combined thermo-mechanical loading.

Keeping the above points in mind, the specific objectives of the present thesis have been laid down as

i) Development of a shell finite element capable of analysis coupled electro-thermo-mechanical responses of smart FRP shell (both deep and shallow) structures

ii) Study the influences of important parameters on the electro-mechanical responses of smart FRP shell structures for different types of shells

iii) Development of an improved GA based optimal placement scheme for achieving better controllability of such structures

iv) Development of an improved GA based LQR control scheme for superior control performance under thermo-mechanical loading of smart FRP shell structures based on the responses from finite element analysis

v) Study of influences of different placement schemes on the control performance of such structures

vi) Conjunction of developed shell finite element code along with GA based optimal placement and optimal LQR control code to obtain a complete module for analysis and design of active vibration control of smart FRP composite shell structures.

CHAPTER 3

Finite Element Formulation of Smart FRP Composite Shell Structures

This chapter presents the development of an improved eight-nodded layered shell finite element formulation for piezothemoelastic analysis of different FRP laminated composite shell structures with bonded piezoelectric sensors and actuators patches. Electro-mechanical, electro-thermal and thermo-mechanical couplings have been incorporated in this shell element formulation. Stress resultant-type Koiter's shell theory has been used and no restriction has been imposed on the magnitude of curvature components to capture the deep and shallow shell cases. The twist curvature component has been incorporated along with the normal curvatures to keep the strain equations complete**.** The transverse shear effect has also been considered according to the Mindlin's hypothesis [61].

3.1 Finite element method (FEM)

Finite element method has become one of the universally adopted numerical method for the analysis of general structural and continuum problems. This is an approximate method in which the structure or the continuum is divided into number of small elements of various shapes, sizes and types, which are then, assembled together using compatibility of displacement and equilibrium of forces to form an approximate mathematical model. This method is used extensively in aerospace, automobile, civil, naval and other applications.

The plate/shell type structures are important in various applications. These are a particular form of a three dimensional solid. The thickness of such structures is very small when compared to other dimensions and complete three-dimensional treatment is not only costly but often leads to serious numerical ill-conditioning problems. Although the finite element analysis of plate and shell structures now span over more than forty years, the establishment of reliable and efficient finite element models still continues to be the subject of research effort.

An enormous amount of effort has been devoted to the development of finite elements for the analysis of plate and shell type structures. There are many theories developed for the mechanical analysis of plates/shells, but there is no effective general shell theory developed for the better modeling of shell structure. The modeling of plates and shells in the linear and nonlinear regimes including their application to dynamic analysis of structures has also grown extensively. Finite element method has been extensively used for

analysis of composite shell structures. Numerous elements have been proposed for the analysis of composite shell like structures. Unfortunately, no single theory has proven to be general and comprehensive enough for the entire range of applications. The generality of the shell formulation has been reduced in many of the situations to obtain better performance over a certain class of physical problems with greater accuracy and efficiency.

3.2 Classical shell theories (CST)

The behavior for deformations of shell structures in general, is rather complex because of the interaction between bending and stretching/membrane in carrying the applied loads. In the beginning of the 20th century, most of the attention was devoted to general problems of satisfying hypothesis and simplifying assumptions in formulating this portion of the mathematical theory of elasticity. Love [60] was one the first to reach the conclusion of possible representation of shell deformation energy in the form of two quadratic functions, describing the membrane deformations and bending of mean shell surface, as well as the possibility of the adopting simplifications similar to those suggested by Kirchhoff [160] in developing plate theory. Latter on, the accuracy of the so called Kirchhoff-Love shell theory was investigated by a large group of scientists, and its contemporary state has been largely influenced by ideas of Vlasov [161], Galimov [162], Koiter [163], and Mushtari and Galimov [164]. Since, in these theories the deformation energy is completely determined in terms of the deformation of the reference surface considering three-dimensional elasticity solution, its basic statements are valid for both the linear and nonlinear statements. These shell theories are known as classical shell theories (CST).

3.3 Classical lamination theory (CLT) and Mindlin's hypothesis

Most of the laminated structures have been modeled using classical lamination theory (CLT). The classical lamination theory however, totally ignores the transverse shear deformation and can be better applied to the thin structures (e.g. beams, plates, and shells) and to the structures made of materials having low ratio of elastic moduli to shear moduli, because these structures are not susceptible to thickness effects. But the thick structures and the laminated plates and shells made of advanced filamentary composite materials are susceptible to thickness effects. This is because, in case of such structures, the transverse shear strain is significant and cannot be neglected and for the structure made of advanced filamentary composite materials, the ratios of elastic moduli to shear moduli are very high (i.e. of the order 25-40 compared to 2.6 for isotropic materials). For these structures,

therefore, the transverse shear deformation plays a very important role in reducing the effective flexural stiffness. Therefore, modeling of these structures using CLT leads to the underestimation of deflections and overestimation of natural frequencies. Due to these aspects, it is desirable to consider the effect of shear deformation in the modeling and analysis of such structures.

In this work, effect of shear deformation has been considered according to Mindlin's hypothesis, which is known as the first order shear deformation theory (FOST) or Constant Shear Angle Theory. In this theory, Mindlin relaxed the assumption made in Kirchhoff theory and assumed that a line originally straight and normal to undeformed mid plane remains straight, but not necessarily normal to the deformed midsurface. This assumption leads to the constant transverse shear strains through the thickness and it may not be zero.

Because of the Mindlin hypothesis, the transverse shear strain is represented as constant through the thickness. It follows that the transverse shear stresses will also be constant in the thickness direction. But according to elementary theory, the transverse shear stress varies parabolically in the thickness direction. In the laminated composite structure, the transverse shear stress varies at least quadratically in the thickness direction. This discrepancy between the actual stress and transverse stress predicted from FOST is corrected by introducing the shear correction factor.

The shear correction factor is calculated by equating the strain energy due to the actual transverse shear stress in elementary theory to the strain energy due to the transverse shear stress in FOST. Even though shear correction factor depends on the properties of lamina and lamination scheme, a value of 5/6 has often been taken for the analysis [165].

3.4 Shell finite element for piezo-thermo-elastic analysis

The Koiter's [57] equations of equilibrium with body forces (which, by D' Alembert principle can immediately be converted into equations of motion) are remarkable in several ways. Mainly, they are much simpler than the analogous equations of Love for a comparison but of equal accuracy. The stress-resultant type Koiter's shell theory has been considered to formulate the present finite element formulation of the smart FRP composite shells. Since the Koiter's shell theory is based on the Love-Kirchhoff assumptions, the effect of shear deformation was not considered by the Koiter's shell theory. This effect has been considered in the formulation of shell according to the Mindlin's hypothesis. It has been established that the assumption of the first order shear deformation in the thickness direction is sufficient for the prediction of global response of thin to moderately thick shells.

Moreover, the treatments involved with the incorporation of shear deformation are quite simple in the first order shear deformation theory (FOST). Therefore, the effect of transverse shear strain has been incorporated in the Koiter's shell theory according to the first order shear deformation theory (FOST).

3.4. 1 Assumptions made in present formulation

3.4.1.1 Assumptions in mechanical analysis

- The laminated composite shell structures consist of a number of perfectly bonded layers, which are treated as homogeneous and orthotropic and the fibers in each layer are oriented arbitrarily with respect to the reference axis system.
- The material used for the shell structure is linear and elastic and Hooke's law is valid.
- The deformations follow Mindlin's hypothesis. Therefore any normal to the middle surface of the shell before deformation remains straight but not necessarily normal to the deformed middle surface.
- The in-plane displacement components are assumed to vary linearly along the thickness direction to yield constant transverse shear strain.

3.4.1.2 Assumptions in electro-mechanical analysis

In addition to the assumptions made for mechanical analysis, the following assumptions have been made on the variation of electric potential and electric field.

- The variation of electric potential is linear in the thickness direction and the electric potential is constant over each piezo layer/ each element of a particular layer.
- Linear constitutive relations of the piezoelectric material have been considered.
- The piezoelectric principal axis is parallel to the structural orthotropic axis and so the poling direction is z.
- No shear strain is induced by the transverse electric field.

3.4.1.3 Assumptions in piezothermoelastic analysis

In addition to the assumptions made for electromechanical analysis, the following assumptions have also been made on the variation of temperature field.

- The variation of thermal load is linear in the thickness direction and the temperature is constant on top and bottom surface of laminate/each element of the laminate.

3.4.2 Geometry of shell midsurface

The shell geometry used in the present formulation has been developed using an orthogonal curvilinear coordinate system with the midplane of the shell assumed to be the reference surface as shown in Fig. 3.1. The shell midsurface in the Cartesian rectangular coordinate system has been first mapped into a parametric domain through the suitable exact parametrization. Two independent coordinates (α_1, α_2) in the parametric space have been considered as the midsurface curvilinear coordinates of the shell. The normal direction coordinate to the middle surface of the shell has been represented by z. The reference surface or the shell midsurface can be described in the global cartesian coordinates in terms of the position vector as

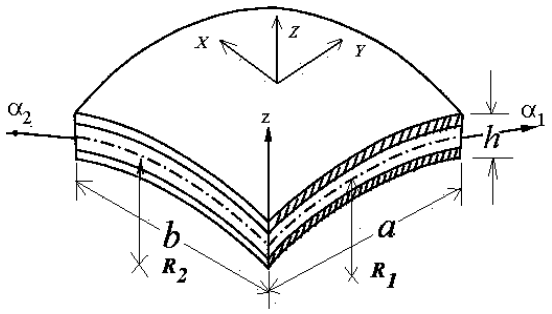

Fig 3.1 Geometry of layered composite shell panel in cartesian coordinate system

$$r(\alpha_1, \alpha_2) = X(\alpha_1, \alpha_2)\,\hat{i} + Y(\alpha_1, \alpha_2)\,\hat{j} + Z(\alpha_1, \alpha_2)\,\hat{k} \tag{3.1}$$

where, $\hat{i}$, $\hat{j}$ and $\hat{k}$ are unit vectors along the X, Y and Z axis, respectively. The tangent to the isoparametric curves $s_{\alpha 1}$ and $s_{\alpha 2}$ respectively are

$$r_{,1} = \frac{\partial r}{\partial \alpha_1}, \text{ and } r_{,2} = \frac{\partial r}{\partial \alpha_2} \tag{3.2}$$

The vector joining two points on the middle surface (α_1, α_2) and $(\alpha_1 + d\alpha_1, \alpha_2 + d\alpha_2)$ is given as

$$ds = r_{,1}\, d\alpha_1 + r_{,2}\, d\alpha_2 \tag{3.3}$$

The scalar product of ds

$$ds.ds = (r_{,1}.r_{,1})d\alpha_1^2 + (r_{,2}.r_{,2})d\alpha_2^2 \tag{3.4}$$

Defining

$$A_1 = \sqrt{r_{,1}.r_{,1}} \text{ and } A_2 = \sqrt{r_{,2}.r_{,2}} \tag{3.5}$$

as the Lame's parameters or measure numbers that are fundamentals for the understanding of curvilinear coordinates,

$$ds^2 = A_1^2 d\alpha_1^2 + A_2^2 d\alpha_2^2 \tag{3.6}$$

Since the α_1 and α_2 are independent coordinates

$$ds^2 = ds_{\alpha 1}^2 + ds_{\alpha 2}^2 \tag{3.7}$$

$$\begin{aligned} ds_{\alpha 1} &= A_1 d\alpha_1 \\ ds_{\alpha 2} &= A_2 d\alpha_2 \end{aligned} \tag{3.8}$$

The unit tangent vectors to the isoparametric curve $s_{\alpha 1}$ and $s_{\alpha 2}$ can be expressed respectively as

$$\hat{e}_1 = \frac{r_{,1}}{A_1} \tag{3.9}$$

and $$\hat{e}_2 = \frac{r_{,2}}{A_2} \tag{3.10}$$

The subscripts 1 and 2 in $r_{,1}$ and $r_{,2}$ indicate the derivative with respect to α_1 and α_2 respectively.

The unit normal vector to the tangent plane of any point on the reference surface can be expressed as

$$\hat{e}_n = \frac{r_{,1} \times r_{,2}}{\left| r_{,1} \times r_{,2} \right|} \tag{3.11}$$

The normal curvatures of the shell midsurface can be expressed as

$$\frac{1}{R_1} = -\frac{\hat{e}_n . r_{,11}}{A_1^2} \text{ and } \frac{1}{R_2} = -\frac{\hat{e}_n . r_{,22}}{A_2^2} \tag{3.12}$$

and the twist curvatures of the shell midsurface can be expressed as

$$\frac{1}{R_{12}} = -\frac{\hat{e}_n . r_{,12}}{A_1 A_2} \tag{3.13}$$

3.4.3 Isoparametric mapping

The shell midsurface in the rectangular cartesian coordinate system has been mapped into the parametric space (α_1, α_2) and the midsurface in the parametric space has been divided into required number of quadrilateral elements or sub-domains. The reference coordinates (ξ, η) map the quadrilateral element in the curvilinear coordinates (α_1, α_2) into the reference coordinates that is a square as shown in Fig. 3.2. Any point within an element in the parametric space has been approximated by the isoparametric mapping.

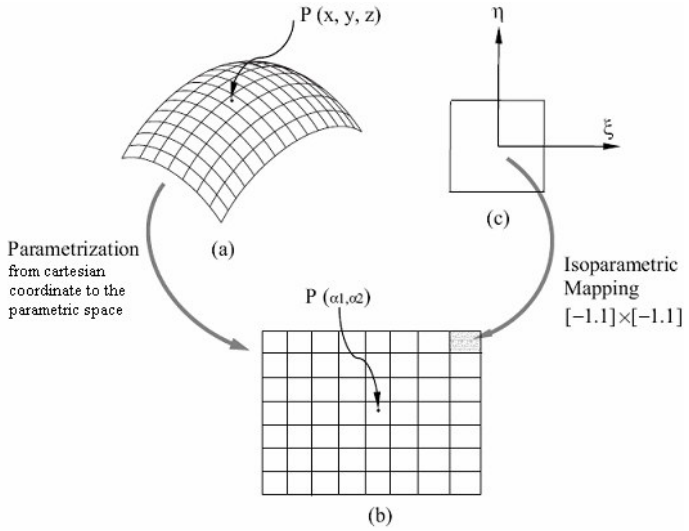

Fig 3.2 Mapping of midsurface of shell (a) Global space; (b) Parametric space; (c) Isoparametric space

Hence the curvilinear coordinates (α_1, α_2) of any point within an element may be expressed as

$$\alpha_1 = \sum_{i=1}^{nd} N_i \alpha_{1i}$$
$$\alpha_2 = \sum_{i=1}^{nd} N_i \alpha_{2i} \tag{3.14}$$

The displacement components on the shell midsurface at any point within an element may be expressed as

$$\begin{Bmatrix} u_0 \\ v_0 \\ w \\ \theta_1 \\ \theta_2 \end{Bmatrix} = \sum_{i=1}^{nd} N_i \begin{Bmatrix} u_{0i} \\ v_{0i} \\ w_i \\ \theta_{1i} \\ \theta_{2i} \end{Bmatrix} \tag{3.15}$$

where, nd is the number of nodes in an element,

N_i is the shape function corresponding to the i^{th} node and shape functions of 8 noded serendipity element are given below

$$N_1 = \frac{1}{4}(1-\xi)(1-\eta)(-1-\xi-\eta)$$
$$N_2 = \frac{1}{2}(1-\xi^2)(1-\eta)$$

$$
\begin{aligned}
N_3 &= \frac{1}{4}(1+\xi)(1-\eta)(-1+\xi-\eta) \\
N_4 &= \frac{1}{2}(1+\xi)(1-\eta^2) \\
N_5 &= \frac{1}{4}(1+\xi)(1+\eta)(-1+\xi+\eta) \\
N_6 &= \frac{1}{2}(1-\xi^2)(1+\eta) \\
N_7 &= \frac{1}{4}(1-\xi)(1+\eta)(-1-\xi+\eta) \\
N_8 &= \frac{1}{2}(1-\xi)(1-\eta^2)
\end{aligned}
\tag{3.16}
$$

(α_1, α_2) is the coordinate of midsurface at i^{th} node in curvilinear coordinate system. u_{0i}, v_{0i} and w_{0i} are the deflection of midsurface at i^{th} node in α_1, α_2 and z directions respectively. θ_{1i} is the rotation of normal at i^{th} node about α_2 axis and θ_{2i} is the rotation of normal at i^{th} node about α_1 axis.

3.4.4 Strain displacement relations

Neglecting normal strain component in the thickness direction, the five strain components of a doubly curved shell may be express as

$$\begin{bmatrix} \varepsilon_{xx} & \varepsilon_{yy} & \gamma_{xy} & \gamma_{yz} & \gamma_{xz} \end{bmatrix}^T = \begin{bmatrix} \varepsilon^0_{xx} & \varepsilon^0_{yy} & \gamma^0_{xy} & \gamma^0_{yz} & \gamma^0_{xz} \end{bmatrix}^T + z\begin{bmatrix} k_{xx} & k_{yy} & k_{xy} & 0 & 0 \end{bmatrix}^T \tag{3.17}$$

where $\varepsilon^0_{xx}, \varepsilon^0_{yy}$ and γ^0_{xy} are the in-plane strains of the midsurface in the cartesian coordinate system and k_{xx}, k_{yy} and k_{xy} are the bending strains (curvatures) of the midsurface in the cartesian coordinates system. After incorporating the effect of transverse stain in Koiter's shell theory**,** inplane and transverse strain-displacement relations may be expressed as described in the following subsections.

3.4.4.1 In-plane/bending strain-displacement matrix

Using isoparametric 8-noded shell element, the displacement component on the shell midsurface at any point within an element can be expressed as

$$\begin{Bmatrix} u_0 \\ v_0 \\ w \\ \theta_1 \\ \theta_2 \end{Bmatrix} = [N]\{d^e\} \tag{3.18}$$

According to Koiter's shell theory, the midsurface strains and curvatures may be expressed in terms of field variables as

$$\varepsilon_{xx}^0 = \frac{1}{A_1}\frac{\partial u}{\partial \alpha_1} + \frac{v}{A_1 A_2}\frac{\partial A_1}{\partial \alpha_2} + \frac{w}{R_1}$$

$$\varepsilon_{yy}^0 = \frac{1}{A_2}\frac{\partial v}{\partial \alpha_2} + \frac{u}{A_1 A_2}\frac{\partial A_2}{\partial \alpha_1} + \frac{w}{R_2}$$

$$\gamma_{xy}^0 = \frac{1}{A_1}\frac{\partial v}{\partial \alpha_1} + \frac{1}{A_2}\frac{\partial u}{\partial \alpha_2} - \frac{u}{A_1 A_2}\frac{\partial A_1}{\partial \alpha_2} - \frac{v}{A_1 A_2}\frac{\partial A_2}{\partial \alpha_1} + \frac{2w}{R_{12}}$$

$$k_{xx} = \frac{1}{A_1}\frac{\partial \theta_1}{\partial \alpha_1} + \frac{\theta_2}{A_1 A_2}\frac{\partial A_1}{\partial \alpha_2} + \frac{1}{2R_{12}}\left(\frac{1}{A_1}\frac{\partial v}{\partial \alpha_1} - \frac{1}{A_2}\frac{\partial u}{\partial \alpha_2} - \frac{u}{A_1 A_2}\frac{\partial A_1}{\partial \alpha_2} + \frac{v}{A_1 A_2}\frac{\partial A_2}{\partial \alpha_1}\right)$$

$$k_{yy} = \frac{1}{A_2}\frac{\partial \theta_2}{\partial \alpha_2} + \frac{\theta_1}{A_1 A_2}\frac{\partial A_2}{\partial \alpha_1} - \frac{1}{2R_{12}}\left(\frac{1}{A_1}\frac{\partial v}{\partial \alpha_1} - \frac{1}{A_2}\frac{\partial u}{\partial \alpha_2} - \frac{u}{A_1 A_2}\frac{\partial A_1}{\partial \alpha_2} + \frac{v}{A_1 A_2}\frac{\partial A_2}{\partial \alpha_1}\right)$$

$$k_{xy} = \begin{bmatrix} \frac{1}{A_1}\frac{\partial \theta_2}{\partial \alpha_1} + \frac{1}{A_2}\frac{\partial \theta_1}{\partial \alpha_2} - \frac{\theta_1}{A_1 A_2}\frac{\partial A_1}{\partial \alpha_2} - \frac{\theta_2}{A_1 A_2}\frac{\partial A_2}{\partial \alpha_1} - \\ \frac{1}{2}\left(\frac{1}{R_1} - \frac{1}{R_2}\right)\left(\frac{1}{A_1}\frac{\partial v}{\partial \alpha_1} - \frac{1}{A_2}\frac{\partial u}{\partial \alpha_2} - \frac{u}{A_1 A_2}\frac{\partial A_1}{\partial \alpha_2} + \frac{v}{A_1 A_2}\frac{\partial A_2}{\partial \alpha_1}\right) \end{bmatrix} \tag{3.19}$$

By using 8-noded isoparametric shape functions from Eq. (3.16), the strain components at any point on the shell midsurface can be expressed as

$$\{\varepsilon\} = \sum_{i=1}^{8} \begin{bmatrix} \frac{1}{A_1}\frac{\partial N_i}{\partial \alpha_1} & \frac{N_i}{A_1 A_2}\frac{\partial A_1}{\partial \alpha_2} & \frac{N_i}{R_1} & 0 & 0 \\ \frac{N_i}{A_1 A_2}\frac{\partial A_2}{\partial \alpha_1} & \frac{1}{A_2}\frac{\partial N_i}{\partial \alpha_2} & \frac{N_i}{R_2} & 0 & 0 \\ \frac{1}{A_2}\frac{\partial N_i}{\partial \alpha_2} - \frac{N_i}{A_1 A_2}\frac{\partial A_1}{\partial \alpha_2} & \frac{1}{A_1}\frac{\partial N_i}{\partial \alpha_1} - \frac{N_i}{A_1 A_2}\frac{\partial A_2}{\partial \alpha_1} & \frac{2N_i}{R_{12}} & 0 & 0 \\ -\frac{1}{2}\frac{1}{R_{12}}\left(\frac{1}{A_2}\frac{\partial N_i}{\partial \alpha_2} + \frac{N_i}{A_1 A_2}\frac{\partial A_1}{\partial \alpha_2}\right) & \frac{1}{2}\frac{1}{R_{12}}\left(\frac{1}{A_1}\frac{\partial N_i}{\partial \alpha_1} + \frac{N_i}{A_1 A_2}\frac{\partial A_2}{\partial \alpha_1}\right) & 0 & \frac{1}{A_1}\frac{\partial N_i}{\partial \alpha_1} & \frac{N_i}{A_1 A_2}\frac{\partial A_1}{\partial \alpha_2} \\ \frac{1}{2}\frac{1}{R_{12}}\left(\frac{1}{A_2}\frac{\partial N_i}{\partial \alpha_2} + \frac{N_i}{A_1 A_2}\frac{\partial A_1}{\partial \alpha_2}\right) & -\frac{1}{2}\frac{1}{R_{12}}\left(\frac{1}{A_1}\frac{\partial N_i}{\partial \alpha_1} + \frac{N_i}{A_1 A_2}\frac{\partial A_2}{\partial \alpha_1}\right) & 0 & \frac{N_i}{A_1 A_2}\frac{\partial A_2}{\partial \alpha_1} & \frac{1}{A_2}\frac{\partial N_i}{\partial \alpha_2} \\ C_0\left(\frac{1}{A_2}\frac{\partial N_i}{\partial \alpha_2} + \frac{N_i}{A_1 A_2}\frac{\partial A_1}{\partial \alpha_2}\right) & -C_0\left(\frac{1}{A_1}\frac{\partial N_i}{\partial \alpha_1} + \frac{N_i}{A_1 A_2}\frac{\partial A_2}{\partial \alpha_1}\right) & 0 & \frac{1}{A_2}\frac{\partial N_i}{\partial \alpha_2} - \frac{N_i}{A_1 A_2}\frac{\partial A_1}{\partial \alpha_2} & \frac{1}{A_1}\frac{\partial N_i}{\partial \alpha_1} - \frac{N_i}{A_1 A_2}\frac{\partial A_2}{\partial \alpha_1} \end{bmatrix} \begin{Bmatrix} u_{0i} \\ v_{0i} \\ w_i \\ \theta_{1i} \\ \theta_{2i} \end{Bmatrix}$$

$$= \left[B_b^e\right]\left\{d^e\right\} \tag{3.20}$$

where $C_0 = \frac{1}{2}\left(\frac{1}{R_1} - \frac{1}{R_2}\right)$

3.4.4.2 Transverse strain displacement matrix

According to the FOST, the transverse shear strain vector of a doubly curved shell element may be expressed as

$$\begin{Bmatrix}\gamma_{yz}\\ \gamma_{xz}\end{Bmatrix}=\begin{Bmatrix}\theta_2+\frac{1}{A_2}\frac{\partial w}{\partial\alpha_2}-\frac{u}{R_{12}}-\frac{v}{R_2}\\ \theta_1+\frac{1}{A_1}\frac{\partial w}{\partial\alpha_1}-\frac{u}{R_1}-\frac{v}{R_{12}}\end{Bmatrix} \tag{3.21}$$

and hence the transverse shear strain at any point on the shell mid surface can be expressed as

$$\begin{Bmatrix}\gamma_{yz}\\ \gamma_{xz}\end{Bmatrix}=\sum_{k=1}^{nd}\begin{bmatrix}-\frac{N_i}{R_{12}} & -\frac{N_i}{R_2} & \frac{1}{A_2}\frac{\partial N_i}{\partial\alpha_2} & 0 & N_i\\ -\frac{N_i}{R_1} & -\frac{N_i}{R_{12}} & \frac{1}{A_1}\frac{\partial N_i}{\partial\alpha_1} & N_i & 0\end{bmatrix}\begin{Bmatrix}u_{0i}\\ v_{0i}\\ w_i\\ \theta_{1i}\\ \theta_{2i}\end{Bmatrix}$$

$$=\left[B_s^e\right]\left\{d^e\right\} \tag{3.22}$$

3.4.5 Piezothermoelastic constitutive relation

It has been assumed that the piezoelectric continuum is exposed to three fields viz. an elastic field, an electric field, and a thermal field. The linear constitutive equations of piezothermoelasticity expressing the coupling between the elastic, electric and thermal fields can be defined as

$$\{\sigma\}=[C]\{\varepsilon\}-[e]^T\{E\}-\{\lambda\}\Delta T \tag{3.23}$$

$$\{D\}=[e]\{\varepsilon\}+[\in]\{E\}+\{p\}\Delta T \tag{3.24}$$

$$\eta=\{\lambda\}^T\{\varepsilon\}+\{p\}^T\{E\}+a_T\Delta T \tag{3.25}$$

where,

Stress tensor $\{\sigma\}=\left[\sigma_{xx}\quad\sigma_{yy}\quad\tau_{yz}\quad\tau_{xz}\quad\tau_{xy}\right]^T$,

Strain tensor $\{\varepsilon\}=\left[\varepsilon_{xx}\quad\varepsilon_{yy}\quad\gamma_{yz}\quad\gamma_{xz}\quad\gamma_{xy}\right]^T$,

Elasticity matrix $[C]=\begin{bmatrix}C_{11} & C_{12} & 0 & 0 & 0\\ C_{12} & C_{22} & 0 & 0 & 0\\ 0 & 0 & C_{44} & 0 & 0\\ 0 & 0 & 0 & C_{55} & 0\\ 0 & 0 & 0 & 0 & C_{66}\end{bmatrix}$,

Electric displacement $\{D\} = [D_1 \quad D_2 \quad D_3]^T$,

Electric field vector $\{E\} = [E_1 \quad E_2 \quad E_3]^T$,

Piezo electric coefficient $[e] = \begin{bmatrix} e_{11} & e_{12} & e_{14} & e_{15} & e_{16} \\ e_{21} & e_{22} & e_{24} & e_{25} & e_{26} \\ e_{31} & e_{32} & e_{34} & e_{35} & e_{36} \end{bmatrix}$,

Thermal stress coefficient $\{\lambda\} = [\lambda_1 \quad \lambda_2 \quad \lambda_4 \quad \lambda_5 \quad \lambda_6]^T$,

Dielectric permittivity $[\in] = \begin{bmatrix} \in_{11} & 0 & 0 \\ 0 & \in_{22} & 0 \\ 0 & 0 & \in_{33} \end{bmatrix}$,

Pyroelectric coefficient $\{p\} = [p_1 \quad p_2 \quad p_3]^T$,

η is the entropy per unit volume,

ΔT is the temperature rise from the stress free reference temperature t_0,

$a_T = \dfrac{\rho c_v}{t_0}$, c_v is the specific heat at constant volume and ρ is mass density.

3.4.6 Direct and converse piezoelectric relations

The thermal field terms are neglected in the coupled Eqs (3.23) and (3.24) to obtain the direct and converse piezoelectric relations. The electro-mechanical coupled equations coupling the elastic and electric fields can be respectively expressed as the direct and converse piezoelectric equations as

$$\{\sigma\} = [C]\{\varepsilon\} - [e]^T \{E\} \tag{3.26}$$

$$\{D\} = [e]\{\varepsilon\} + [\in]\{E\} \tag{3.27}$$

The strain $\{\varepsilon\}$ in the piezoelectric material induces a polarization $[e]\{\varepsilon\}$ by the direct piezoelectric effect. Hence the coupled equation with direct piezoelectric effect becomes

$$\{D\} = [e]\{\varepsilon\} + [\in]\{E\} \tag{3.28}$$

Eq. (3.28) is the starting point for the formulation of the equation of a piezoelectric sensor. Conversely, an applied electric field $\{E\}$ induces the stresses $-[e]^T \{E\}$ in the material by the inverse piezoelectric effect. Hence the coupled equation with inverse piezoelectric effect becomes

$$\{\sigma\} = [C]\{\varepsilon\} - [e]^T \{E\} \tag{3.29}$$

Equation (3.29) is the starting point for the formulation of equation of a piezoelectric actuator.

3.4.7 Electrical potential in the piezoelectric layers/ patches

For thin piezoelectric layers, the component of electric field in the thickness direction (E_z) is dominant. Hence the electric field can be accurately approximated with a non-zero component only in the thickness direction. Therefore it is assumed that the electric potential varies only in the thickness direction and constant in *x* and *y* direction. Since the electrical potential is assumed constant in x and y direction, the negative gradient of electrical potential with respect to x and y for a layer is zero. Two kinds of electrical approximations are implemented in this work.

1. Electrical potential varies linearly in the thickness direction and only one electrical degree of freedom is taken for each piezo layer. Therefore, the electrical potential is constant over each layer. With this assumption, the electrical potential vector for an entire structure can be expressed as

$$\{\phi\} = \begin{Bmatrix} \phi_1 \\ \phi_2 \\ \vdots \\ \phi_{nl} \end{Bmatrix} \tag{3.30}$$

where ϕ_1, is the electrical potential for the first piezo layer, ϕ_2, is the electrical potential for the second piezo layer and so on and *nl* is the total number of layers.

Since it has been assumed that the electrical potential is constant over each layer, the electrical potential vector is same for all the elements of particular lamina. Since electrical potential is assumed to be constant in x and y direction, the electric field components in these directions are zero. Hence for k^{th} layer, the electric field vector may be written as

$$\{-E_k\} = \begin{Bmatrix} -E_{xk} \\ -E_{yk} \\ -E_{zk} \end{Bmatrix} = \begin{Bmatrix} 0 \\ 0 \\ \dfrac{1}{h_k} \end{Bmatrix} \phi_k \tag{3.31}$$

where ϕ_k, is the electrical potential difference of k^{th} layer, and h_k, is the thickness of k^{th} layer

2. Electrical potential varies linearly in the thickness direction and the elemental electrical degree of freedom is considered. From this assumption, the electrical potential vector for an i^{th} element can be expressed as

$$\{\phi^i\} = \begin{Bmatrix} \phi_1^i \\ \phi_2^i \\ \vdots \\ \phi_{nl}^i \end{Bmatrix} \tag{3.32}$$

where ϕ_1^i, is the electrical potential difference for the first layer of i^{th} element, ϕ_2^i, is the electrical potential difference for the second layer of i^{th} element and so on. Hence the electric field for k^{th} layer of i^{th} element may be written as

$$\{-E_k^i\} = \begin{Bmatrix} -E_{xk}^i \\ -E_{yk}^i \\ -E_{zk}^i \end{Bmatrix} = \begin{Bmatrix} 0 \\ 0 \\ \dfrac{1}{h_k^i} \end{Bmatrix} \phi_k^i \tag{3.33}$$

where ϕ_k^i, is the electrical potential difference of k^{th} layer of i^{th} element and h_k^i, is the thickness of k^{th} layer of i^{th} element. Since the electric field is non zero only in the thickness direction, the electric field term in the other directions are removed. Therefore, the electric field vector for an element can be written as

$$\{-E_z^i\} = \left[B_\phi^i\right]\{\phi^i\} \tag{3.34}$$

where ,$\{-E_z^i\}$ is the electric field vector of i^{th} element in the thickness direction and $\left[B_\phi^i\right]$, is the functional derivative relating electrical field and electrical potential of i^{th} element.

3.4.8 Temperature field

Two kinds of temperature distribution approximations have been implemented in this work. In both the cases, it has been assumed that the temperature varies linearly in the thickness direction from top surface to bottom surface of laminate.

1. Linear temperature variation is considered in the thickness direction of laminate and only two thermal degrees of freedom are considered for whole laminate. One is temperature at the top surface of laminate and another one is the temperature at the bottom surface of laminate. Therefore, the temperatures on the top surface of all the

elements are same and temperatures on the bottom surface of all the elements are same. Temperature field for the laminate is

$$t(z)=\frac{t_t+t_b}{2}+z\frac{t_t-t_b}{h} \tag{3.35}$$

$$=\left\lfloor \frac{1}{2}-\frac{z}{h} \quad \frac{1}{2}+\frac{z}{h} \right\rfloor \begin{Bmatrix} t_t \\ t_b \end{Bmatrix}$$

$$=\lfloor N_t \rfloor \{\theta_t\} \tag{3.36}$$

where, t_t and t_b are temperatures on top and bottom surface of laminate, respectively and h is the thickness of laminate.

2. Linear temperature variation is considered in the thickness direction of laminate and two thermal degrees of freedom are considered for every element. One is the temperature at the top surface of an element and another one is the temperature at the bottom surface of an element. Temperature field for the i^{th} element is

$$t^i(z)=\frac{t_t^i+t_b^i}{2}+z\frac{t_t^i-t_b^i}{h^i} \tag{3.37}$$

$$=\left\lfloor \frac{1}{2}-\frac{z}{h^i} \quad \frac{1}{2}+\frac{z}{h^i} \right\rfloor \begin{Bmatrix} t_t^i \\ t_b^i \end{Bmatrix}$$

$$=\lfloor N_t^i \rfloor \{\theta_t^i\} \tag{3.38}$$

where, t_t^i and t_b^i are temperatures on top and bottom surface of i^{th} element, respectively and h^i, is the thickness of i^{th} element.

3.4.9 Finite element equations

In this section, the piezothermoelastic finite element formulation has been derived for static and dynamic analysis.

3.4.9.1 Static finite element equations

The total potential energy of the element is given by

$$\prod = U - W \tag{3.39}$$

The internal potential energy U consists of the elastic strain energy of the entire structure (V^m), the electrical potential energy of piezoelectric layers (V^e) and the internal energy due to the thermal fields (V^t) as

$$U = V^m + V^e + V^t \tag{3.40}$$

External work done W consists of external work done by both applied mechanical force and the applied electrical charges.

a) Elastic strain energy of the entire structure

$$
\begin{aligned}
V^m &= \frac{1}{2}\int_V \{\varepsilon\}^T \{\sigma\} dV \\
&= \frac{1}{2}\int_V \{\varepsilon\}^T \left([C]\{\varepsilon\} - [e]^T \{E\} - \{\lambda\}\Delta T\right) dV \\
&= \frac{1}{2}\int_V \{\varepsilon\}^T \left([C]\{\varepsilon\} + [e]^T \{-E\} - \{\lambda\}\Delta T\right) dV \\
&= \frac{1}{2}\int_V \{\varepsilon\}^T [C]\{\varepsilon\} dV + \frac{1}{2}\int_{V_p} \{\varepsilon\}^T [e]^T \{-E\} dV_p - \frac{1}{2}\int_V \{\varepsilon\}^T \{\lambda\}\Delta T dV \\
&= \frac{1}{2}\{d^e\}^T \int_V \left[B_u^e\right]^T [C]\left[B_u^e\right] dV \{d^e\} + \frac{1}{2}\{d^e\}^T \int_{V_p} \left[B_u^e\right]^T [e]^T \left[B_\phi^e\right] dV_p \{\phi^e\} \\
&\quad - \frac{1}{2}\{d^e\}^T \int_V \left[B_u^e\right]^T \{\lambda\} \left[N_t^e\right] dV \{\theta_t\} \\
&= \frac{1}{2}\{d^e\}^T \left[K_{uu}^e\right]\{d^e\} + \frac{1}{2}\{d^e\}^T \left[K_{u\phi}^e\right]\{\phi^e\} - \frac{1}{2}\{d^e\}^T \left[K_{ut}^e\right]\{\theta_t\}
\end{aligned}
\tag{3.41}
$$

b) Electrical potential energy of piezoelectric layers

$$
\begin{aligned}
V^e &= -\frac{1}{2}\int_{V_P} \{E^e\}^T \{D\} dV_p \\
&= -\frac{1}{2}\int_{V_P} \{E^e\}^T \left([e]\{\varepsilon\} + [\in]\{E^e\} + \{p\}\Delta T\right) dV_p \\
&= -\frac{1}{2}\int_{V_P} \{E^e\}^T [e]\{\varepsilon\} dV_p - \frac{1}{2}\int_{V_P} \{E^e\}^T [\in]\{E^e\} dV_p - \frac{1}{2}\int_V \{E^e\}^T \{p\}\Delta T dV \\
&= -\frac{1}{2}\int_{V_P} \{E^e\}^T [e]\{\varepsilon\} dV_p - \frac{1}{2}\int_{V_P} \{-E^e\}^T [\in]\{-E^e\} dV_p + \frac{1}{2}\int_V \{-E^e\}^T \{p\}\Delta T dV \\
&= \frac{1}{2}\{\phi^e\}^T \int_{V_P} \left[B_\phi^e\right]^T [e]\left[B_u^e\right] dV_p \{d^e\} - \frac{1}{2}\{\phi^e\}^T \int_{V_P} \left[B_\phi^e\right]^T [\in]\left[B_\phi^e\right] dV_p \{\phi^e\} \\
&\quad + \frac{1}{2}\{\phi^e\}^T \int_{V_P} \left[B_\phi^e\right]^T \{p\} \left[N_t^e\right] dV \{\theta_t\} \\
&= \frac{1}{2}\{\phi^e\}^T \int_{V_P} \left[B_\phi^e\right]^T [e]\left[B_u^e\right] dV_p \{d^e\} + \frac{1}{2}\{\phi^e\}^T \left(-\int_{V_P} \left[B_\phi^e\right]^T [\in]\left[B_\phi^e\right] dV_p\right)\{\phi^e\} \\
&\quad + \frac{1}{2}\{\phi^e\}^T \int_{V_P} \left[B_\phi^e\right]^T \{p\} \left[N_t^e\right] dV \{\theta_t\} \\
&= \frac{1}{2}\{\phi^e\}^T \left[K_{\phi u}^e\right]\{d^e\} + \frac{1}{2}\{\phi^e\}^T \left[K_{\phi\phi}^e\right]\{\phi^e\} + \frac{1}{2}\{\phi^e\}^T \left[K_{\phi t}^e\right]\{\theta_t\}
\end{aligned}
\tag{3.42}
$$

c) Internal energy due to the thermal field

$$V^t = -\frac{1}{2}\int_V \Delta T \eta dV$$

$$= -\frac{1}{2}\int_V \Delta T \left(\{\lambda\}^T \{\varepsilon\} + \{p\}^T \{E\} + a_T \Delta T\right) dV$$

$$= -\frac{1}{2}\int_V \Delta T \{\lambda\}^T \{\varepsilon\} dV + \frac{1}{2}\int_{V_p} \Delta T \{p\}^T \{-E\} dV_p - \frac{1}{2}\int_V \Delta T a_T \Delta T dV$$

$$= -\frac{1}{2}\int_V \{\theta_t\}^T \left\lfloor N_t^e \right\rfloor^T \{\lambda\}^T \left[B_u^e\right] dV \{d^e\} + \frac{1}{2}\int_{V_p} \{\theta_t\}^T \left\lfloor N_t^e \right\rfloor^T \{p\}^T \left[B_\phi^e\right] dV_p \{\phi^e\}$$

$$-\frac{1}{2}\int_V \{\theta_t\}^T \left\lfloor N_t^e \right\rfloor^T a_T \left\lfloor N_t^e \right\rfloor dV \{\theta_t\}$$

$$= -\frac{1}{2}\{d^e\}^T \int_V \left[B_u^e\right]^T \{\lambda\} \left[N_t^e\right] dV \{\theta_t\} + \frac{1}{2}\int_{V_p} \{\phi^e\}^T \left[B_\phi^e\right]^T \{p\} \left\lfloor N_t^e \right\rfloor dV_p \{\theta_t\}$$

$$-\frac{1}{2}\int_V \{\theta_t\}^T \left\lfloor N_t^e \right\rfloor^T a_T \left\lfloor N_t^e \right\rfloor dV \{\theta_t\}$$

$$= -\frac{1}{2}\{d^e\}^T \left[K_{ut}^e\right]\{\theta_t\} + \frac{1}{2}\{\phi^e\}^T \left[K_{\phi t}^e\right]\{\theta_t\} - \frac{1}{2}\int_V \{\theta_t\}^T \left\lfloor N_t^e \right\rfloor^T a_T \left\lfloor N_t^e \right\rfloor dV \{\theta_t\} \quad (3.43)$$

where $\{\theta_t\}$ is the vector of top and bottom surface temperatures and ΔT is temperature gradient.

d) The total internal energy of the structure

$$U = \frac{1}{2}\{d^e\}^T \left[K_{uu}^e\right]\{d^e\} + \frac{1}{2}\{d^e\}^T \left[K_{u\phi}^e\right]\{\phi^e\} + \frac{1}{2}\{\phi^e\}^T \left[K_{\phi u}^e\right]\{d^e\}$$
$$+\frac{1}{2}\{\phi^e\}^T \left[K_{\phi\phi}^e\right]\{\phi^e\} - \{d^e\}^T \left[K_{ut}^e\right]\{\theta_t\} + \{\phi^e\}^T \left[K_{\phi t}^e\right]\{\theta_t\} \quad (3.44)$$
$$-\frac{1}{2}\int_V \{\theta_t\}^T \left\lfloor N_t^e \right\rfloor^T a_T \left\lfloor N_t^e \right\rfloor dV \{\theta_t\}$$

$$= \frac{1}{2}\{d^e\}^T \left[K_{uu}^e\right]\{d^e\} + \{d^e\}^T \left[K_{u\phi}^e\right]\{\phi^e\} + \frac{1}{2}\{\phi^e\}^T \left[K_{\phi\phi}^e\right]\{\phi^e\}$$
$$-\{d^e\}^T \left[K_{ut}^e\right]\{\theta_t\} + \{\phi^e\}^T \left[K_{\phi t}^e\right]\{\theta_t\} - \frac{1}{2}\int_V \{\theta_t\}^T \left\lfloor N_t^e \right\rfloor^T a_T \left\lfloor N_t^e \right\rfloor dV \{\theta_t\} \quad (3.45)$$

e) Work done by the external forces and electrical charges

$$W = \int_{A_1} \{d^e\}^T \{f_s^e(x,y)\} dA - \int_{A_2} \{\phi\}^T \{q^e(x,y)\} dA$$

$$= \{d^e\}^T \int_{A_1} [N]^T \{f_s^e(x,y)\} dA - \{\phi^e\}^T \int_{A_2} \left[N_\phi^e\right]^T \{q^e(x,y)\} dA \quad (3.46)$$

$$= \{d^e\}^T \{F^e\} + \{\phi^e\}^T \{G^e\}$$

Substituting internal potential energy U and the external work done W in (3.39) and setting its first variation with respect to $\{d^e\}^T$ and $\{\phi^e\}^T$ to zero, the following system of equations for an element are obtained.

$$\left[K^e_{uu}\right]\{d^e\}+\left[K^e_{u\phi}\right]\{\phi^e\}-\left[K^e_{ut}\right]\{\theta_t\}=\{F^e\} \tag{3.47}$$

$$\left[K^e_{\phi u}\right]\{d^e\}+\left[K^e_{\phi\phi}\right]\{\phi^e\}+\left[K^e_{\phi t}\right]\{\theta_t\}=\{G^e\} \tag{3.48}$$

Eqs. (3.47) and (3.48) are the static piezothermoelastic equations for one element. The detailed derivation of all the matrices involved in the Eqs (3.47) and (3.48) for smart FRP composite structure is given in the Appendix.

where,

$$\left[K^e_{uu}\right]=\int_V\left[B^e_u\right]^T[C]\left[B^e_u\right]dV \tag{3.49}$$

$$\left[K^e_{uu}\right]=\left[K^e_{bb}\right]+\left[K^e_{ss}\right] \tag{3.50}$$

$$\left[B^e_u\right]=\begin{bmatrix}\left[B^e_b\right] & [0]\\ [0] & \left[B^e_s\right]\end{bmatrix} \tag{3.51}$$

$$[C]=\begin{bmatrix}[D_b] & [0]\\ [0] & [D_s]\end{bmatrix} \tag{3.52}$$

$$\left[K^e_{bb}\right]=\int_V\left[B^e_b\right]^T[D_b]\left[B^e_b\right]dV$$

$$=\int_\Omega\left[B^e_b\right]^T\begin{bmatrix}[A] & [B]\\ [B] & [D]\end{bmatrix}\left[B^e_b\right]d\Omega \tag{3.53}$$

$$\left[K^e_{ss}\right]=\int_V\left[B^e_s\right]^T[D_s]\left[B^e_s\right]dV \tag{3.54}$$

$$\left[K^e_{u\phi}\right]=\int_{V_p}\left[B^e_u\right]^T[e]^T\left[B^e_\phi\right]dV_p \tag{3.55}$$

$$\left[K^e_{ut}\right]=\int_V\left[B^e_u\right]^T\{\lambda\}\left\lfloor N^e_t\right\rfloor dV \tag{3.56}$$

$$\left[K^e_{\phi u}\right]=\left[K^e_{u\phi}\right]^T \tag{3.57}$$

$$\left[K^e_{\phi\phi}\right]=-\int_{V_p}\left[B^e_\phi\right]^T[\in]\left[B^e_\phi\right]dV_p \tag{3.58}$$

$$\left[K_{\phi t}^{e}\right]=\int_{V_p}\left[B_{\phi}^{e}\right]^{T}\{p\}\left\lfloor N_{t}^{e}\right\rfloor dV_p \tag{3.59}$$

$$\left\{F^{e}\right\}=\int_{A}\left[N\right]^{T}\left\{f_{s}^{e}\left(x,y\right)\right\}dA \tag{3.60}$$

$$\left\{G^{e}\right\}=-\int_{A}\left[N_{\phi}^{e}\right]^{T}\left\{q^{e}\left(x,y\right)\right\}dA \tag{3.61}$$

where

$\left[K_{uu}^{e}\right]$, is the element structural stiffness matrix

$\left[K_{u\phi}^{e}\right]$, is the element piezoelectric stiffness matrix

$\left[K_{ut}^{e}\right]$, is the element thermo elastic stiffness matrix

$\left[K_{\phi\phi}^{e}\right]$, is the element dielectric stiffness matrix

$\left[K_{\phi t}^{e}\right]$, is the element pyroelectric stiffness matrix

$\left\{F^{e}\right\}$, is the element external mechanical force vector

$\left\{G^{e}\right\}$, is the element external electrical force vector

$\left[K_{bb}^{e}\right]$, is the element in plane/bending stiffness matrix

$\left[K_{ss}^{e}\right]$, is the element transverse shear stiffness matrix

$\left[B_{b}^{e}\right]$, is the element in plane stain- displacement matrix

$\left[B_{s}^{e}\right]$, is the element transverse stain- displacement matrix

$\left[D_{b}\right]$, is the in-plane/bending constitutive matrix

$\left[D_{s}\right]$, is the transverse shear constitutive matrix

$\left[B_{\phi}^{e}\right]$, is the element electric field- potential matrix

$\left[e\right]$, is the piezoelectric coefficient matrix

$\left[\in\right]$, is the dielectric permittivity matrix

After assembling the elemental stiffness matrices, the global set of piezothermoelastic equations are given as

$$\begin{pmatrix}\left[K_{uu}\right] & \left[K_{u\phi}\right] & -\left[K_{ut}\right]\\ \left[K_{\phi u}\right] & \left[K_{\phi\phi}\right] & \left[K_{\phi t}\right]\end{pmatrix}\begin{Bmatrix}\{d\}\\ \{\phi\}\\ \{\theta_t\}\end{Bmatrix}=\begin{Bmatrix}\{F\}\\ \{G\}\end{Bmatrix} \tag{3.62}$$

The coupled piezoelectric equations can be written by taking the thermal strain effect and the pyroelectric effect as force vectors on the right hand side as follows

$$\begin{bmatrix} [K_{uu}] & [K_{u\phi}] \\ [K_{\phi u}] & [K_{\phi\phi}] \end{bmatrix} \begin{Bmatrix} \{d\} \\ \{\phi\} \end{Bmatrix} = \begin{Bmatrix} \{F\} + [K_{ut}]\{\theta_t\} \\ \{G\} - [K_{\phi t}]\{\theta_t\} \end{Bmatrix} \tag{3.63}$$

In Eq. (3.63), $[K_{ut}]\{\theta_t\}$, is the force vector due to the thermal strain effect, and $[K_{\phi t}]\{\theta_t\}$, is the force vector due to the pyroelectric effect.

3.4.9.2 Dynamic finite element equations

The dynamic finite element formulation has been derived by using Hamilton's principle as

$$\int_{t_1}^{t_2} (\delta L + \delta W_e) dt = 0 \tag{3.64}$$

where, the Lagrangian, $L = T - U$

and $U = V^m + V^e + V^t$

W_e is the external work done and the internal potential energy U consists of the elastic strain energy of the entire structure, the electrical potential energy of piezoelectric layers and the internal energy due to the thermal fields. Eq. (3.64) can be written as

$$\int_{t_1}^{t_2} (\delta [T - U] + \delta W_e) dt = 0$$

$$\Rightarrow \quad \int_{t_1}^{t_2} (\delta T - \delta U + \delta W_e) dt = 0$$

$$\Rightarrow \quad \int_{t_1}^{t_2} \left(\delta T - \delta \left(V^m + V^e + V^t \right) + \delta W_e \right) dt = 0 \tag{3.65}$$

where, t_1 and t_2 defines the time interval (all variations must vanish at $t = t_1$ and $t = t_2$), $T = \int_V \rho \left(\frac{1}{2} \{\dot{d}\}^T \{\dot{d}\} \right) dV$ is the kinetic energy and ρ is the mass density. Individual parts of the Hamilton equation can be written as follows:

Part 1: The kinetic energy of the system is

$$\int_{t_1}^{t_2} \delta T dt = \delta \int_{t_1}^{t_2} \int_V \rho \left(\frac{1}{2} \{\dot{d}\}^T \{\dot{d}\} \right) dV dt$$

$$
\begin{aligned}
&= -\int_{t_1}^{t_2}\int_{V} \rho\{\delta d\}^T \{\ddot{d}\} dV dt \\
&= -\int_{t_1}^{t_2} \{\delta d^e\}^T \left[\int_{V} \rho\left[N^T\right][N] dV\right] \{\ddot{d}^e\} dt \\
&= -\int_{t_1}^{t_2} \{\delta d^e\}^T \left[M^e_{uu}\right] \{\ddot{d}^e\} dt
\end{aligned} \tag{3.66}
$$

Part 2: The total internal energy of the system is

$$
\int_{t1}^{t2} \delta U dt = \int_{t1}^{t2} \delta\left(V^m + V^e + V^t\right) dt
$$

$$
\Rightarrow \int_{t1}^{t2} \delta U dt = \int_{t1}^{t2} \left(\begin{array}{l} \{\delta d^e\}^T \left[K^e_{uu}\right] \{d^e\} + \{\delta d^e\}^T \left[K^e_{u\phi}\right] \{\phi^e\} + \{\delta \phi^e\}^T \left[K^e_{\phi u}\right] \{d^e\} \\ + \{\delta \phi^e\}^T \left[K^e_{\phi\phi}\right] \{\phi^e\} - \{\delta d^e\}^T \left[K^e_{ut}\right] \{\theta_t\} + \{\delta \phi^e\}^T \left[K^e_{\phi t}\right] \{\theta_t\} \\ - \{\delta t\}^T \left[K^e_{ut}\right]^T \{d^e\} + \{\delta t\}^T \left[K^e_{\phi t}\right]^T \{\phi^e\} - \int_V \{\delta t\}^T \left\lfloor N^e_t \right\rfloor^T a_T \left\lfloor N^e_t \right\rfloor dV \{\theta_t\} \end{array} \right) dt \tag{3.67}
$$

Part 3: The work done by the external forces is

$$
\begin{aligned}
&\int_{t_1}^{t_2} \delta W_e dt = \int_{t_1}^{t_2} \left[\int_{A_1} \{\delta d^e\}^T \{f_s^e(x,y)\} dA - \int_{A_2} \{\delta \phi\}^T \{q^e(x,y)\} dA \right] dt \\
&= \int_{t_1}^{t_2} \left[\{\delta d^e\}^T \int_{A_1} [N]^T \{f_s^e(x,y)\} dA - \{\delta \phi^e\}^T \int_{A_2} \left[N^e_\phi\right]^T \{q^e(x,y)\} dA \right] dt \\
&= \{\delta d^e\}^T \{F^e\} + \{\delta \phi^e\}^T \{G^e\}
\end{aligned} \tag{3.68}
$$

Substituting Eqs. (3.66)- (3.68) in Eq. (3.65) gives

$$
\begin{aligned}
&\int_{t_1}^{t_2} \left[\{\delta d^e\}^T \left(-\left[M^e_{uu}\right] \{\ddot{d}^e\} - \left[K^e_{uu}\right] \{d^e\} - \left[K^e_{u\phi}\right] \{\phi^e\} + \left[K^e_{ut}\right] \{\theta_t\} + \{F^e\} \right) \right] dt \\
&+ \int_{t_1}^{t_2} \left[\{\delta \phi^e\}^T \left(-\left[K^e_{\phi u}\right] \{d^e\} - \left[K^e_{\phi\phi}\right] \{\phi^e\} - \left[K^e_{\phi t}\right] \{\theta_t\} + \{G^e\} \right) \right] dt \\
&+ \int_{t_1}^{t_2} \left[\{\delta t\}^T \left(\left[K^e_{ut}\right]^T \{d^e\} - \left[K^e_{\phi t}\right]^T \{\phi^e\} + \int_V \left\lfloor N^e_t \right\rfloor^T a_T \left\lfloor N^e_t \right\rfloor dV \{\theta_t\} \right) \right] dt = 0
\end{aligned} \tag{3.69}
$$

Since $\{\delta d^e\}, \{\delta \phi^e\}$ and $\{\delta t\}$ can be any arbitrary values, $\{\delta d^e\}, \{\delta \phi^e\}$ and $\{\delta t\} \neq 0$ and therefore the Eq. (3.65) is zero only if

$$
\left[M^e_{uu}\right] \{\ddot{d}^e\} + \left[K^e_{uu}\right] \{d^e\} + \left[K^e_{u\phi}\right] \{\phi^e\} - \left[K^e_{ut}\right] \{\theta_t\} = \{F^e\} \tag{3.70}
$$

$$
\left[K^e_{\phi u}\right] \{d^e\} + \left[K^e_{\phi\phi}\right] \{\phi^e\} + \left[K^e_{\phi t}\right] \{\theta_t\} = \{G^e\} \tag{3.71}
$$

Eqs. (3.70) and (3.71) are dynamic finite element equations of one element. The detailed derivation of mass matrix involving in the equations Eq. (3.70) is given in the Appendix.

Eqs. (3.70) and (3.71) can be written in matrix form as

$$\begin{pmatrix} \left[M_{uu}^{e}\right] & [0] & [0] \\ [0] & [0] & [0] \end{pmatrix} \begin{Bmatrix} \{\ddot{d}^{e}\} \\ \{\ddot{\phi}^{e}\} \\ \{\ddot{\theta}_{t}\} \end{Bmatrix} + \begin{pmatrix} \left[K_{uu}^{e}\right] & \left[K_{u\phi}^{e}\right] & -\left[K_{ut}^{e}\right] \\ \left[K_{\phi u}^{e}\right] & \left[K_{\phi\phi}^{e}\right] & \left[K_{\phi t}^{e}\right] \end{pmatrix} \begin{Bmatrix} \{d^{e}\} \\ \{\phi^{e}\} \\ \{\theta_{t}\} \end{Bmatrix} = \begin{Bmatrix} \{F^{e}\} \\ \{G^{e}\} \end{Bmatrix} \tag{3.72}$$

where

$$\left[M_{uu}^{e}\right] = \int_{V} \rho \left[N^{T}\right][N] dV \tag{3.73}$$

After assembling the elemental stiffness matrices, the global dynamic finite element equations can be expressed as

$$\begin{pmatrix} [M_{uu}] & [0] & [0] \\ [0] & [0] & [0] \end{pmatrix} \begin{Bmatrix} \{\ddot{d}\} \\ \{\ddot{\phi}\} \\ \{\ddot{\theta}_{t}\} \end{Bmatrix} + \begin{pmatrix} [K_{uu}] & [K_{u\phi}] & -[K_{ut}] \\ [K_{\phi u}] & [K_{\phi\phi}] & [K_{\phi t}] \end{pmatrix} \begin{Bmatrix} \{d\} \\ \{\phi\} \\ \{\theta_{t}\} \end{Bmatrix} = \begin{Bmatrix} \{F\} \\ \{G\} \end{Bmatrix} \tag{3.74}$$

where the matrices are defined in subsection 3.4.9.1.

3.4.10 Finite element equations for electromechanical analysis

The global static electromechanical finite element equations are obtained by substituting the temperature increment vector $\{\theta_t\}$=0 into the static piezothermoelastic Eq. (3.62) as

$$\begin{bmatrix} [K_{uu}] & [K_{u\phi}] \\ [K_{\phi u}] & [K_{\phi\phi}] \end{bmatrix} \begin{Bmatrix} \{d\} \\ \{\phi\} \end{Bmatrix} = \begin{Bmatrix} \{F\} \\ \{G\} \end{Bmatrix} \tag{3.75}$$

Similarly, the global dynamic electromechanical finite element equations are obtained by substituting $\{\theta_t\}$=0 into the dynamic piezothermoelastic Eq. (3.74) as

$$\begin{pmatrix} [M_{uu}] & 0 \\ 0 & 0 \end{pmatrix} \begin{Bmatrix} \{\ddot{d}\} \\ \{\ddot{\phi}\} \end{Bmatrix} + \begin{pmatrix} [K_{uu}] & [K_{u\phi}] \\ [K_{\phi u}] & [K_{\phi\phi}] \end{pmatrix} \begin{Bmatrix} \{d\} \\ \{\phi\} \end{Bmatrix} = \begin{Bmatrix} \{F\} \\ \{G\} \end{Bmatrix} \tag{3.76}$$

CHAPTER 4

Genetic Algorithms for Optimal Actuators Placement and Control

This chapter describes the development of a methodology where genetic algorithm (GA) has been used for optimal placement of actuators as well as design of linear quadratic regulator (LQR) optimal controller of a smart structures. An improved integer coded genetic algorithm (GA) based open loop procedure has been implemented for optimal placement of actuators in order to maximize modal control forces. Control spillover of the higher modes has been incorporated to prevent closed loop instability by minimizing the modal control force of the higher modes. Once, the optimal actuator locations have been obtained, an improved real coded GA based LQR control scheme has been developed for designing an optimal controller in order to maximize the closed loop damping ratio while keeping actuators voltages within the permissible limit of actuator voltage.

4.1 Genetic algorithms (GA)

GA is a powerful and broadly applicable stochastic search and optimization technique based on the principles of natural selection and genetics. The current framework of GAs was first proposed by Holland [166] and his student Jong [167], and was finally popularized by another of his students, Goldberg [168]. Genetic algorithms were first proposed as adaptive search algorithms, although they have mostly been used as a global optimization algorithm for combinatorial and numerical problems. The working mechanism of canonical or simple genetic algorithm is shown in Fig.4.1. In the recent years, GAs have been extensively used for optimization of engineering problems due to its many advantages

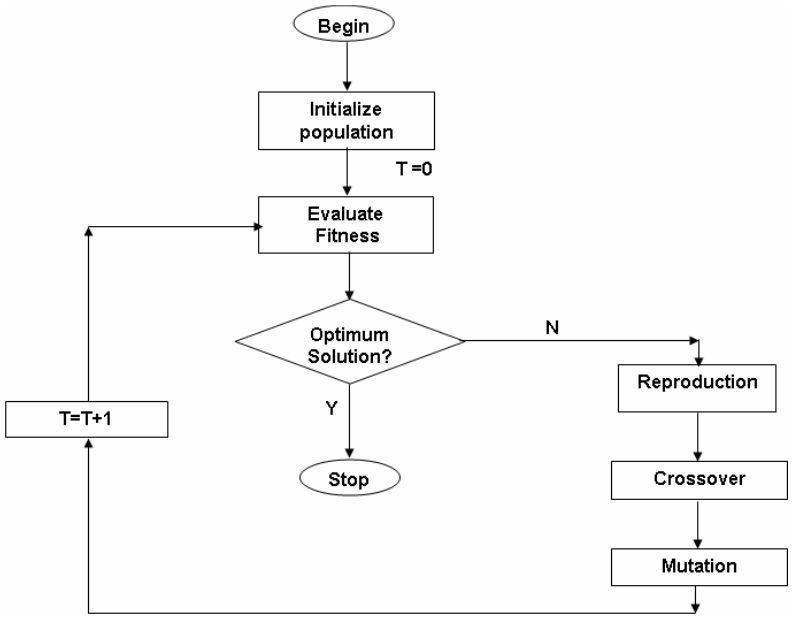

Fig. 4.1 A framework of simple genetic algorithm

compared to classical optimization techniques such as it is blind search method and highly parallel.

It is important for problem solution to select proper encoding. Encoding represents transformation of solved problem to *N*-dimensional space of real (integer) numbers. GA begins with a population of randomly generated candidates and evolves towards a solution by applying genetic operators such as reproduction, crossover and mutation. These three operators are simple and straightforward. Reproduction operator selects good strings and crossover operator recombines good substrings from two good strings together to hopefully form a better substring. Mutation operator alters a string locally to hopefully create a better string. Even though none of these claims are guaranteed and/or tested during a GA generation, it is expected that if bad strings are created they will be eliminated by the reproduction operator in the next generation and if good strings are created, they will be emphasized. Various encodings and GA operators have been discussed below.

4.1.1 Encoding

The choice of genetic coding is also very important depending on the continuous or discrete search space. In solving problems having continuous search space using binary coded GAs binary strings are usually chosen to code the problem variables. When binary (discrete) coding is used for continuous search space, a number of difficulties arise. One difficulty is the Hamming cliffs associated with certain string, from which a transition to a neighboring solution (in real space) requires alteration of many bits. Hamming cliffs in the binary coding cause artificial hindrance to gradual search in the continuous search space. The other difficulties are the inability to achieve any arbitrary precision and decoding. In binary coded GAs, the string length must be chosen a priori to enable GAs to achieve a certain precision in the solution. More is the required precision, the larger is the string length. For large string, the population size requirement is also large, thereby increasing the computational complexity of the algorithm. Since fixed, mapped coding is used, the variables bounds must be such that they bracket the optimal variable value. Since in many problems, this information is not usually known a priori, this may cause some difficulty in using binary coded GAs in those problems. For more discrete space such as actuators/sensors positioning in the smart structures integer coded genetic algorithm will be more efficient than binary coded genetic algorithm because binary coded will lead to increased string length as well as computational time especially in the large-scale structures where possible combination sensors/actuators is large. Gray coded genetic algorithm is also available in the literature [117] for placement of sensors/actuators. In essence, a Gray code

takes a binary sequence depending on the binary string of length. To avoid the problems associated with binary coded GAs for continuous space searching, many real coded GAs were developed. Apart from these, simulated binary crossover and probability-based mutation real coded genetic algorithm can completely overcome the difficulties associated with binary coded genetic algorithm. One of the main advantage of this type of real coded GA is that it can search in continuous space with or without variables bounds by creating extended or contracted children solutions in space automatically.

4.1.2 Reproduction operator

The primary objective of the reproduction operator is to emphasize good solutions and eliminate bad solutions in a population, while keeping the population size constant. This is achieved by performing the following tasks as

i) Identify good (usually above-average) solutions in a population.

ii) Make multiple copies of good solutions.

iii) Eliminate bad solutions from the population so that multiple copies of good solutions can be placed in the population. There exist a number of ways to achieve the above tasks. Some common methods are tournament selection, proportionate selection, ranking selection and roulette wheel selection.

4.1.3 Crossover operator

The reproduction operator cannot create any new solutions in the population. It only makes more copies of good solutions at the expense of not-so-good solutions. Creation of new solutions is performed in crossover and mutation operators. Like reproduction operator, there exists a number of crossover operators in the GA literature, but in almost all crossover operators, two strings are picked from the mating pool at random and some portion of the strings are exchanged between the strings. In a single-point crossover operator, this is performed by randomly choosing a crossing site along the string and by exchanging all bits on the right side of the crossing site. For example, a single point crossover of binary coded GA has been considered. If parents are **10001001110010010 and 01010001001000011** then their offspring will be **1000100101000011 and 0101000110010010** by choosing a random bit along the length of the chromosome, and swap all the bits after that point.

4.1.4 Mutation operator

Crossover operator is mainly responsible for the search aspect of genetic algorithms, even though mutation operator is also used for this purpose sparingly. The need for mutation is to keep diversity in the population. For binary encoding chromosome, mutation can be performed by switching a few randomly chosen bits from 1 to 0 or from 0 to 1. For

example, a new offspring after mutation can be represented as 10**1**01001101000011 of original offspring 10001001101000011.

4.2 State-space representation

In control engineering, state space representation is a mathematical model of a physical system as a set of input, output and state variables related by first-order differential equations. To abstract from the number of inputs, outputs and states, the variables are expressed as vectors and the differential and algebraic equations are written in matrix form (the last one can be done when the dynamical system is linear and time invariant). The state space representation (also known as the "time-domain approach") provides a convenient and compact way to model and analyze systems with multiple inputs and outputs.

The global set of dynamic equations for piezo-thermo-elastic analysis rewritten as

$$[M_{uu}]\{\ddot{d}\}+[K_{uu}]\{d\}+[K_{u\phi}]\{\phi\}-[K_{ut}]\{\theta_t\}=\{F\} \tag{4.1}$$

$$[K_{\phi u}]\{d\}+[K_{\phi\phi}]\{\phi\}+[K_{\phi t}]\{\theta_t\}=\{G\} \tag{4.2}$$

The coupled piezoelectric static equations can be written by taking the thermal strain effect and the pyroelectric effect as force vectors on the right hand side as follows

$$[K_{uu}]\{d\}+[K_{u\phi}]\{\phi\}=\{F\}+[K_{ut}]\{\theta_t\} \tag{4.3}$$

$$[K_{\phi u}]\{d\}+[K_{\phi\phi}]\{\phi\}=\{G\}-[K_{\phi t}]\{\theta_t\} \tag{4.4}$$

For open electrodes, charge can be expressed as

$$\{G\}=0 \tag{4.5}$$

Static displacement can be calculated due to only thermal loading from

$$\begin{bmatrix}[K_{uu}] & [K_{u\phi}]\\ [K_{\phi u}] & [K_{\phi\phi}]\end{bmatrix}\begin{Bmatrix}\{d_{th}\}\\ \{\phi\}\end{Bmatrix}=\begin{Bmatrix}[K_{ut}]\{\theta_t\}\\ -[K_{\phi t}]\{\theta_t\}\end{Bmatrix} \tag{4.6}$$

where, $\{d_{th}\}$ is the vector for nodal displacements considering only thermal loading. Dynamic responses of piezolaminated structures can be calculated due to only dynamic loading from

$$[M]\{\ddot{d}_{dy}\}+[K]\{d_{dy}\}=\{F\}-[K_{u\phi a}]\{\phi_a\} \tag{4.7}$$

where $[M]$ is the overall global mass matrix, $[K]$ is the overall global elastic stiffness matrix and $[K_{u\phi a}]$ is the global piezoelectric coupling matrices of actuator patches. The

nodal dynamic displacement vector $d_{dy}(t)$ can be approximated by the modal superposition of the first 'r' modes as

$$\{d_{dy}(t)\} \approx [\psi]\{\eta(t)\} \tag{4.8}$$

where $[\psi] = [\psi_1\ \psi_2 ... \psi_r]$ is the truncated modal matrix. The decoupled dynamic equations (Eq. (4.7)) considering modal damping can be written as

$$\left\{\ddot{\eta}_i(t)\right\} + 2\xi_{di}\omega_i\left\{\dot{\eta}_i(t)\right\} + \omega_i^2\left\{\eta_i(t)\right\} = [\psi]^T\{F\} - [\psi]^T[K_{ua}]\{\phi_a\} \tag{4.9}$$

where ξ_{di} is the damping ratio.

Eq. (4.9) can be represented in state-space form as

$$\left\{\dot{X}\right\} = [A]\{X\} + [B]\{\phi_a\} + \left[\hat{B}\right]\{u_d\} \tag{4.10}$$

where,

$[A] = \begin{bmatrix} [0] & [I] \\ [-\omega_i^2] & [-2\xi_{di}\omega_i] \end{bmatrix}$ is the system matrix, $[B] = \begin{bmatrix} [0] \\ -[\psi]^T[K_{ua}] \end{bmatrix}$ is the control matrix,

$\left[\hat{B}\right] = \begin{bmatrix} [0] \\ [\psi]^T\{F\} \end{bmatrix}$ is the disturbance matrix, $\{u_d\}$ is the disturbance input vector, $\{\phi_a\}$ is the control input, and

$$\left\{\dot{X}\right\} = \begin{Bmatrix} \dot{\eta} \\ \ddot{\eta} \end{Bmatrix} \text{ and } \{X\} = \begin{Bmatrix} \eta \\ \dot{\eta} \end{Bmatrix} \tag{4.11}$$

Two types of sensor output equations have been considered for mechanical and thermo-mechanical loading. The sensor output equation [153] for mechanical loading can be written as

$$\{y\} = [C_0]\{X\} \tag{4.12}$$

where output matrix $[C_0]$ depends on the modal matrix $[\psi]$ and the sensor coupling matrix $\left[K_{\phi us}\right]$. The sensor output equation for thermo-mechanical loading has been proposed as

$$\{y\} = -\left[K_{\phi\phi s}\right]^{-1}\left[\left[K_{\phi us}\right]\ \left[K_{\phi ts}\right]\right]\begin{Bmatrix}\{d_{com}\} \\ \{\{\theta_t\}\}\end{Bmatrix} \tag{4.13}$$

where $\left[K_{\phi\phi s}\right]$ and $\left[K_{\phi ts}\right]$ are the global dielectric and electro-thermal stiffness matrices of sensor patches respectively and $\{d_{com}\}$ is the combined displacement and it can be written as

$$\{d_{com}\} = \{d_{dy}\} + \{d_{th}\} \tag{4.14}$$

4.3 Controllability index for actuator location

The system controllability is a basis in the modern control theory. Wang and Wang [97] proposed a controllability index for actuator locations, which was obtained by maximizing the global control force, and this has been considered in the present study. The modal control force f_c applied to the system can be written as

$$\{f_c\} = [B]\{\phi_a\} \tag{4.15}$$

It follows from Eq. (4.15) that

$$\{f_c\}^T \{f_c\} = \{\phi_a\}^T [B]^T [B]\{\phi_a\} \tag{4.16}$$

Using the singular value analysis, $[B]$ can be written as $[B] = [M][S][N]^T$

where $[M]^T [M] = [I]$, $[N]^T [N] = [I]$ and $[S] = \begin{bmatrix} \sigma_1 & \text{K} & 0 \\ 0 & \text{O} & \text{M} \\ \text{M} & \text{K} & \sigma_{n_a} \\ 0 & \text{K} & 0 \end{bmatrix}$

where n_a is the number of actuators. Equation (4.15) can be rewritten as

$$\{f_c\}^T \{f_c\} = \{\phi_a\}^T [N][S]^T [S][N]^T \{\phi_a\} \quad \text{or} \quad \|\{f_c\}\|^2 = \|\{\phi_a\}\|^2 \|S\|^2 \tag{4.17}$$

Thus, maximizing this norm independently on the input voltage $\{\phi_a\}$ induces maximizing $\|S\|^2$. The magnitude of σ_i is a function of location and the size of piezoelectric actuators. Wang and Wang [97] proposed that the controllability index is defined by

$$Maximize\ \Omega = \prod_{i=1}^{n_a} \sigma_i \tag{4.18}$$

The higher the controllability index, the smaller will be the electrical potential required for control. The control spillover effects are a significant problem of active vibration control implementation on real structures. Therefore, a similar controllability index has been proposed in the present work incorporating residual modes of system/structures as follows

$$Maximize\ \Omega = \prod_{i=1}^{n_a} \sigma_i - \gamma' \prod_{i=1}^{n_a} \sigma_i^R \tag{4.19}$$

where σ_i^R are the components of $[S^R]$ corresponding to residual modes and γ' is a weight constant.

4.4 LQR optimal feedback control

Linear quadratic regulator (LQR) optimal control theory has been used to determine the control gains. In this, the feedback control system has been designed to minimize a cost function or a performance index, which is proportional to the required measure of the system's response. The cost function [146] used in the present case is given by

$$J = \frac{1}{2}\int_{t_0}^{t_f} (\{y\}^T[Q]\{y\} + \{\phi_a\}^T[R]\{\phi_a\})dt \tag{4.20}$$

where $[Q]$ and $[R]$ are the semi-positive-definite and positive-definite weighting matrices on the outputs and control inputs, respectively.

Minimization of J leads to the steady-state matrix Ricatti equation as

$$[A]^T[K] + [K][A] - [K][B][R]^{-1}[B]^T[K] + [C]^T[Q][C] = 0 \tag{4.21}$$

After solving the Ricaati equation using Potters method [169], optimal gain can be written as

$$[G_c] = [R]^{-1}[B]^T[K] \tag{4.22}$$

Considering the output feedback, actuation voltage can be calculated as

$$\{\phi_a\} = -[G_c]\{y\} \tag{4.23}$$

4.4.1 Determination of weighting matrices

Weighting matrices $[Q]$ and $[R]$ are important components of LQR control process and compositions of $[Q]$ and $[R]$ elements influence the system's performance. Commonly, trial and error methods have been used to find for these weighting matrices. Lewis [170] assumed $[Q]$ and $[R]$ to be a semi-positive definite and positive definite matrix respectively. Ang et al. [142] proposed that $[Q]$ and $[R]$ matrices could be determined considering weighted energy of the system as follows

$$[Q] = \begin{bmatrix} \alpha_2[\psi]^T[K][\psi] & [0] \\ [0] & \alpha_1[\psi]^T[M][\psi] \end{bmatrix}, \text{and } [R] = \gamma[\hat{R}] \tag{4.24}$$

The proposed weighted energy of the system in the quadratic form is

$$\bar{\Pi} = \frac{1}{2}\alpha_1\{\dot{X}\}^T[M]\{\dot{X}\} + \frac{1}{2}\alpha_2\{X\}^T[K]\{X\} + \frac{1}{2}\gamma\{\phi_a\}^T[\hat{R}]\{\phi_a\} \tag{4.25}$$

where, α_1, α_2 and γ are the coefficients associated with total kinetic energy, strain energy and input energy respectively. These coefficients will take different values in the control algorithm apart from the value of unity to allow for the relative importance of these energy terms. The closed loop damping values can be calculated by using the following equation.

$$\ln\left(\frac{d_{com}(t_i)}{d_{com}(t_{i+1})}\right)=\frac{2\pi\xi_d}{\sqrt{(1-\xi_d{}^2)}} \tag{4.26}$$

Therefore, a search algorithm is required for finding [Q] and [R] by taking α_1,α_2 and γ as variables, which will give maximum control response within the allowable actuators voltage. In this present study, optimization problem has been proposed as follows

$$Maximize\ \xi_d=\frac{1}{\sqrt{\left(1+\frac{4\pi^2}{p^2}\right)}} \tag{4.27}$$

Subjected to $\phi_i<\phi_{max}, i=1,...n_a$

where $p=\ln\left(\frac{d_{com}(t_i)}{d_{com}(t_{i+1})}\right)$, n_a is the number of actuators and ϕ_{max} refers to the maximum voltage that can be applied on the actuators depending on the piezoelectric materials and thickness of the piezolayers. The allowable voltage of piezo-ceramic materials is around 500-1000 V per 1 mm piezo thickness [171].

4.5 GA for optimal placement

Most natural representation in the form of a string of integers specifying the locations of actuators has been used in this study. An integer coded genetic (ICGA) algorithm with uniform crossover and mutation have been developed for optimal placement of actuators. In the present problem, the design variables are the positions of the actuators, and are represented in a string of integers specifying the locations of actuators. The gene code is taken as $ac_1,ac_2,.....,ac_j,.....,ac_{n_a}$, where $ac_j\in(1,m)$ and is a positive integer number and m is the total number of locations for actuators in the structures/system. Uniform crossover and new mutation techniques for integer coded genetic algorithm have been discussed in the following subsections.

4.5.1 Uniform crossover

The steps involve in this crossover are

a) A random mask is generated
b) The mask determines which bits are copied from one parent and which from the other parent
c) Bit density in mask determines how much material is taken from the other parent

For example, if the randomly generated mask is 0110011000 and parents are1010001110 and 0011010010 then their offspring will be 0011001010 and 1010010110.

4.5.2 Mutation

A one-digit positive integer value $ac_j \in [1, m]$ is generated at random, which replaces the old one when mutating. If ac_j is equal to old one, then a new positive integer is selected again until they are different in the chromosome. The efficiency of the mutation could be improved greatly using the method.

4.6 Optimal placement

The fitness value i.e. measure of controllability for the optimal actuators location has been proposed as follows

$$\Omega = \left\{ \begin{array}{l} \prod_{i=1}^{n_a} \sigma_i, \ without\ control\ spillover \\ \left\{ \begin{array}{l} \left(\prod_{i=1}^{n_a} \sigma_i - \gamma' \prod_{i=1}^{n_a} \sigma_i^R \right) \ if \ \left(\prod_{i=1}^{n_a} \sigma_i \right) > \left(\gamma' \prod_{i=1}^{n_a} \sigma_i^R \right) \\ \left(\prod_{i=1}^{n_a} \sigma_i - \gamma' \prod_{i=1}^{n_a} \sigma_i^R \right) \times 10^{-12}, \ otherwise \end{array} \right\}, considering\ control\ spillover \end{array} \right\} \quad (4.28)$$

The outline of optimization problem using IGA is as follows:

i) Initial chromosomes depending on the number of actuators and populations are chosen randomly.

ii) The fitness value (measure of controllability) is calculated for each chromosome.

iii) Genetic operators are applied to produce a new set of chromosomes.

iv) Steps (ii) to (iii) are repeated until the fitness converge

v) The computation is terminated after convergence of fitness and the chromosome based on the best controllability value is selected as the optimal locations of actuators.

4.7 GA for LQR control scheme

In the present study, real coded genetic algorithm along with simulated binary crossover (SBX) and parameter based mutation [172] operators have been used to search optimal weighting matrices for designing conventional LQR control scheme. In the following subsections, these operators have been briefly described.

4.7.1 Simulated binary crossover (SBX)

A probability distribution function has been used around the parent solutions to create two children solutions as

$$P(\beta) = \begin{array}{ll} 0.5(\eta_c + 1)\beta^{\eta_c} & if\ \beta \le 1, \\ 0.5(\eta_c + 1)/\beta^{\eta_c + 2} & otherwise \end{array} \quad (4.29)$$

where

$$\beta = \left| \frac{b^{(2)} - b^{(1)}}{a^{(2)} - a^{(1)}} \right|$$

and $b^{(1)}$, $b^{(2)}$ are the children solutions, and $a^{(1)}$, $a^{(2)}$ are the parent solutions. η_c is a parameter which controls the extent of spread in children solution. A small value of η_c allows solutions far away from parents to be created as children solutions and a large value restricts only near-parent solutions to be created as children solutions. In the most of the literature, the small and large values of η_c are taken as 2 and 5 respectively [172]. A self-adaptive procedure for updating η_c parameter can also be used for calculating this parameter [173]. The procedure adopted for computing children solution $b^{(1)}$ and $b^{(2)}$ from parent solutions $a^{(1)}$ and $a^{(2)}$ are as follows:

1. A random number u between 0 and 1 has been generated

2. Parameter $\bar{\beta}$ has been found using the polynomial probability distribution (Eq. (4.29)) and $\bar{\beta}$ can be written as

$$\bar{\beta} = \begin{cases} (\alpha u)^{\frac{1}{\eta_c+1}}, & \text{if } u \le 1/\alpha, \\ (1/2-\alpha u)^{\frac{1}{\eta_c+1}}, & \text{otherwise} \end{cases} \tag{4.30}$$

where $\alpha = 2 - \beta^{-(\eta_c+1)}$ and β is calculated as follows

$$\beta = 1 + \frac{2}{a^{(u)} - a^{(l)}} \min[(a^{(1)} - a^{(l)}), (a^{(u)} - a^{(2)})] \tag{4.31}$$

where a^l and a^u are lower and upper bounds of a variable.

3. The children solutions are then calculated as follows

$$b^{(1)} = 0.5[(a^{(1)} + a^{(2)}) - \bar{\beta}\left|a^{(2)} - a^{(1)}\right|] \tag{4.32}$$

$$b^{(2)} = 0.5[(a^{(1)} + a^{(2)}) + \bar{\beta}\left|a^{(2)} - a^{(1)}\right|] \tag{4.33}$$

4.7.2 Parameter-based mutation operator

A polynomial probability distribution has been used to create a solution b in the vicinity of a parent solution using the following procedure

1. A random number u between 0 and 1 has been generated

2. The parameter $\bar{\delta}$ is calculated as follows

$$\bar{\delta} = \begin{cases} [2u + (1-2u)(1-\delta)^{\eta_m+1}]^{\frac{1}{\eta_m+1}} - 1, & \text{if } u \le 0.5, \\ (1 - [2(1-u) + 2(u-0.5)(1-\delta)^{\eta_m+1}]^{\frac{1}{\eta_m+1}}), & \text{otherwise} \end{cases} \tag{4.34}$$

where $\delta = \min[(a-a^l),(a^u-a)]/(a^u-a^l)$

η_m is the distribution index for the mutation and takes any non-negative value.

3. The mutated child is calculated as follows

$$b = a + \bar{\delta}\ \Delta_{\max} \tag{4.35}$$

where, $\Delta_{\max}$ is maximum perturbation allowed in the parent solution. By setting, $\Delta_{\max} = a^u - a^l$, the expected normalized perturbation can be calculated from Eq. (4.35) as $(b-a)/(a^u-a^l)$

It has been observed that this order is $O(1/\eta_m)$ [172]. Thus, in order to get a mutation effect of 1% perturbation η_m has been taken as 100.

4.8 The GA approach to optimal LQR

In the present work, weighting matrices have been determined by the genetic search to obtain best control gain for the optimal LQR scheme. Parameters α_1, α_2 and γ in Eq. (4.23) have been represented by real-valued genes for finding [Q] and [R] matrices. The fitness value has been calculated with respect to each chromosome using the following expression.

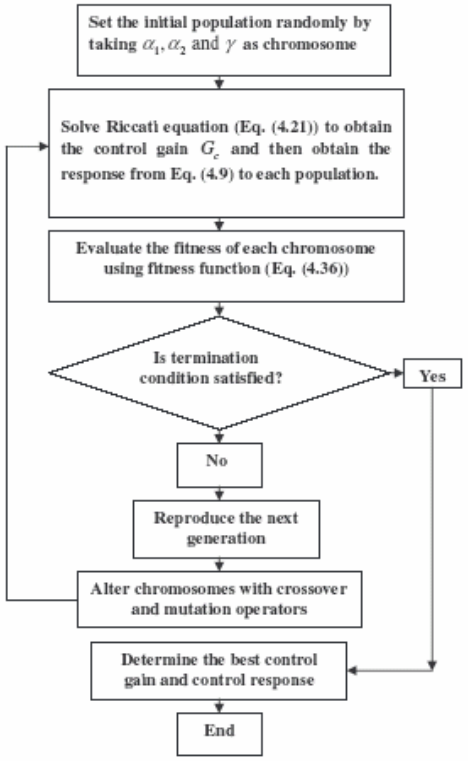

Fig. 4.2 Flowchart of GA based LQR

$$\xi_d = \begin{cases} \left(\dfrac{1}{\sqrt{\left(1+\dfrac{4\pi^2}{p^2}\right)}}\right), & if\ \ \phi_i < \phi_{max} \\ \left[10^{-8} \times \left(\dfrac{1}{\sqrt{\left(1+\dfrac{4\pi^2}{p^2}\right)}}\right)\right], & otherwise \end{cases} \tag{4.36}$$

Fig. 4.2 shows the steps in determining the weighting matrices for optimal gain by real coded GA in the present problem. The ranges of α_1, α_2 and γ are taken as

$0 < \alpha_1 \leq 300$, $0 < \alpha_2 \leq 300$ and $0 < \gamma \leq 2$ where controlled response depends on α_1, α_2 and γ. Parents have been selected through roulette wheel operator and offspring have been created using simulated binary crossover and polynomial mutation operator [172]. The distribution parameters associated with simulated binary crossover and polynomial mutation operator have been taken as $\eta_c = 2$ and $\eta_m = 100$. Genetic evolution has been continued for large number of generations till the fitness converges.

CHAPTER 5

Validation and Thermo-Electro-Mechanical Responses of Smart FRP Composite Shell Structures

This chapter first presents the validation of the computer code developed which is capable of finite element analysis of smart shell structures subjected to thermo-electro-mechanical loading, determination of optimal actuators placement using GA and GA based LQR control scheme for active vibration control of such structures. After validation of entire code, different smart composite shell structures have been analyzed to study coupled thermo-electro-mechanical responses under thermal loading.

5.1 Computer code validation

Based on the finite element formulations discussed in chapter 3, an improved layered shell finite element code has been developed for thermo-electro-mechanical analysis of piezo embedded smart FRP composite shell structures. Based on the methodology described in chapter 4, a code incorporating an improved integer coded GA based optimal placement of actuators including control spillover has been developed which gets required system matrices from the shell FE code. Finally, a code has been developed for improved real coded GA based LQR control scheme for simulation of optimal active vibration control of smart shell structures. This code gets its required thermo-electro-mechanical responses from the FE code. These three codes integrated lead to a complete module for analysis and design for active vibration control of smart FRP composite shell structures with the following key features.

i) The developed code is capable of analyzing smart FRP composite shell structures under any kind of possible loading such as thermal, electrical, mechanical or any combination of these with or without pyroelectric effect.

ii) The code is capable of evaluating optimal placement of actuators and/or sensors on different kind of smart FRP shells structures considering control spillover.

iii) The code is also capable of simulation of optimal active vibration control for any smart FRP structures under the action of mechanical as well as thermo-mechanical loading in order to maximize closed loop damping ratio within the limit of actuators voltage.

The developed computer code has been validated for all possible kinds of load cases before using the same for analysis and design of smart shell structures.

5.1.1 Structural validation

In order to verify the shell finite element code developed, the static and free vibration analysis have been carried out for the doubly curved laminated composite shell panels having spherical and ellipsoidal shapes. A 10×10 finite element mesh has been used to model both the shell panels. The material properties of structural laminae considered for this analysis are listed in the Table 5.1. Nondimensionalized central deflection (w^a) of the laminated spherical and ellipsoidal GR/E shells under distributed load of 10^5 N/m^2 and nondimensionalized fundamental frequency (λ^{**}) has been calculated using the present shell finite element code and compared with those obtained from already published results [165] as follows

Table 5.1 Material properties for Gr/Epoxy lamina [169]

E_1 (GPa)	300
E_2 (GPa)	12
$G_{12} = G_{13}$ (GPa)	6
G_{23} (GPa)	2.4
ρ (kg/m^3)	7800

$$w^a = (wh^3E_2/qa^4)\times 10^3 \text{ and } \lambda^{**} = \frac{\lambda a^2}{h}\sqrt{\rho/E_2} \tag{5.1}$$

where, h = total thickness of laminate and a = length of the structure along x axis.

5.1.1.1 Spherical laminated composite shell

A simply supported cross-ply laminated GR/E composite spherical shell has been considered. Geometry of this layered spherical shell panel is shown in Fig 5.1. In Fig. 5.1, '*R*' is the radius of curvature of the shell structure and '*a*' is the length of the structure along x axis. Analysis has been done on three different types of laminates on square base ($a = b$) for static analysis as well as free vibration. Table 5.2 shows non-dimensional central deflections of laminated spherical shell for different *R/a* ratios and *a/h* ratios compared with analytical solutions [165, 174]. It could be observed that the results obtained from the present finite element code are very close to those obtained from published analytical solutions [165, 174]. For the same spherical shell, free vibration analysis has also been carried out and the non-dimensional fundamental frequencies obtained from the present code have been

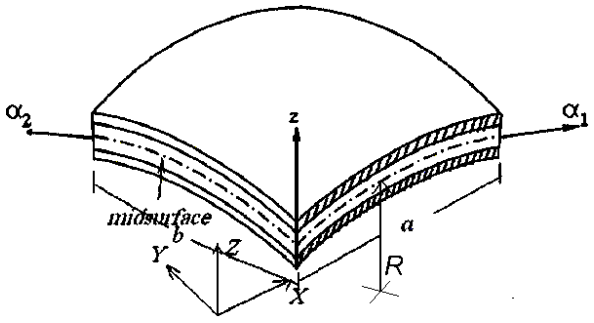

Fig 5.1. Geometry of layered composite shell panel

compared with the analytical solution [165, 174] as listed in Table 5.4 for different *R/a* and *a/h* ratios. It could be observed that the results obtained from the present finite element code agree well with the results obtained from the analytical solutions [165, 174].

Table 5.2 Comparison of nondimensionalized central deflection (w^a) of spherical shell panel

Panel type	*a/h*	Sources	*R/a*							
			1	2	5	10	20	50	100	Plate
0/90	10	Present FE	6.1897	13.3926	18.2008	19.1396	19.3892	19.4570	19.4929	19.469
		Refs [165,174]	6.0540	12.6680	17.9940	19.0690	19.3650	19.4520	19.4640	19.469
	100	Present FE	0.0689	0.2844	1.7539	5.5459	11.2677	15.7265	16.6956	16.980
		Refs [165,174]	0.0718	0.2855	1.7535	5.5428	11.273	15.714	16.645	16.980
0/90/0	10	Present FE	4.9344	8.9201	9.9962	10.1628	10.2051	10.2182	10.2216	10.222
		Refs [165,174]	4.8173	8.021	9.7937	10.110	10.191	10.214	10.218	10.220
	100	Present FE	0.0692	0.2864	1.5218	3.6590	5.5470	6.4937	6.6602	6.696
		Refs [165,174]	0.0718	0.2858	1.5118	3.6445	5.5473	6.4827	6.6421	6.697
$[0/90]_S$	10	Present FE	4.9754	8.8573	10.0074	10.1887	10.2352	10.2504	10.2556	10.256
		Refs [165,174]	4.8366	8.0517	9.8249	10.141	10.222	10.245	10.249	10.251
	100	Present FE	0.0694	0.2852	1.5443	3.7304	5.6683	6.6162	6.7806	6.8335
		Refs [165,174]	0.0715	0.2844	1.5358	3.7208	5.6618	6.6148	6.7772	6.8331

Table 5.3 Comparison of nondimensional fundamental frequency (λ^{**}) for spherical shell

Panel type	*a/h*	Source	*R/a*							
			1	2	5	10	20	50	100	Plate
0/90	10	Present FE	13.9840	10.4314	9.1653	8.9665	8.9158	8.8997	8.8947	8.8933
		Refs [165,174]	14.481	10.749	9.2302	8.9841	8.9212	8.9035	8.9009	8.9001
	100	Present FE	124.7504	67.3346	28.8106	16.6968	11.8396	10.0579	9.7673	9.6549
		Refs [165,174]	125.93	67.369	28.826	16.706	11.841	10.063	9.7825	9.6873
0/90/0	10	Present FE	15.5501	12.6854	12.2485	12.1843	12.1679	12.1626	12.1609	12.160
		Refs [165,174]	16.115	13.382	12.372	12.215	12.176	12.165	12.163	12.162
	100	Present FE	123.8227	67.8001	30.9009	20.3108	16.6169	15.4180	15.2397	15.179
		Refs [165,174]	125.99	68.075	30.993	20.347	16.627	15.424	15.244	15.183
$[0/90]_S$	10	Present FE	15.5219	12.8041	12.3228	12.2511	12.2327	12.2262	12.2237	12.223
		Refs [165,174]	16.172	13.447	12.437	12.280	12.240	12.229	12.228	12.226
	100	Present FE	124.607	68.0221	30.9921	20.3473	16.6284	15.4216	15.2353	15.179
		Refs [165,174]	126.33	68.294	31.079	20.38	16.638	15.426	15.245	15.184

5.1.1.2 Ellipsoidal laminated composite shell

The static analysis has also been carried out for the simply supported cross-ply ellipsoidal laminated composite shell. The ellipsoidal shell panel has been considered with major axis length $2\times R$ and minor axis length $1.5\times R$ on the square base ($a = b$) and non-dimensional central deflections are listed in the Table 5.3 for thick (a/h =10) and thin (a/h =100) ellipsoidal laminated shells for different R/a ratios. In absence of analytical results, results obtained from the present shell finite element code are compared with already published FE results [61] and are observed to be very close. The free vibration analysis has

Table 5.4 Comparison of nondimensionalized central deflection (w^a) of ellipsoidal shell panel

Panel type	a/h	Sources	R/a							
			1	2	5	10	20	50	100	Plate
0/90	10	Present FE	3.5537	10.4216	17.2351	18.8809	19.3305	19.4596	19.4740	19.4789
		Ref [61]	3.4600	9.9417	16.991	18.804	19.307	19.447	19.465	19.469
	100	Present FE	0.03284	0.14578	0.92538	3.3632	8.5742	14.7213	16.3635	16.9863
		Ref [61]	0.0291	0.1391	0.9210	3.3603	8.5706	14.698	16.347	16.980
0/90/0	10	Present FE	3.4175	7.5389	9.6890	10.0820	10.1846	10.2145	10.2188	10.2198
		Ref [61]	3.1842	6.6467	9.4364	10.013	10.167	10.221	10.217	10.219
	100	Present FE	0.03346	0.14300	0.8395	2.5245	4.7770	6.2923	6.6003	6.6957
		Ref [61]	0.0294	0.1367	0.8312	2.5123	4.7662	6.2930	6.5913	6.6970
$[0/90]_S$	10	Present FE	3.4069	7.5680	9.7198	10.1130	10.2162	10.2463	10.2496	10.252
		Ref [61]	2.9665	6.7811	9.5005	10.053	10.200	10.242	10.248	10.250
	100	Present FE	0.03267	0.1431	0.8617	2.5953	4.8889	6.4193	6.7170	6.8295
		Ref [61]	0.0289	0.1362	0.8541	2.5849	4.8760	6.4236	6.7260	6.8331

been carried out for the same simply supported cross-ply ellipsoidal laminated composite shell. The non-dimensional fundamental frequencies obtained from the present code have been compared with the available FE solution [61] and listed in Table 5.5 for different ratios *of R/a* and *a/h*. From the results tabulated, it could be observed that the results obtained from the present finite element code are very close to the already published solutions [61]. The shell finite element formulation of the present work thus validated for both deep and shallow shells in spherical and ellipsoidal shells.

Table 5.5 Comparison of nondimensional fundamental frequency (λ^{**}) of ellipsoidal shell panel

Panel type	*a/h*	Source	*R/a*							
			1	2	5	10	20	50	100	Plate
0/90	10	Present FE	15.9897	11.4263	9.3472	9.0037	8.9200	8.8987	8.8949	8.8912
		Ref [61]	16.663	11.711	9.4135	9.0223	8.9255	8.9015	8.8993	8.9001
	100	Present FE	155.3043	89.9107	38.688	21.1971	13.5263	10.3933	9.8673	9.6859
		Ref [61]	157.44	90.879	38.755	21.209	13.531	10.399	9.8698	9.6873
0/90/0	10	Present FE	16.7912	13.3905	12.3811	12.2183	12.1766	12.1645	12.1619	12.162
		Ref [61]	18.085	14.226	12.540	12.259	12.187	12.167	12.164	12.163
	100	Present FE	156.7332	90.1427	40.1932	24.1116	17.8470	15.6411	15.2941	15.1754
		Ref [61]	159.45	91.405	40.349	24.157	17.861	15.643	15.300	15.183
$[0/90]_S$	10	Present FE	16.7809	13.4552	12.4454	12.2826	12.2407	12.2283	12.2271	12.2265
		Ref [61]	17.995	14.210	12.586	12.319	12.250	12.231	12.228	12.227
	100	Present FE	156.8187	90.3873	40.3145	24.1654	17.8649	15.6405	15.3005	15.1789
		Ref [61]	159.94	91.666	40.465	24.208	17.879	15.647	15.301	15.184

5.1.2 Electro-mechanical validation

In order to verify the accuracy of the present coupled electro-mechanical shell finite element code, the results obtained from the present code have been compared with the benchmark problem proposed by Smits et al [175]. Here, a cantilever bimorph (as shown in Fig. 5.2) made of two PVDF layers laminated together has been considered subjected to an external voltage. The induced internal stresses result in a bending moment which forces the bimorph beam to bend. In this case, the bimorph beam has been discretized into five elements using the shell FE, considering the dimensions of the beam as length, L = 100 mm, width, W = 5 mm and thickness, h = 1 mm. The analytical solution for the transverse displacement w is given by Smits et al [175] as

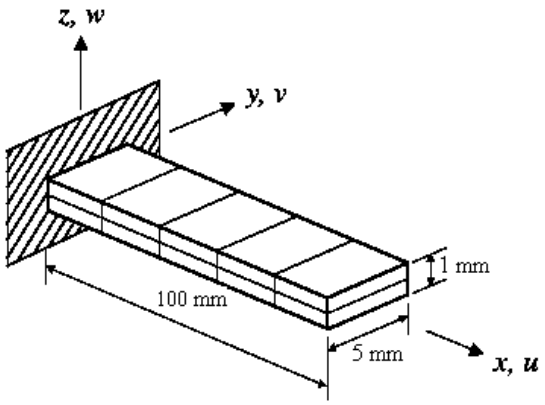

Fig.5.2 Schematic view of a bimorph beam

$$w = 1.5\frac{e_{31}\phi}{Eh^2}x^2 \tag{5.2}$$

A unit voltage has been applied across the thickness and the calculated transverse deflections at the five nodes obtained from the present code have also been compared with

Table 5.6 Transverse deflections of piezoelectric bimorph actuator

Distance (mm) from fixed end	Deflections (in μm)					
	Smits (Theory) [175]	Chee et al (Beam FE) [30]	Hwang and Park (Plate FE) [8]	Tzou and Ye (Shell FE) [28]	Detwiler et al Experiment [27]	Present (Shell FE)
20	0.0138	0.0138	0.0131	0.0132	-	0.0136
40	0.0552	0.0552	0.0545	0.0528	-	0.0540
60	0.1240	0.1242	0.1200	0.1190	-	0.1218
80	0.2210	0.2208	0.2180	0.2110	-	0.2150
100	0.3450	0.3450	0.3400	0.3300	0.315	0.3367

the results of Smits et al [175], Hwang and Park [8], Detwiler et al [27], Tzou and Ye [28] and Chee et al [30] as listed in Table 5.6. It could be observed from the table that the results from the present finite element code agree well with the already published results. Thus the coupled electro-mechanical formulation has been validated.

5.1.3 Validation for piezo-thermo-elastic analysis

Two types of problems have been used to validate the code for electro-thermo-mechanical analysis. Since no published results are available for piezo-thermo-elastic analysis of shells, the results for piezo-thermo-elastic analysis from the developed code has been

Table 5.7 Material properties of Gr/Epoxy and PVDF [63]

Properties	Graphite/epoxy	PVDF
E_1 (GPa)	181	2
E_2 (GPa)	10.3	2
ν_{12}	0.28	0.33
G_{12} (GPa)	7.17	0.752
G_{13} (GPa)	7.17	0.752
α_1 (/°C)	0.02×10^{-6}	22.5×10^{-6}
α_2 (/°C)	0.02×10^{-6}	22.5×10^{-6}
e_{31} (c/m^2)	----	0.068657
e_{32} (c/m^2)	----	0.068657
$\in_{33}$ (nF/m)	----	0.0106

validated with the available results of beams and plates. In the present code the radii of curvatures have been input as infinite to simulate the beam and plate behaviors. These are briefly described in the following subsections (5.1.3.1-5.1.3.2).

5.1.3.1 Static displacement of piezo-laminated plate

The piezo-thermo-elastic analysis of simply supported piezolaminated composite plate has been carried out to validate the present shell finite element code. A 4×4 finite element mesh has been considered. Material properties of graphite/epoxy and PVDF used in this study have been listed in Table 5.7. Only thermal load has been applied on the top and bottom surfaces of the plate. Temperatures at the top and bottom surfaces have been taken as 50ºC and 0ºC respectively. Central deflections of the plate obtained from the present code for various width/thickness ratios have been compared with the already published results for piezolaminated plate structure for analytical and finite element results of Jonnalagadda et al. [63] and are listed in Table 5.8. From the results listed in Table 5.8, it could be observed that the results obtained from the present shell finite element code agree well with the analytical as well as FE solution [63], showing the validation of coupled electro-thermo-mechanical formulation of the present work.

Table 5.8 Comparison of center deflection of piezo-laminated plate

b/h ratio	Center deflection of plate $\times 10^{-5}$ m		
	Jonnalagadda et al [63]		Present FEM
	Analytical results	FEM	
4	-0.676	-0.677	-0.677
10	-1.5834	-1.5849	-1.5805
40	-6.209	-6.2128	-6.1852

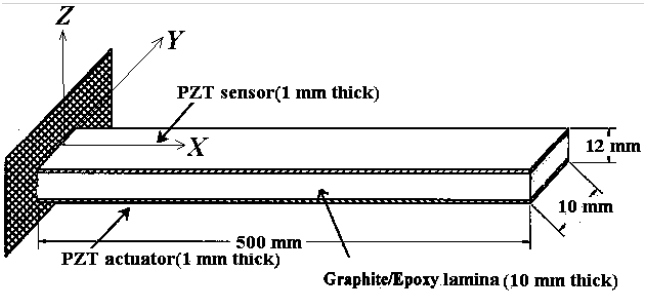

Fig.5.3 Piezolaminated beam structure

5.1.3.2 Thermo-electric analysis

Static analysis of piezolaminated beam has also been considered to validate eletro-thermal coupling effect in the present shell finite element formulation. Geometry of piezolaminated beam considered in this work has been shown in Fig 5.3. A three layer piezolaminated composite beam structure, consisting of two uniformly thick PZT layers on the top and the bottom of the laminate, respectively and the middle layer 90º of

Graphite/epoxy lamina, has been considered for the analysis. The top PZT layer has been considered as the sensor layer and the bottom PZT layer has been considered as the actuator layer. A 5×1 finite element mesh has been considered. Material properties of Graphite/epoxy and PZT layer used in this work have been listed in Table 5.9. Only thermal load has been applied on this beam structure. The induced sensor voltage has been calculated for both thermal strain effect and pyroelectric effect and has been validated with the available results [86]. The thermal load applied on the top surface is taken as 0ºC and on the bottom surface is taken as t_bºC. Fig 5.4 shows the closeness of the sensor voltage due to thermal strain effect to the results of Jiang and Li [86]. Fig 5.5 shows the closeness of the

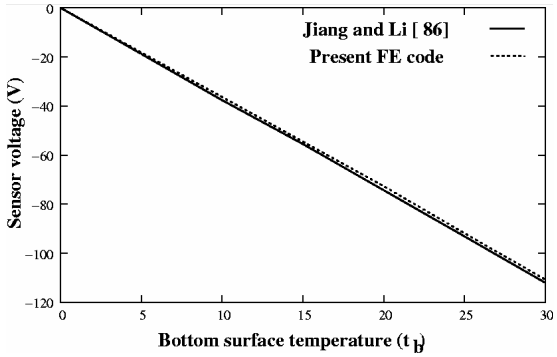

Fig.5.4 Sensor voltage due to thermal strain effect

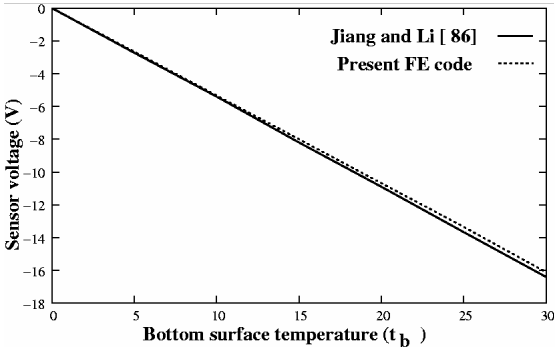

Fig.5.5 Sensor voltage due to pyroelectric effect

Table 5.9 Material properties of Gr/Epoxy and PZT [86]

Properties	Graphite/epoxy	PZT
E_1 (GPa)	181	60
E_2 (GPa)	10	60
ν_{12}	0.33	0.33
G_{12} (GPa)	8	22.5
G_{13} (GPa)	8	22.5
G_{23} (GPa)	3	22.5
α_1 (/ºC)	0.024×10^{-6}	1.2×10^{-6}
α_2 (/ºC)	24×10^{-6}	1.2×10^{-6}
e_{31} (c/m^2)	----	-20.75
e_{32} (c/m^2)	----	-20.75
P_3(cK^{-1}m^{-2})	----	-2.5×10^{-4}
$\in_{33}$ (nF/m)	----	15

induced sensor voltages due to pyroelectric effect to the results of Jiang and Li [86]. From Fig 5.4 and Fig 5.5 it could be observed that the induced sensor voltages due to the thermal strain effect as well as pyroelectric effect agree well with the already published results [86] thereby validating the present formulation.

5.1.4 Validation for optimal actuators placement

In order to ensure that the GA based methodology developed for optimal placement of the actuators actually converges to optimal solution and to compare the performance of binary coded and integer coded GA in searching the optimal solution, a [p/[0/0]$_s$/p]] cantilever beam having length L = 0.2 m and width B = 0.01 m has been considered. Thickness of the piezo-layer is taken as 0.5 mm and thickness of the each ply is taken as 0.15 mm. Here 'p' stands for piezo patches. Several important parameters for integer and binary coded GA have been listed in Table 5.10. The mechanical, electrical and coupled material properties [141] used in the present study have been listed in the Table 5.11. In this study, four actuators and first mode of vibration have been considered. Optimal actuators placement based on the maximum controllability index is shown in Fig. 5.6. It could be clearly observed from Fig.5.6, that the optimal locations of PZT actuators are on

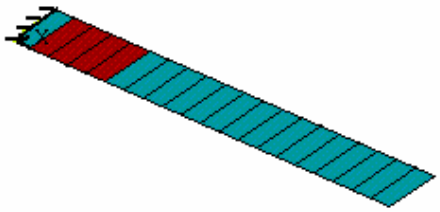

Fig.5.6 Optimal location of four actuators on the cantilever beam based on maximum controllability index using GA

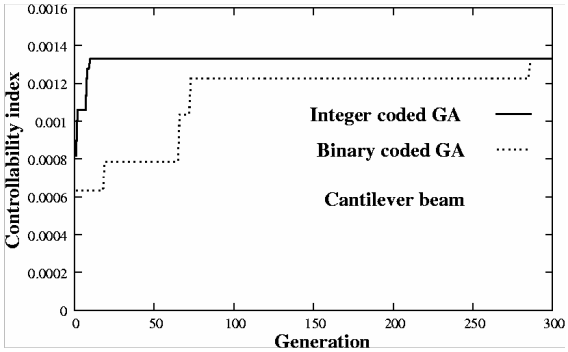

Fig. 5.7 Variation of controllability index with generation using integer and binary coded GA

Table 5.10. Several important parameters for integer and binary coded GA

	Integer coded	Binary coded
Number of genes to represent one actuator	1	8
Length of the chromosome	4	32
Population size	10	10
Crossover probability	0.9	0.9
Mutation probability	0.1	0.1

the root of the beam. This result is expected since the curvature of the first mode of vibration reaches its maximum value at the fixed end of the cantilever beam and a similar observation was also reported by Wang and Wang [97]. Fig.5.7 shows the convergence plot with generations for integer coded and binary coded GA for this problem and it could be observed that while the integer coded GA converges after 11 generations, binary coded GA converges only after 286 generations clearly showing the computational advantage of integer coded GA over binary coded GA for this problem as discussed in chapter 4. Hence, integer coded GA has been used for determination of optimal placement of sensors and actuators.

Table 5.11 Material properties of GR/E lamina and PZT [141]

Material properties	Gr/Epoxy lamina	PZT
E_1 (GPa)	172.5	63.0
$E_2 = E_3$ (GPa)	6.9	63.0
$G_{12} = G_{13}$ (GPa)	3.45	24.6
G_{23} (GPa)	1.38	24.6
$\upsilon_{12} = \upsilon_{13} = \upsilon_{23}$	0.25	0.28
ρ (kg m^{-3})	1600	7600
$e_{31} = e_{32}$ (C m^{-2})	0.0	10.62
$\in_{11} = \in_{22} = \in_{33}$ (F m^{-1})	0.0	0.1555 x 10^{-7}

5.1.5 Validation for optimal LQR gain

In order to ensure that GA based LQR methodology actually leads to the demonstration of optimal gain in active vibration control problems, the code developed based on the present formulation has been validated first. For this, a two degrees of freedom system shown in Fig. 5.8 is considered (example 6.4 given in Meirovitch [176]) to validate the code developed for LQR optimal control gain. The mass matrix [M] and stiffness matrix [K] are considered as

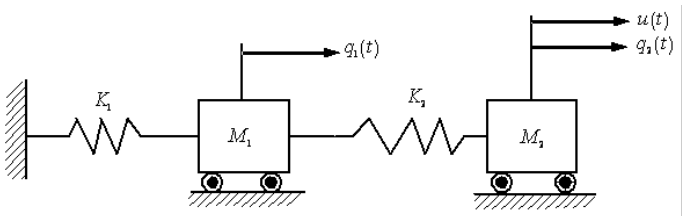

Fig. 5.8 Two degree of freedom system

$$[M]=\begin{bmatrix}1 & 0\\ 0 & 2\end{bmatrix},\ [K]=\begin{bmatrix}2 & -1\\ -1 & 1\end{bmatrix}$$

The system matrix A and control matrix B are given by

$$A=\begin{bmatrix} 0 & I \\ -M^{-1}K & 0 \end{bmatrix},\ B=\begin{bmatrix} 0 \\ M^{-1} \end{bmatrix}\begin{bmatrix} 0 \\ 1 \end{bmatrix}$$

The weighting matrices Q and R are given by

$$Q=\begin{bmatrix} K & 0 \\ 0 & M \end{bmatrix},\ R=[1]$$

The optimal control gain vector calculated from present code has been observed to have well agreed with that given in Meirovitch [176]. From Meirovitch [176] the control gain $G_c=[-1.0864 \quad 0.9092 \quad -0.5687 \quad 2.3742]^T$ and from the code the control gain is $G_c=[-1.08642 \quad 0.90923 \quad -0.56871 \quad 2.37422]^T$

5.2 Thermo-electro-mechanical analysis of smart FRP composite shell structures

After validation of the developed code, this has been used to analyze different simply supported smart FRP composite shell panels on a square base subjected to thermal load to study the pyroelectric effects on the thermally induced static displacement as well as on the developed sensor voltage of such shell panel. Stacking sequence of the GR/E laminated structure considered is [p/[0/90]$_s$/p]]. Here 'p' stands for distributed piezo-layers one for sensing and the other for actuation. The top piezoelectric layer has been taken as sensor and bottom piezoelectric layer has been considered as actuator. Thickness of each ply has been considered as 0.25 mm and that of piezo patch is 0.5 mm. A 10×10 finite element mesh has been considered to model the shell structures. The mechanical, electrical and coupled material properties [141] used in the present study have been listed in the Table 5.11. A spherical shell structures with two

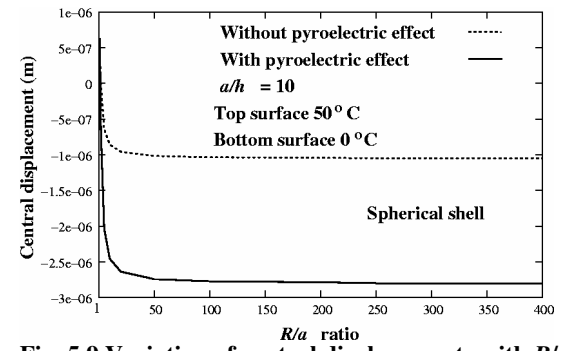

Fig. 5.9 Variation of central displacements with *R/a* ratios due to bottom surface 0°C and top surface 50°C for *a/h* =10

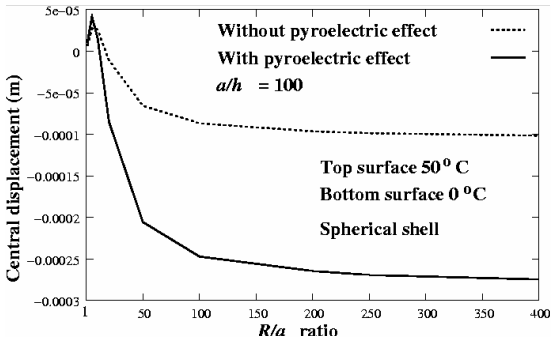

Fig. 5.10 Variation of central displacements with *R/a* ratios due to bottom surface 0°C and top surface 50°C for *a/h* =100

different thickness ratios (a/h = 10 and 100) and with various R/a ratios as well as different temperatures at the top and bottom surfaces have been studied.

5.2.1 Piezo-laminated spherical shell under thermal load

In this study, a simply supported piezo-laminated FRP composite spherical shell panel on a square base under the action of two different types of thermal load has been analyzed as follows

i) The thermal load applied on the top surface is taken as 50ºC and on the bottom surface is taken as 0 ºC.

ii) The thermal load applied on the top surface is taken as 0ºC and on the bottom surface is taken as 50 ºC.

Fig. 5.9 shows the comparison of central displacements neglecting and considering pyroelectric effect with R/a ratios due to bottom surface temperature 0ºC and top surface temperature 50ºC for a/h =10. It has been observed from Fig. 5.9 that the central displacements are more or less constant after R/a = 50 for both the cases (i.e. neglecting and considering pyroelectric effect). Fig. 5.10 shows the comparison of central displacements neglecting and considering pyroelectric effect with different R/a ratios due to bottom surface temperature 0ºC and top surface temperature 50ºC for a/h =100. It has been observed from Fig. 5.10 that pyroelectric effect exists for wide range of R/a ratios for thickness ratio a/h =100. It could also be noticed from Figs. 5.9 and 5.10 that the thermal loads together with pyroelectric effect lead to more static central displacement. The comparison of central displacements neglecting and considering pyroelectric effect with R/a ratios due to bottom surface temperature 50ºC and top surface temperature 0ºC for a/h =10 is shown in Fig. 5.11. The comparison of central displacements neglecting and considering pyroelectric effect with R/a ratios due to bottom surface temperature 50ºC and top surface temperature

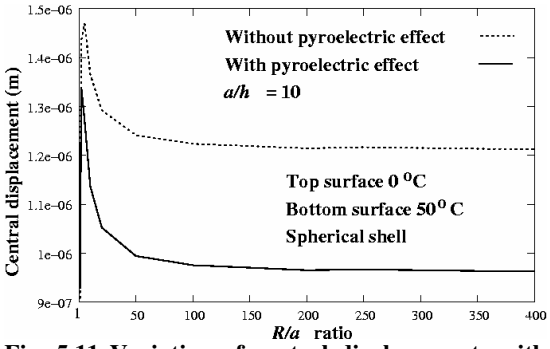

Fig. 5.11 Variation of central displacements with R/a ratios due to bottom surface 50ºC and top surface 0ºC for a/h =10

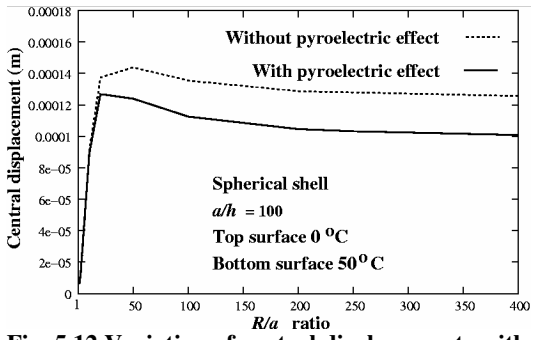

Fig. 5.12 Variation of central displacements with R/a ratios due to bottom surface 50ºC and top surface 0ºC for a/h =100

0ºC for a/h =100 is shown in Fig. 5.12. It has also been observed from Figs. 5.11 and 5.12 that the thermal loads together with pyroelectric effect lead to less static central displacement. It could be observed from Figs. 5.9 to 5.12 that pyroelectric based thermally induced displacement has also an effect on the top and bottom surfaces temperatures depending on the sensors or actuators. Therefore, pyroelectric effect is significant in the analysis of thermally induced static displacement of piezo-laminated structures especially for R/a>50. Figs. 5.13 and 5.14 show the comparison of variation of maximum sensor voltages with R/a ratios due to bottom surface temperature 0ºC and top surface temperature 50ºC for both thickness ratios without or with considering pyroelectric effect. Fig. 5.15 and 5.16 show the comparison of variation of maximum sensor voltages with R/a ratios due to bottom surface temperature 50ºC and top surface temperature 0ºC for both thickness ratios without or with considering pyroelectric effect. It could be observed from Figs. 5.13 to 5.16 that sensor voltages considering pyroelectric effect are more for both deep as well as shallow shells. From this analysis, it could be concluded that the central displacement as well as maximum sensor voltages depends on the electro-thermal coupling (i.e. pyroelectric effect), R/a ratios for different thickness ratios and

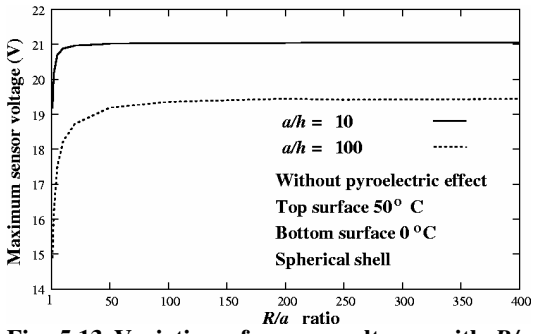

Fig. 5.13 Variation of sensor voltages with *R/a* ratios due to bottom surface 0ºC and top surface 50ºC

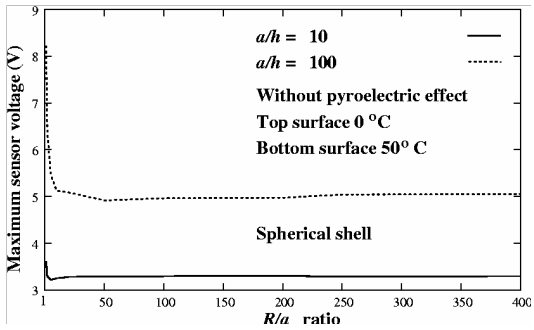

Fig. 5.14 Variation of sensor voltages with *R/a* ratios due to bottom surface 50ºC and top surface 0ºC

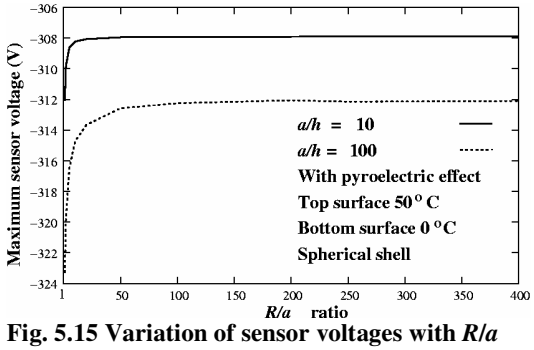

Fig. 5.15 Variation of sensor voltages with *R/a* ratios due to bottom surface 0ºC and top surface 50ºC considering pyroelectric

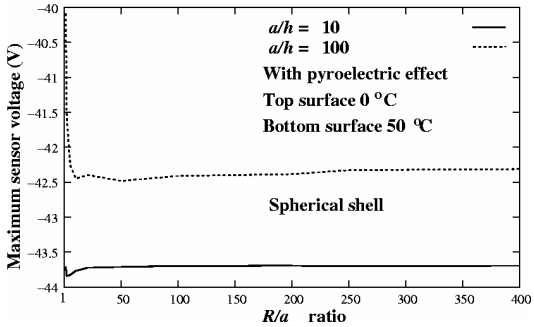

Fig. 5.16 Variation of sensor voltages with *R/a* ratios due to bottom surface 50ºC and top surface 0ºC considering pyroelectric

the top and bottom surfaces temperatures. Fig. 5.17 and Fig. 5.18 show the comparison of central displacements considering pyroelectric effect of deep spherical shell panels due to bottom surface temperature 0ºC and variable top surface temperatures for two different thickness ratios. It has been observed from Figs. 5.17 and 5.18 that the central displacements vary more rapidly for deep shell compared to shallow shell. The comparison of maximum sensor voltages considering pyroelectric effect of deep spherical shell panels due to bottom surface temperature 0ºC and variable top surface temperatures for two different thickness ratios are also shown in the Fig. 5.19 and Fig. 5.20. It has been observed from Figs. 5.19 and 5.20 that maximum sensor voltages are beyond the break down voltage of piezoelectric material considered due to top surface temperature 80ºC for both the thickness ratios.

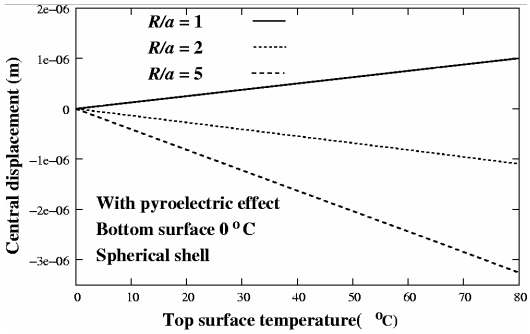

Fig. 5.17 Comparison of central displacements due to various top surface temperatures for a/*h* = 10

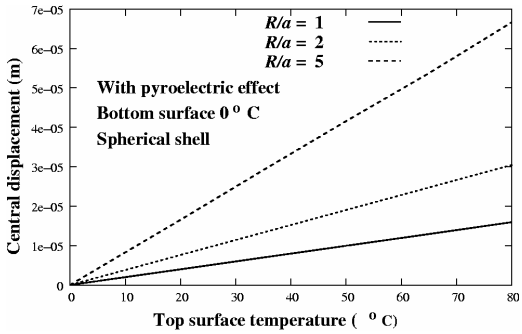

Fig. 5.18 Comparison of central displacements due to various top surface temperatures for a/*h* = 100

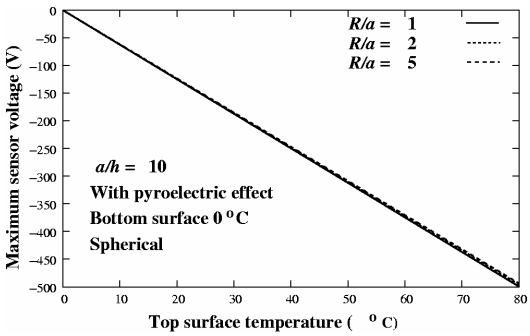

Fig. 5.19 Variation of sensor voltages due to various various top surface temperatures for *a/h* = 10

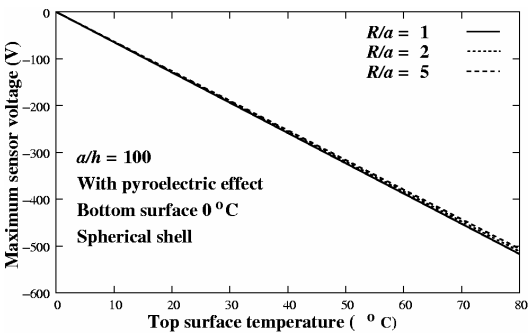

Fig. 5.20 Variation of sensor voltages due to various top surface temperatures for *a/h* = 100

5.2.2 Comparative study on thermo-electro-mechanical responses of different shells

Different types of smart FRP composite shells structures (such as spherical, ellipsoidal, doubly curved and cylindrical) have been analyzed in order to compare study the piezo-thermo-elastic responses of such shells structures under thermal loading without and with considering pyroelectric effect. For this study, the thermal load applied on the top

surface temperature is considered as 50ºC and on the bottom surface is considered as 0 ºC. Fig. 5.21 and Fig. 5.22 show the comparison of central displacements of different shell panels with *R*/*a* ratios for the thickness ratio *a*/*h* = 10 without and with considering pyroelectric effect respectively. Fig. 5.23 and Fig. 5.24 show the comparison of central displacements of different shell panels with *R*/*a* ratios for the thickness ratio *a*/*h* = 100 without and with considering pyroelectric effect respectively. It has been observed from Figs. 5.21 to 5.24 that thermally induced static displacements obtained are much more for all shell panels with considering pyroelectric effect compared to those without considering pyroelectric effect. It has also been observed that the magnitude of static displacement due to thermal gradient is more in the case of cylindrical shell panel and is least in the case of doubly curved shell panels. This is more significant in the case of thin shell panels and the difference is negligible for thick shell panels. The comparison of maximum sensor voltages of different shell panels with *R*/*a* ratios for the thickness ratio *a*/*h* = 10 without and with considering pyroelectric effect are shown in Fig. 5.25 and Fig. 5.26. The comparison of maximum sensor voltages of different shell panels with *R*/*a* ratios for the thickness ratio *a*/*h* = 100 without and with considering pyroelectric effect are shown in Fig. 5.27 and Fig. 5.28. It has been observed from Figs 5.25 to 5.28 that thermally induced sensors voltage is more in the case of considering pyroelectric effect than that of without considering pyroelectric effect for both the thickness ratios.

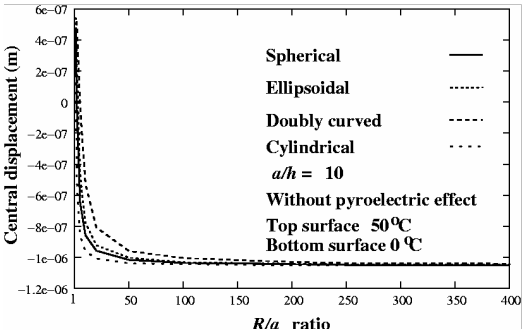

Fig. 5.21 Variation of central displacements of different shells with *R*/*a* ratios without pyroelectric effect for *a*/*h* =10

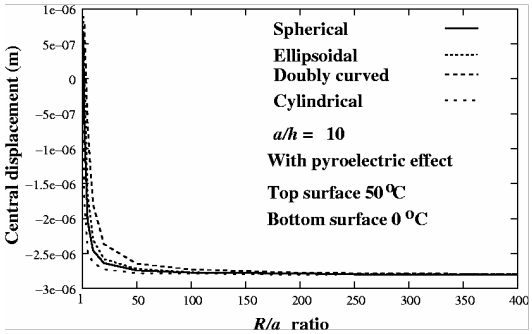

Fig. 5.22 Variation of central displacements of different shells with *R*/*a* ratios with pyroelectric effect for *a*/*h* =10

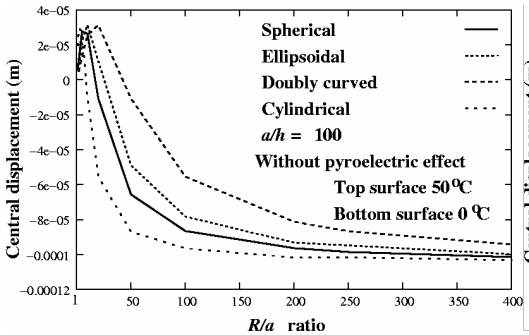

Fig. 5.23 Variation of central displacements of different shells with *R/a* ratios for *a/h* =100 neglecting pyroelectric effect

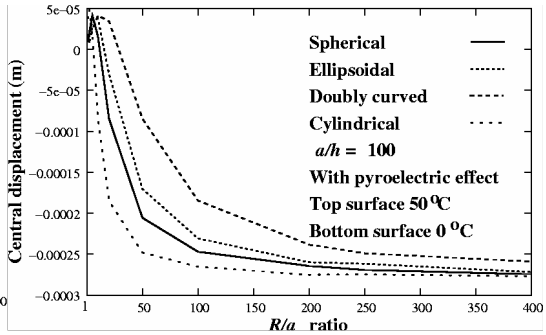

Fig. 5.24 Variation of central displacements of different shells with *R/a* ratios for *a/h* =100 considering pyroelectric effect

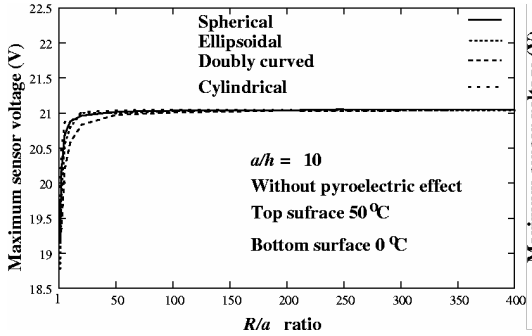

Fig. 5.25 Variation of sensor voltages of different shells with *R/a* ratios without pyroelectric effect for *a/h* =10

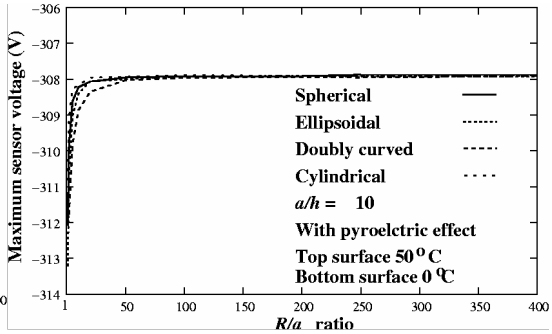

Fig. 5.26 Variation of sensor voltages of different shells with *R/a* ratios with pyroelectric effect for *a/h* =10

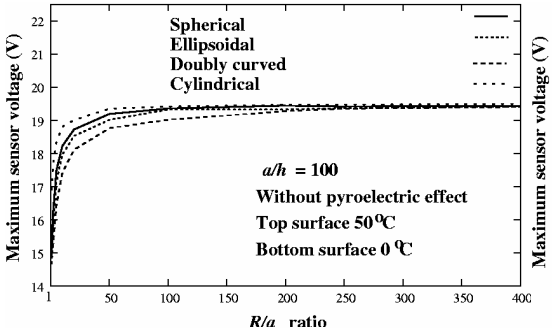

Fig. 5.27 Variation of sensor voltages of different shells with *R/a* ratios without pyroelectric effect *a/h* =100

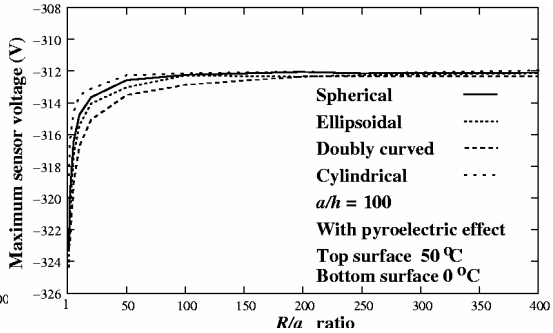

Fig. 5.28 Variation of sensor voltages of different shells with *R/a* ratios with pyroelectric effect for *a/h* =100

5.3 Summary

The entire computer codes starting from finite element analysis of smart shell structures subjected to thermo-electro-mechanical loading, determination of optimal actuators placement using GA and GA based LQR control scheme for active vibration control of shell structures have been validated with existing results available in literatures. Results obtained from the present developed code are in close agreement with the existing results. Four types of smart shell panels such as spherical, ellipsoidal, doubly curved and cylindrical panels have been analyzed to study the piezo-thermo-elastic responses of such

panels under various top and bottom surfaces temperatures for different thickness ratios without and with considering pyroelectric effects. It has been observed that pyroelectric effect is significant in both mechanical as well as electrical responses for piezolaminated shell panels under various thermal loading. It has also been observed that doubly curved shell panel is more rigid against thermally induced static displacement compared to other shell panels.

CHAPTER 6

Optimal Placement of Actuators using Genetic Algorithm

This chapter presents the results for optimal placement of collocated sensors and actuators in a smart FRP laminated composites. Based on the methodology developed (as discussed in chapter 4), integer coded GA based optimal placements of PZT actuators have been obtained for different types of smart shell structures and the superiority of the present method over existing methods has also been presented.

6.1 Problem definition

In this study, the stacking sequence of each laminated structure considered has been [p/[0/90]$_s$/p]]. Here 'p' stands for piezo-patches one for sensing and the other for actuation. In all the cases, thickness of each piezoelectric patch has been considered as 0.5 mm and thickness of each FRP composite ply has been considered as 0.25 mm. In all the cases, a 10×10 finite element mesh has been considered to model each shell panel and optimal actuators placement of such piezo-laminated structures have been calculated considering the first eight modes. First four modes out of eight modes have been considered as control modes and others have been considered as residual modes. Two types of piezo patch locations viz. Placement 1 and Placement 2 have been considered to study the influence of optimal placement on the input voltage of actuator and the closed loop-damping ratio for both considering and without considering control spillover. Placement 1 stands for optimal actuators placement based on the maximum controllability index neglecting control spillover. Placement 2 stands for optimal actuators placement based on the maximum controllability index considering control spillover of the higher order modes. In

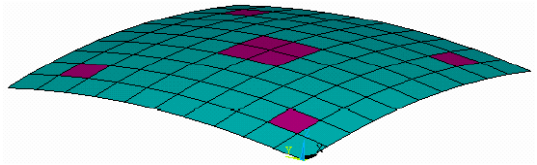

Fig. 6.1 Collocated sensors and actuators location on the spherical shell based on mode shape

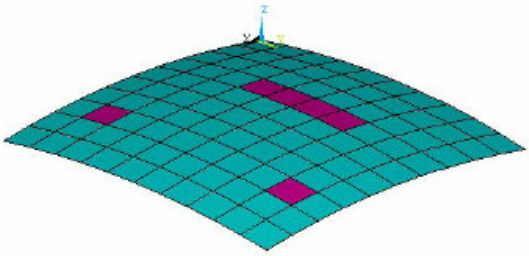

Fig. 6.2 Collocated sensors and actuators location on the spherical shell using Placement 1

this study, six sets of actuators have been considered. It has been assumed that the number of piezoelectric actuators to be less than the number of modes to be controlled [95]. The mechanical, electrical and coupled material properties [141] used in this study have been listed in the Table 5.11. Three different types of shell structures have been considered viz. spherical, ellipsoidal and cylindrical. In each case, *R/a* and *a/h* ratios have been considered as 3 and 10 respectively.

6.2 Optimal placement of collocated sensors and actuators on the spherical shell

A simply supported smart FRP composite spherical shell panel on a square base ($a = b$) has been considered. Actuators placements based on the mode shapes [139] considering eight actuators are shown in Fig. 6.1. Optimal collocated sensors and actuators placements based on the maximum controllability index using Placement 1 are shown in Fig. 6.2. Fig. 6.3 presents the evolution of the best fitness value i.e. controllability index using GA after 100 generations considering Placement 1. Optimal collocated sensors and actuators placements based on the maximum controllability index using Placement 2 are depicted in Fig. 6.4. Fig. 6.5 presents the evolution of the best fitness value i.e. controllability index using GA after 100 generations using Placement 2. From Table 6.1, it could be observed that the placements of actuators using both the optimal placement schemes (i.e. Placement 1 and Placement 2) have achieved better controllability indices than that corresponding to the mode shaped

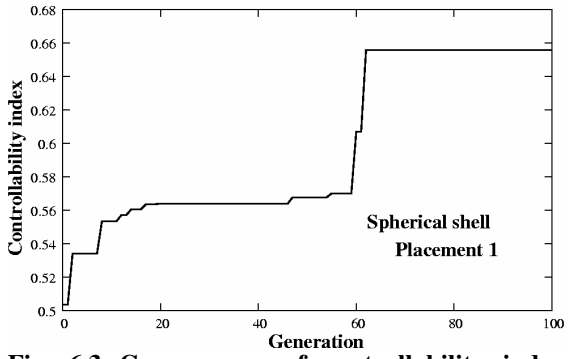

Fig. 6.3 Convergence of controllability index with generation for spherical shell using Placement 1

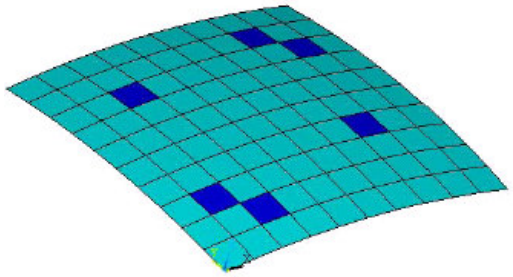

Fig. 6.4 Collocated sensors and actuators location on the spherical shell using Placement 2

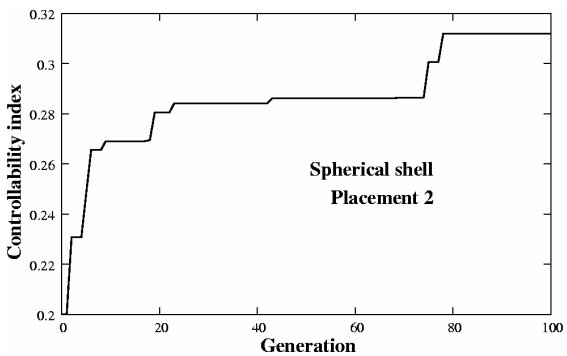

Fig. 6.5 Convergence of controllability index with generation for spherical shell using Placement 2

based placements even though increased number of actuators has been used in the later case. It has also been observed from Table 6.1 that the conventional mode shaped based placement gives very less controllability index considering control spillover than that of Placement 2. First eight natural frequencies corresponding to mode shape based, Placement 1 and Placement 2 collocated sensors and actuators placement considered in the present work have been shown in the Table 6.2. It has been observed from Table 6.2 that placement of actuators has a little effect on the system eigenvalues.

Table 6.1 Value of maximum controllability index for different placement schemes

Mode shape based		Placement 1 (i.e. neglecting control spillover)	Placement 2 (i.e. considering control spillover)
Neglecting control spillover	Considering control spillover		
0.540108.	0.05660	0.65563	0.31203

Table 6.2 First eight natural frequencies of the different pizolaminated spherical panels

Natural frequencies (kHz)	Spherical panel with different of collocated sensors/actuators placements		
	Mode shapes based	Placement1	Placement2
1^{ist}	11.282	11.729	13.110
2nd	21.277	21.353	21.278
3rd	30.620	30.672	30.468
4th	32.027	31.242	33.129
5th	33.699	32.294	33.439
6th	36.436	35.500	36.135
7th	39.524	41.910	39.823
8th	48.177	52.605	48.315

6.3 Optimal placement of collocated sensors and actuators on the ellipsoidal shell

In this study, a simply supported smart FRP composite ellipsoidal shell panel on a square base ($a = b$) has been analyzed to study the optimal placement of actuators and vibration control. The major axis length is $2\times R$ and minor axis length is $1.5\times R$. Optimal collocated sensors and actuators placements on the ellipsoidal shell panel based on the maximum controllability index neglecting control spillover are shown in Fig. 6.6. Figure 6.7 presents the evolution of the best fitness value i.e. controllability index using GA after 100 generations considering Placement 1. Optimal collocated sensors and actuators placements on the shell panel based on the maximum controllability index considering control spillover are depicted in Fig. 6.8. Figure 6.9 presents the evolution of the best fitness value i.e. controllability index

using GA after 100 generations using Placement 2 considering first four modes as control modes. First eight natural frequencies corresponding to Placement 1 and Placement 2 considered in this study have been shown in the Table 6.2. It could be cleared from Table 6.3 that some of the natural frequencies have significantly increased in case of Placement 2 than that of Placement 1.

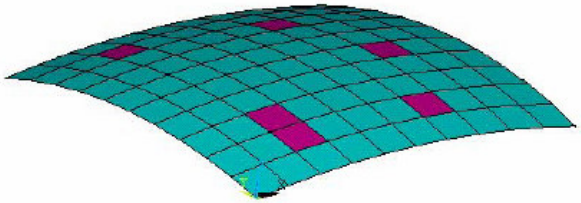

Fig. 6.6 Collocated sensors and actuators location on the ellipsoidal shell using Placement 1

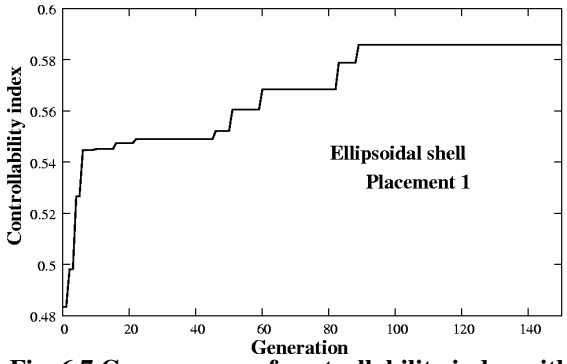

Fig. 6.7 Convergence of controllability index with generation for ellipsoidal shell using Placement 1

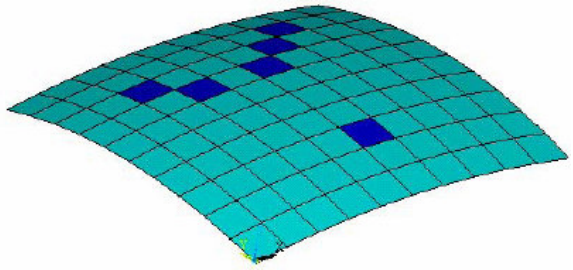

Fig. 6.8 Collocated sensors and actuators location on the ellipsoidal shell using Placement 2

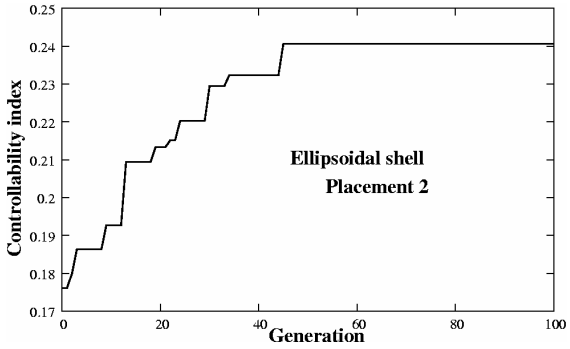

Fig. 6.9 Convergence of controllability index with generation for ellipsoidal shell using Placement 2

Table 6.3 First eight natural frequencies of the different pizolaminated ellipsoidal panel models

Natural frequencies (kHz)	Ellipsoidal panel with	
	Placement1	Placement2
1^{ist}	13.653	12.798
2nd	20.734	20.570
3rd	30.692	31.066
4th	32.173	31.516
5th	33.870	32.817
6th	34.114	38.054
7th	37.430	38.833
8th	45.263	50.664

6.4 Optimal placement of collocated sensors and actuators on the doubly curved shell

A simply supported smart FRP composite double curved shell panel on a square base ($a = b$) has been analyzed to study the optimal placement of actuators and vibration control. The radii of this panel are taken as $R_1 = 2 \times R_2$. Optimal collocated sensors and actuators placements on the doubly curved shell panel based on the maximum controllability index neglecting control spillover are shown in Fig. 6.10. Figure 6.11 presents the evolution of the best fitness value i.e. controllability index using GA after 100 generations considering Placement 1. Optimal collocated sensors and actuators placements on the doubly curved shell panel based on the maximum controllability index considering control spillover are depicted in Fig. 6.12. Figure 6.13 presents the evolution of the best fitness value i.e. controllability index using GA after 100 generations using Placement 2 considering first four modes as control modes. First eight natural frequencies of the doubly curved shell panel corresponding to Placement 1 and

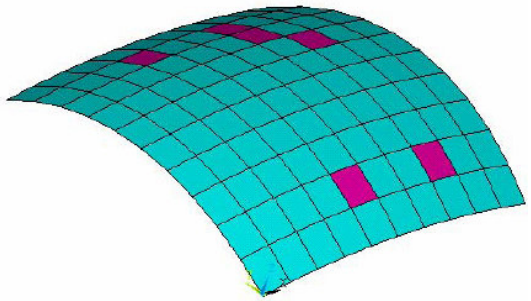

Fig. 6.10 Collocated sensors and actuators location on the doubly curved shell using Placement 1

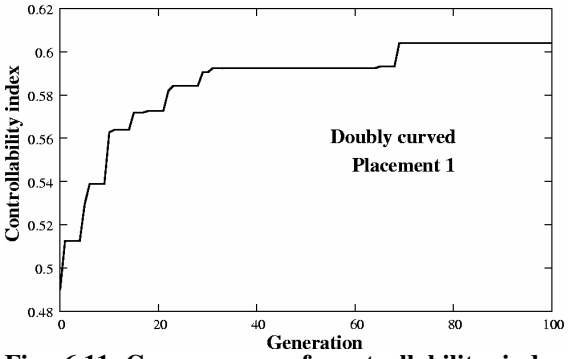

Fig. 6.11 Convergence of controllability index with generation for doubly curved shell using Placement 1

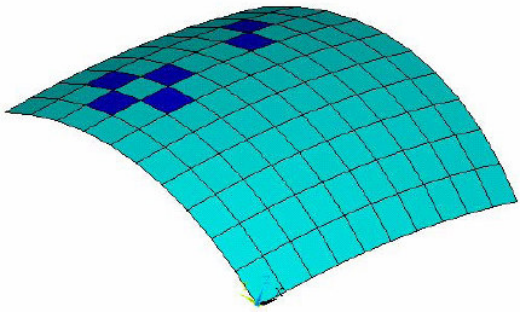

Fig. 6.12 Collocated sensors and actuators location on the doubly curved shell using Placement 2

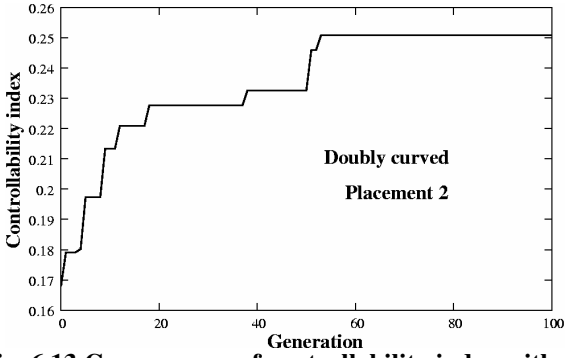

Fig. 6.13 Convergence of controllability index with for doubly curved shell using Placement 2

Placement 2 considered in this present study have been shown in the Table 6.4.

Table 6.4. First eight natural frequencies of the different pizolaminated doubly curved models

Natural frequencies (kHz)	Doubly curved panel with	
	Placement1	Placement2
1^{ist}	17.178	17.205
2nd	19.594	21.564
3rd	30.462	30.771
4th	31.612	31.360
5th	33.460	32.697
6th	34.690	36.378
7th	37.617	39.876
8th	45.095	46.373

6.5 Optimal placement of collocated sensors and actuators on the cylindrical shell

In this analysis a simply supported smart FRP composite cylindrical panel has been considered. Dimensions of this panel are $a = b$, $a/h = 10$, $R_2/a = 3$, $R_1 = \infty$. Optimal collocated sensors and actuators placements on the cylindrical panel based on the maximum controllability index neglecting control spillover are shown in Fig. 6.14. Figure 6.15 presents the evolution of the best fitness value i.e. controllability index using GA after 100 generations considering Placement 1. Optimal collocated sensors and actuators placements on the cylindrical based on the maximum controllability index considering control spillover are depicted in Fig. 6.16. Figure 6.17 presents the evolution of the best fitness value i.e. controllability index using GA after 100 generations using Placement 2 considering first four modes as control modes. First eight natural frequencies

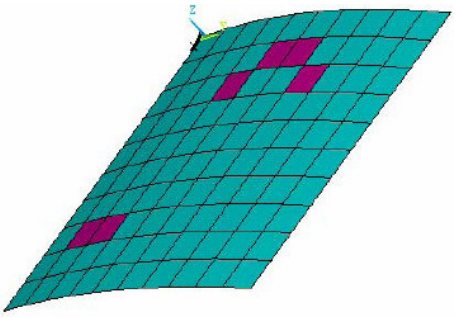

Fig. 6.14 Collocated sensors and actuators location on the cylindrical shell using Placement 1

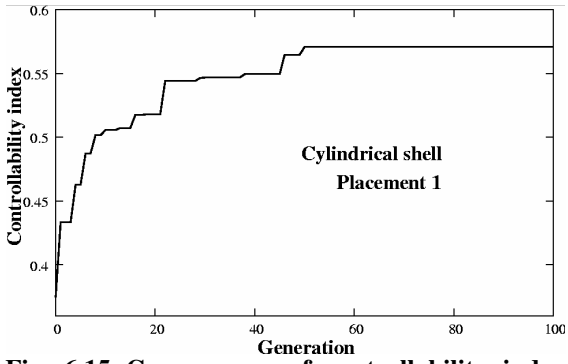

Fig. 6.15 Convergence of controllability index with generation for cylindrical shell using Placement 1

of cylindrical shell panel corresponding to Placement 1 and Placement 2 considered in this study have been shown in the Table 6.5.

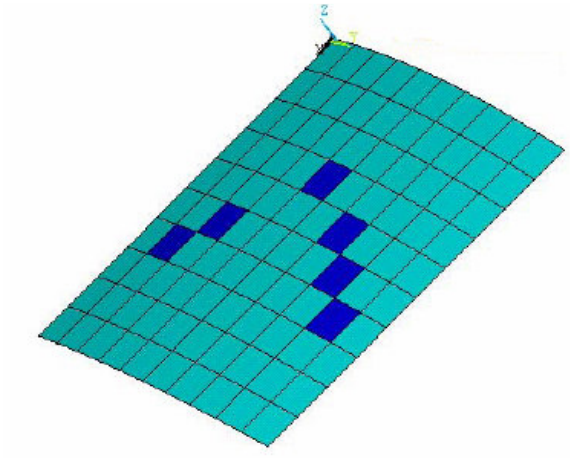

Fig. 6.16 Collocated sensors and actuators location on the cylindrical shell using Placement 2

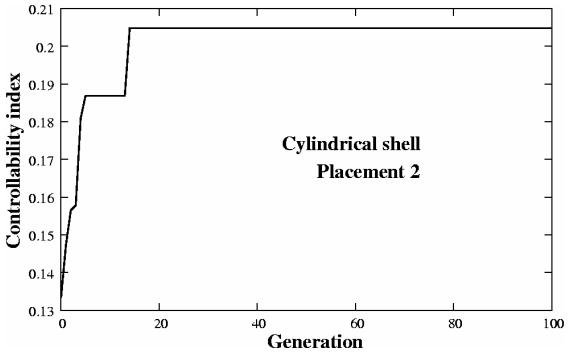

Fig. 6.17 Convergence of controllability index with for cylindrical shell using Placement 2

Table 6.5 First eight natural frequencies of the different pizolaminated cylindrical models

Natural frequencies (kHz)	Cylindrical panel with Placement1	Placement2
1^{ist}	11.074	10.358
2nd	20.458	19.338
3rd	29.782	30.121
4th	31.598	32.689
5th	33.898	34.238
6th	35.714	38.544
7th	41.159	38.970
8th	51.902	51.175

6.6 Summary

Integer coded GA with uniform crossover and an improved mutation technique have been used for determination of optimal actuator placement by maximizing the controllability index. Integer coded GA has been observed to give superior performance in term of computational time and storage compared to binary coded GA. The proposed method has been observed to search for optimal placement of actuators, which results in better controllability, compared to conventional mode shape based placement. Effect of control spillover has also been considered. Several composite shell panels have been analyzed for optimal placement of actuators in such structures using proposed GA based optimal placement scheme.

CHAPTER 7

Genetic Algorithm (GA) based Optimal Vibration Control of Smart FRP Composite Shell structures

In this chapter GA based LQR optimal control scheme (described in chapter 4) has been used for optimal vibration control of different types of smart shell structures. The superiority of the present scheme to the conventionally used LQR schemes has been demonstrated. Efficacy of different sensors and actuators placement schemes has also been presented in terms of their control performances of the smart shell structures.

7.1 Problem definition

Four different types of smart shell structures have been considered in this study are

i) a smart spherical shell panel

ii) a smart ellipsoidal shell panel

iii) a smart doubly curved shell panel and

iv) a smart cylindrical shell panel

All these shell panels have been considered on a square base ($a = b$) as shown in Fig.7.1. In each case, R/a and a/h ratios have been considered as 3 and 10 respectively. In this study, the stacking sequence of each laminated structure has been considered Graphite/Epoxy $[p/[0/90]_s/p]$. Here 'p' stands for piezo-patches, one for sensing and the other for actuation. In all the cases, thickness of each piezoelectric patch has been considered as 0.5 mm and thickness of each FRP composite ply has been considered as 0.25 mm. The mechanical, thermal, electrical and coupled material properties used in the present study have been listed in the Table 7.1. Finite element (FE) analyses have been done using the shell element described in chapter 3. A 10 × 10 FE mesh been used with total degrees of freedom = 1705, number of elements = 100 and number of nodes = 341. In this study, based on the optimal placement of actuators (using GA as presented in chapter 6), GA-LQR control scheme has been applied for the control of such shell structures subjected to an applied impulse load as well as thermal gradient. In all the cases, the smart panel has been subjected to an impulse load of 10 N at

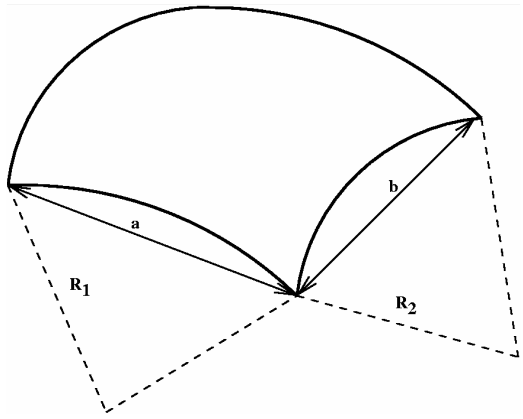

Fig. 7.1 A shell panel

the center for a duration of $\tau/25$ seconds (where τ is the time period corresponding to first natural frequency of the system) and impulse responses of this panel have been calculated with a time step of $\tau/100$ seconds in order to accurately integrate the response in those modes for which time step is larger [177]. For all the cases, a modal damping ratio (ξ_d) of 1% has been assumed to obtain open loop response and to calculate LQR gains [141]. In case of thermal loading, in all the cases temperature on the top surface has been taken as 50ºC and on the bottom surface is taken as 0 ºC. In all the cases, dynamic responses of the piezo-laminated structures have been calculated using mode superposition technique, considering the first eight modes. The allowable voltage of piezo-ceramic materials has been taken as 1000 V/mm thickness of the piezo-patch [171].

Table 7.1 Coupled material properties for Gr/Epoxy lamina and PZT

Material properties	Gr/Epoxy lamina	PZT
E_1 (GPa)	172.5	63.0
$E_2 = E_3$ (GPa)	6.9	63.0
$G_{12} = G_{13}$ (GPa)	3.45	24.6
G_{23} (GPa)	1.38	24.6
$\upsilon_{12} = \upsilon_{13} = \upsilon_{23}$	0.25	0.28
ρ (kg m^{-3})	1600	7600
$e_{31} = e_{32}$ (C m^{-2})	0.0	10.62
$\in_{11} = \in_{22} = \in_{33}$ (F m^{-1})	0.0	0.1555 x 10^{-7}
α_1 (/ºC)	0.024×10^{-6}	1.2×10^{-6}
α_2 (/ºC)	24×10^{-6}	1.2×10^{-6}
P_3 (cK^{-1}m^{-2})	----	-2.5×10^{-4}

7.2 Optimal vibration control of laminated spherical shell panel

A simply supported smart FRP composite spherical shell panel under the action of impulse load at the center as well as combined impulse and thermal load has been analyzed to study the vibration control based on different actuators placement schemes using LQR as well as the proposed GA-LQR control schemes. Dimensions of this panel are $a = b = 20 \times 10^{-3}$ m, $R_1 = R_2 = R = 60 \times 10^{-3}$ m, $h = 2$ mm. Three different types of actuators placement has been considered as shown in Table 7.3 to study efficacy of different actuators placement schemes on the control performance.

7.2.1 Optimal vibration control under impulse load

The smart spherical panel has been subjected to an impulse load of 10 N at the center for a duration of 3.0510892 μs and impulse responses of the panel have been calculated with a time step of 0.7627723 μs (since τ = 76.27723 μs for spherical panel). Figure 7.2 shows the uncontrolled displacement history of this smart spherical panel under

impulse loading. The LQR controlled displacement histories of smart spherical panel using mode shape based placement, Placement 1 and Placement 2 have been depicted in Fig. 7.3.

Table 7.2. Different actuator placement schemes used

Mode shape based	Placement 1	Placement 2
Based on the mode shape considering first eight modes and eight actuators.	Maximizing the modal control forces of the first eight modes using six actuators.	Considering control spillover of the higher modes i.e. maximizing the modal control forces of the first four modes only and minimizing the modal control forces of the last four modes in first eight modes using six actuators.

It could be observed that in the simple LQR controlled response of the panel with mode shape based placement, Placement 1 and Placement 2, the closed loop damping ratios achieved have been 1.26%, 1.72% and 1.94% respectively. The maximum actuator voltage variations using mode shape based placement, Placement 1 and Placement 2 for simple LQR control scheme have also been shown in Fig. 7.4. It could be observed from Fig. 7.4, that the magnitude of maximum actuator voltage is much less in the case of Placement 2 compared to those in mode shape based placement and Placement 1 for simple LQR control scheme even though the corresponding closed loop damping ratios is marginally better, showing that the same damping ratio could be obtained with a much less actuator voltage corresponding to Placement 2. This is due to the fact that the electromechanical coupling matrix in the case of optimal placement using Placement 2 leads to better actuation. Fig. 7.5 shows the GA-LQR controlled displacement histories using mode shape based placement, Placement 1 and

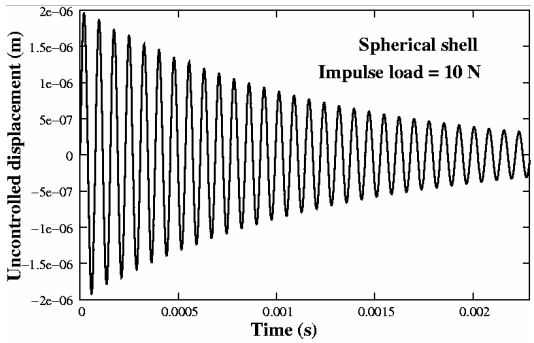

Fig. 7.2 Uncontrolled displacement history of the smart spherical panel due to impulse loading

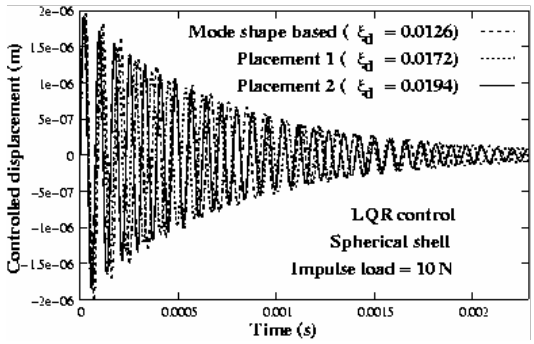

Fig. 7.3 LQR controlled displacement history of the smart spherical panel based on different placement schemes

Placement 2. In this case, the closed loop damping ratios achieved for mode shape based placement, Placement 1 and Placement 2 are 2.93 %, 3.49 % and 12.1 % respectively. The maximum actuator voltage variations using mode shape based placement, Placement1 and Placement2 for GA-LQR control scheme is also shown in Fig. 7.6. It could be clearly observed from Fig. 7.6 that the maximum actuator voltage is much more in the case of mode shape based placement compared to those in the case of Placement 1 and Placement 2 for GA-LQR search control scheme and is least in the case of Placement 2. From Figs 7.5 and 7.6, it could be concluded that the GA-LQR scheme with Placement 2 gives maximum closed loop damping ratio with minimum input actuation voltage. This shows that GA-LQR control schemes not only leads to superior optimal gain compared to conventional LQR, but also leads to minimization of actuation voltage in achieving more effective closed loop damping. Fig. 7.7 shows the convergence of calculated fitness i.e. closed loop damping ratio with number of generations using mode shape based placement, Placement1 and Placement2 for GA-LQR search control scheme. It could be observed that the closed loop-damping ratio is not only much higher in the case of Placement 2 compared to those in case of mode shape based placement and Placement1, but the convergence has also been achieved much faster. Fig. 7.8 shows the LQR and GA-LQR controlled displacement histories using Placement 2.

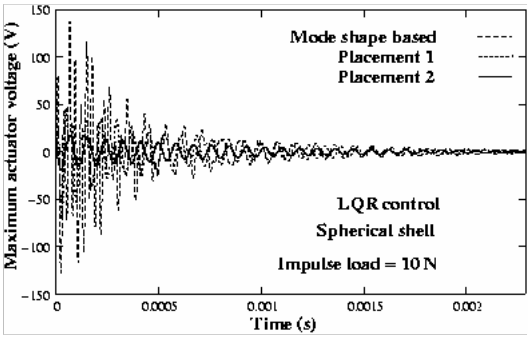

Fig. 7.4 Maximum actuator voltage variation for LQR control of spherical panel under impulse load

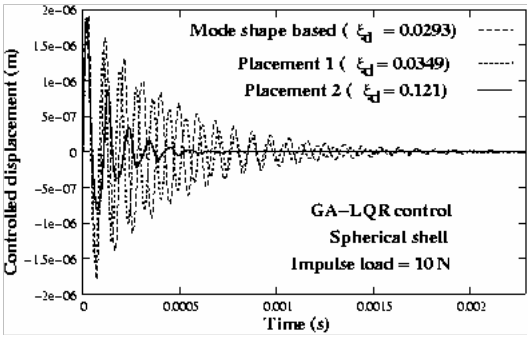

Fig. 7.5 GA-LQR controlled displacement history of spherical panel under impulse load

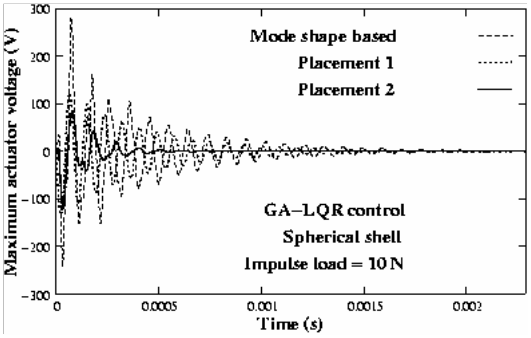

Fig. 7.6 Maximum actuator voltage variation for GA-LQR control of spherical panel under impulse load

It has been observed from the Fig. 7.8 that the closed loop-damping ratio is much more in the case of GA-LQR search control scheme with Placement 2 than that in case of simple LQR control scheme. The maximum actuator voltage variations using Placement2 for LQR and GA-LQR control scheme is also shown in Fig. 7.9. From these results it could be concluded that optimal actuator placement using Placement 2 and subsequent GA-LQR control scheme lead to the maximization of closed loop damping ratio with minimum input/actuator voltage within the limit. Optimal vibration control of this panel with Placement2 under thermo-mechanical loading using GA-LQR control scheme has also been discussed in the following subsection.

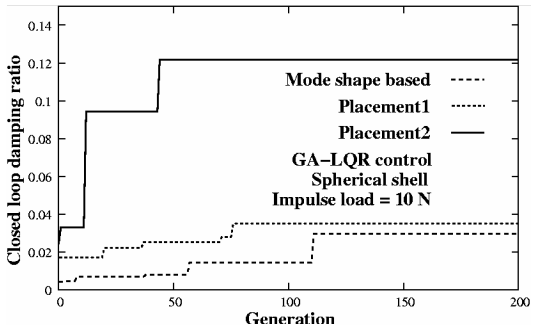

Fig. 7.7 Variation of closed loop damping ratio with generation for spherical panel using GA-LQR control

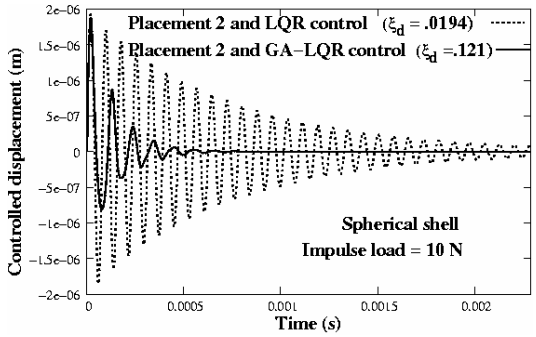

Fig. 7.8 LQR and GA-LQR controlled displacement of spherical panel under impulse load

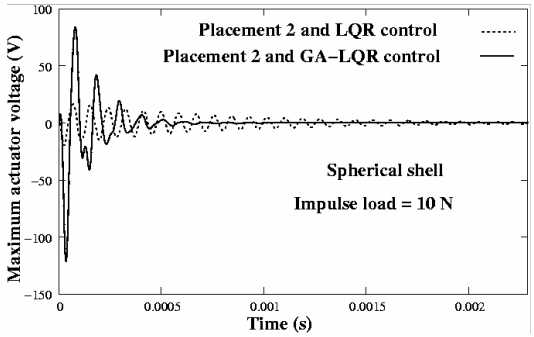

Fig. 7.9 Actuator voltage variation for LQR and GA-LQR control schemes of spherical panel under impulse load

7.2.2 Optimal vibration control under combined impulse and thermal load

Here, the same smart spherical shell has been subjected to both impulse load as well as thermal gradient. GA-LQR scheme has been applied to control both the displacements i.e. impulse induced as well as thermally induced static displacement using Placement 2. The uncontrolled thermo-mechanical displacement histories of the smart FRP composite spherical panel with and without considering pyroelectric effect are shown in Fig 7.10 and Fig.7.11

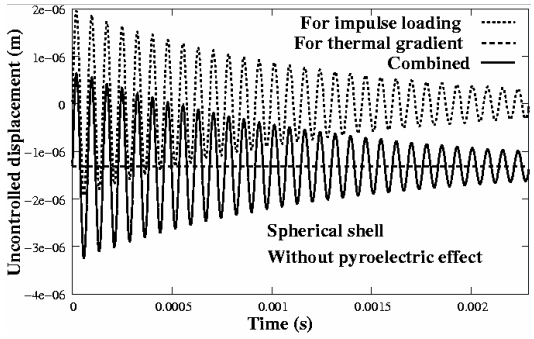

Fig.7.10 Uncontrolled thermo-mechanical displacement of spherical without pyroelectric effect

respectively. From these figures, it could be observed that the combined thermo-mechanical displacement is more in the case when pyroelectric effect is considered due to electro-thermal load. Fig. 7.12 shows the GA-LQR controlled displacement histories under thermo-mechanical loading considering pyroelectric effect and without considering pyroelectric effect. In this case, the closed loop damping ratios for without pyroelectric and with pyroelectric effect are 3.68 % and 3.42 % respectively. It has already been reported by Jiang and Li [86] that the thermally induced static offset is beyond control by negative feedback controller. Narayanan and Balamurugan [146] studied the active vibration control performance of a simply supported piezo-laminated aluminum plate under thermal gradient using conventional LQR control scheme and reported that the thermally induced offset was beyond control using the LQR scheme. Fig. 7.12 clearly shows that the present GA-LQR control scheme and the proposed sensor output is able to control both the displacements (i.e. undesired impulse induced displacement as well as thermally induced static displacement due to thermal gradient) within the limit of actuator voltage. It could also be observed from Fig. 7.12 that incorporation of pyroelectric effect could lead to control of combined thermo-mechanical displacement where as without pyroelectric effect, complete control could not be achieved. The maximum actuator voltage variations for GA-LQR control scheme with and without considering

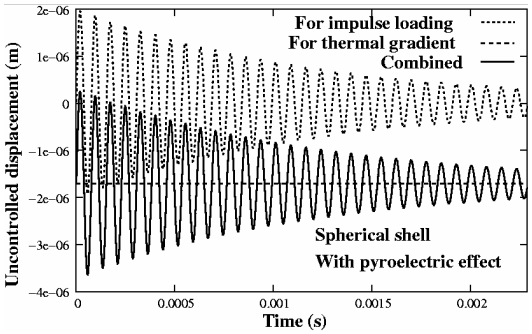

Fig. 7.11 Uncontrolled thermo-mechanical displacement history of spherical panel with pyroelectric effect

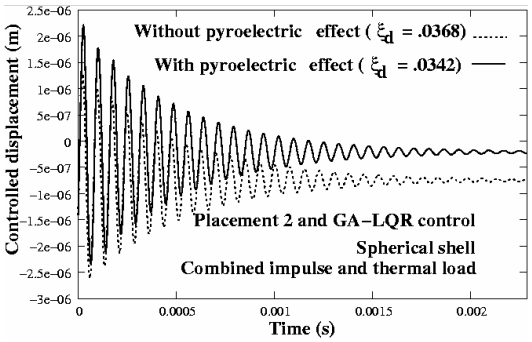

Fig. 7.12 Controlled displacement of spherical panel under thermo-mechanical loading

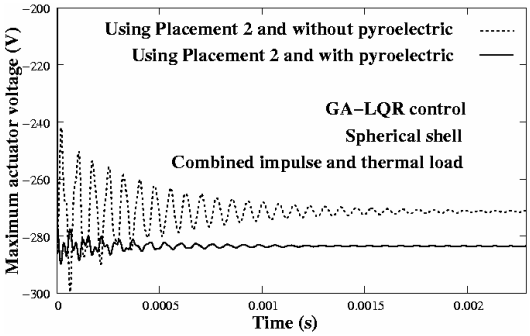

Fig. 7.13 Actuator voltage variation for spherical panel under thermo-mechanical loading

pyroelectric effect is shown in Fig. 7.13. It could be clearly noticed from Fig. 7.13 that there is actuator voltage offset in both the cases. These are due to thermally induced sensor voltage. This also shows that if the controller gain is designed without considering pyroelectric effect, the actuator voltages could be overestimated for control of thermally induced static offset. Therefore, for more accurate calculation of actuator voltage, pyroelectric effect should be considered in the analysis. From Fig 7.13, it could be observed that even though the voltage requirement is slightly higher in the case of considering pyroelectric effect, this voltage leads to complete control of combined thermo-mechanical displacement which was not possible in the case of without considering pyroelectric effect. It should also be noted that in the case of considering pyroelectric effect, a part of the total voltage requirement of the actuator is actually generated by the sensor due to pyroelectric effect. Fig. 7.14 shows the convergence of calculated fitness i.e. closed loop damping ratio with number of generations without and with considering pyroelectric effect for GA-LQR search control scheme. It could be observed that the damping ratio achieved is more in the case of without pyroelectric effect. However, better control of combined thermo-mechanical displacement has been achieved by considering pyroelectric effect which is clear from Fig. 7.12. Fig. 7.15 shows the LQR and GA-LQR controlled displacement histories under thermo-mechanical loading. It has been observed from the Fig. 7.15 that the displacement control achieved is much more in the case of GA-LQR search control scheme than that in case of conventional LQR control scheme. The maximum actuator voltage variation for LQR and GA-LQR control schemes under

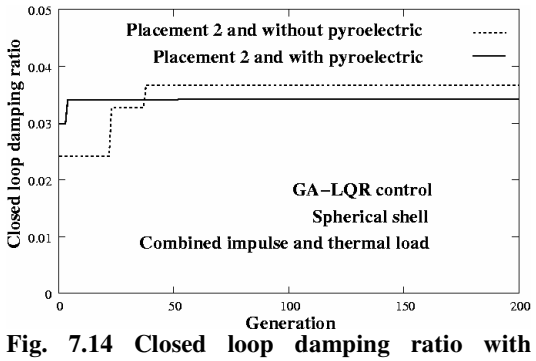

Fig. 7.14 Closed loop damping ratio with generation for spherical shell

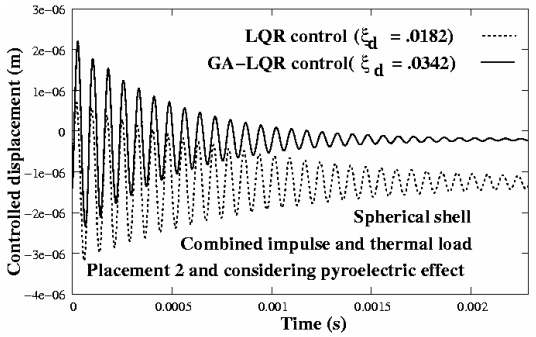

Fig. 7.15 Controlled displacement of spherical shell under thermo-mechanical loading

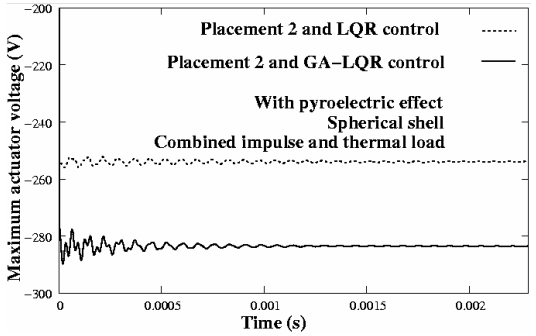

Fig. 7.16 Maximum actuator voltage variation of different control schemes for spherical shell

thermo-mechanical loading is shown in Fig. 7.16. It could be noticed that even though the voltage requirement of the actuator in the case of GA-LQR control scheme is higher than that in case of simple LQR control scheme, simple LQR could not achieved complete control in the case of thermo-mechanical loading. On contrary, complete control of combined thermo-mechanical displacement is possible with the proposed GA-LQR control scheme.

7.3 Optimal vibration control of laminated ellipsoidal shell panel

In this study, a simply supported smart FRP composite ellipsoidal shell panel on a square base ($a = b = 20 \times 10^{-3}$ m) under the action of impulse load at the center as well as thermal load has been analyzed to study optimal vibration control. The major axis length considered is $2\times R$ and minor axis length considered is $1.5\times R$. The radius (i.e. R) of this panel has been considered to be 30×10^{-3} m. This smart ellipsoidal panel has been subjected to an impulse load of 10 N at the center for a duration of 3.16530 μs. Impulse responses of the panel have been calculated with a time step of 0.7913271 μs. Fig. 7.17 shows the comparison of uncontrolled and GA-LQR controlled displacement histories of this panel for impulse loading. In this case,the closed loop damping ratio achieved using GA-LQR control scheme is 9.67 %. The maximum actuator voltage variation of this smart panel using GA-LQR control scheme for impulse loading is shown in Fig. 7.18. Fig.7 19 shows the convergence of calculated fitness i.e. closed loop damping ratio with number of generations for this smart ellipsoidal panel using GA-LQR control scheme for impulse loading. The uncontrolled thermo-mechanical displacement histories with and without considering pyroelectric effect is depicted in Fig 7.20. Fig. 7.21 shows the GA-LQR controlled displacement histories under thermo-mechanical loading without and with considering pyroelectric effect. In this case, the closed loop damping ratios achieved without and with considering pyroelectric effect are 3.58 %

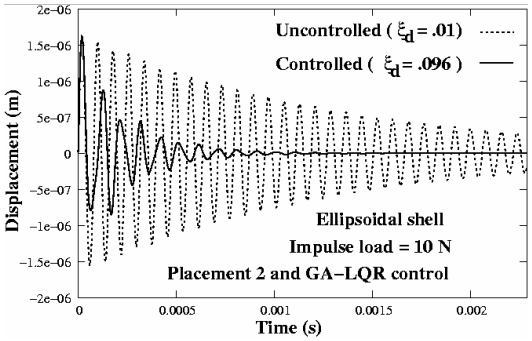

Fig. 7.17 Uncontrolled and controlled displacement of ellipsoidal panel under impulse loading

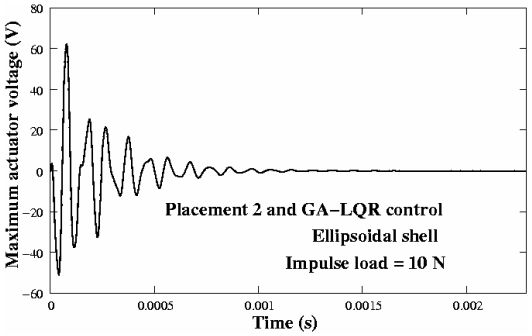

Fig. 7.18 Maximum actuator voltage variation of ellipsoidal panel under impulse loading

and 3.67 % respectively. The maximum actuator voltage variations for GA-LQR control scheme without and with considering pyroelectric effect is shown in Fig. 7.22. From Fig 7.22, it could be observed that even though the voltage requirement is higher in the case of considering pyroelectric effect, this voltage leads to better control of combined thermo-mechanical displacement than that of without considering pyroelectric effect. Fig. 7.23 shows the convergence of calculated fitness i.e. closed loop damping ratio with number of generation without and with considering pyroelectric effect for GA-LQR search control scheme. From these results, it could be inferred that the proposed GA-LQR scheme in conjunction with the proposed GA based placement scheme could achieved control of ellipsoidal smart shells under mechanical as well as thermo-mechanical loading with minimum actuator voltage.

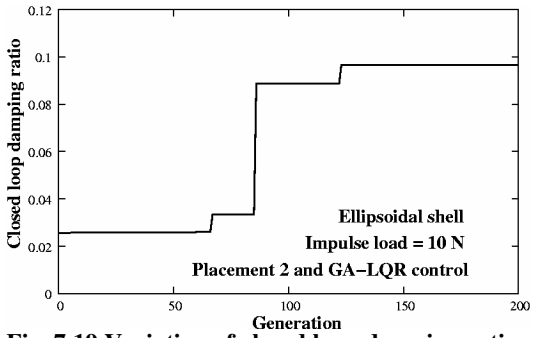

Fig. 7.19 Variation of closed loop damping ratio with generation of ellipsoidal panel for impulse loading

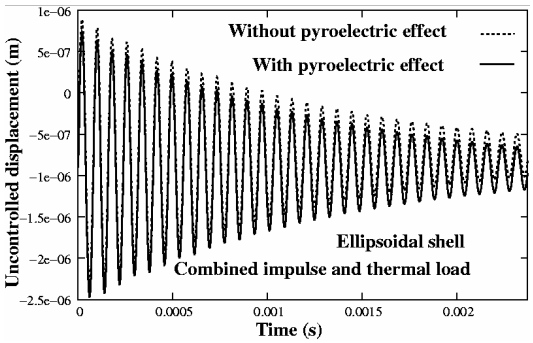

Fig. 7.20 Uncontrolled thermo-mechanical displacement history of ellipsoidal panel

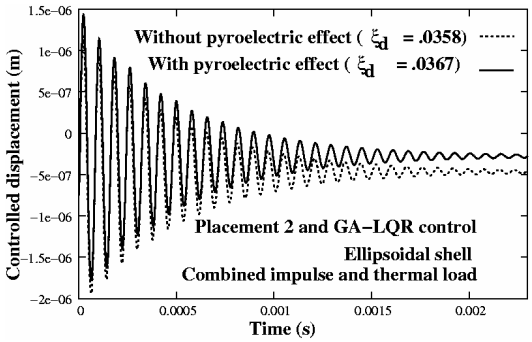

Fig. 7.21 Controlled displacement of ellipsoidal panel under thermo-mechanical loading

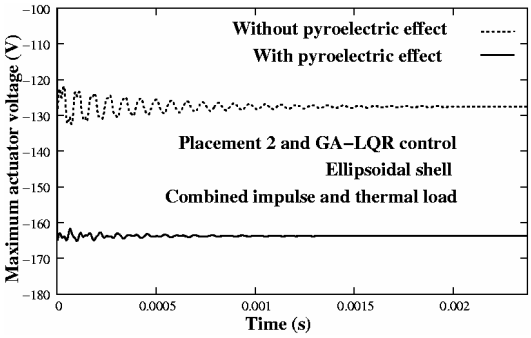

Fig. 7.22 Maximum actuator voltage variation for GA-LQR control scheme of ellipsoidal shell panel

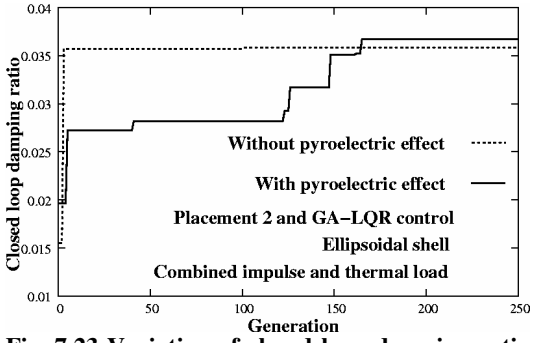

Fig. 7.23 Variation of closed loop damping ratio with generation of ellipsoidal panel due to thermo-mechanical loading

7.4 Optimal vibration control of laminated doubly curved shell panel

A simply supported smart FRP composite double curved shell panel on a square base under the action of impulse load at the center as well as thermal load has been analyzed to study optimal vibration control. The radii of this panel are taken as $R_1 = 2\times R_2$. Dimensions of this panel are $a = b = 20 \times 10^{-3}$ m, $R_1 = 2\times R_2 = 60 \times 10^{-3}$ m, $h = 2$ mm. This smart panel has been subjected to an impulse load of 10 N at the center for a duration of 2.253904 μs and impulse responses of the panel have been calculated with a time step of 0.563476 μs. Fig. 7.24 shows the comparison of uncontrolled and GA-LQR controlled displacement histories for impulse loading. In this case, the closed loop-damping ratio achieved has been 10.76 %. The variation of maximum actuator voltage for GA-LQR control scheme is shown in Fig. 7. 25 which is seen to be well within the maximum limit of actuator voltage. Fig. 7.26 shows the convergence of calculated fitness i.e. closed loop damping ratio with number of generation using GA-LQR search control scheme for doubly curved FRP composite shell panel under impulse loading at the center. The uncontrolled thermo-mechanical displacement histories with and without considering pyroelectric effect is shown in Fig 7.27. Fig. 7.28 shows the GA-LQR controlled displacement histories under thermo-mechanical loading without and with considering pyroelectric effect. In this case the closed loop damping ratios for

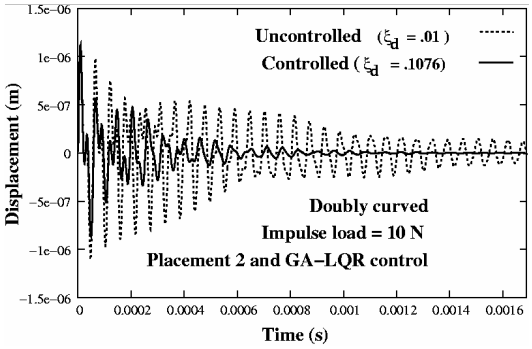

Fig. 7.24 Uncontrolled and controlled displacement history doubly curved panel under impulse loading

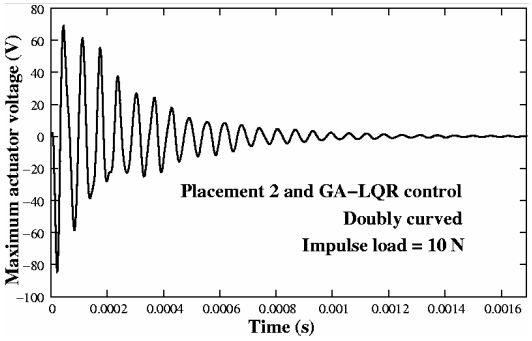

Fig. 7.25 Maximum actuator voltage variation for GA-LQR control scheme of doubly curved panel under impulse loading

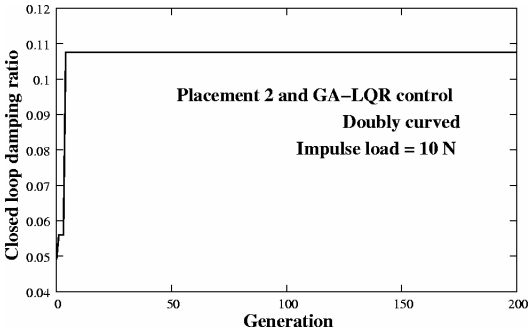

Fig. 7.26 Variation of closed loop damping ratio with generation of doubly curved panel under impulse loading

without pyroelectric and with pyroelectric effect are 4.57 % and 5.84 % respectively. The maximum actuator voltage variations for GA-LQR control scheme without and with considering pyroelectric effect is shown in Fig. 7.29. Even though the actuator voltage is higher in the case of considering pyroelectric effect, but the vibration suppression obtained for combined thermo-mechanical loading is also far more compared to that without considering pyroelectric effect. It should be noted that a part of this voltage is automatically generated by sensor due to pyroelectric effect. Fig. 7.30 shows the convergence of calculated fitness i.e. closed loop damping ratio with number of generation without and with considering pyroelectric effect for GA-LQR search control scheme. From this study it could also be concluded that optimal actuator placement using Placement2 and subsequent GA-LQR control scheme lead to the maximization of closed loop damping ratio for both mechanical as well as thermo-mechanical loading within the limit of input/actuator voltage.

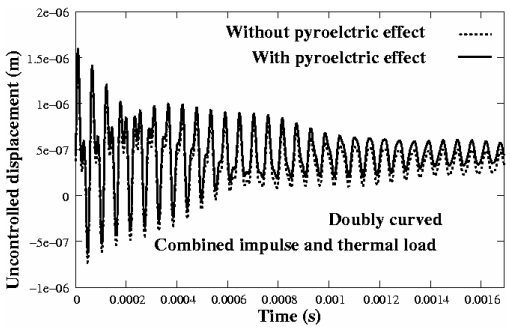

Fig. 7.27 Uncontrolled thermo-mechanical displacement history of doubly curved panel

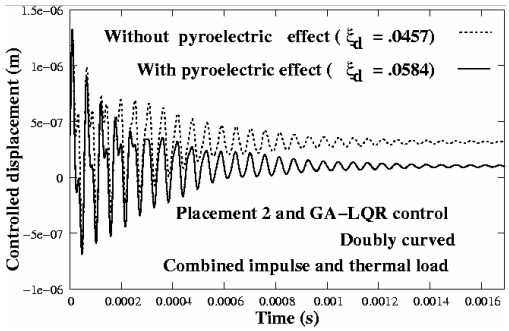

Fig. 7.28 Controlled displacement history of doubly curved panel

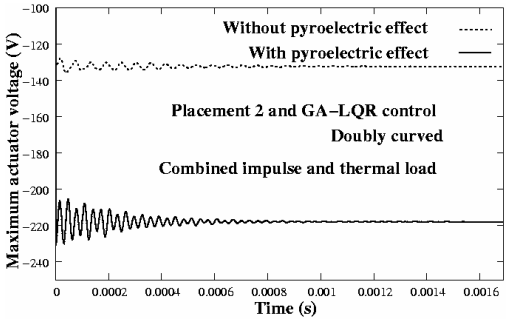

Fig. 7.29 Maximum actuator voltage variation of doubly curved panel due to thermo-mechanical loading

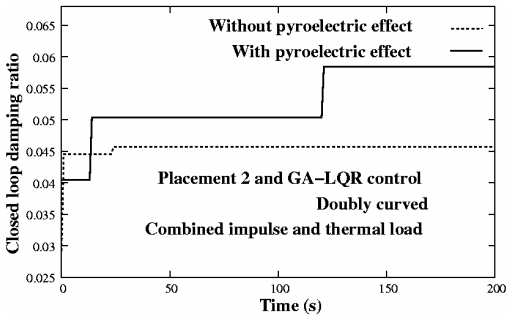

Fig. 7.30 Variation of closed loop damping ratio with generation of doubly curved panel due to thermo-mechanical loading

7.5 Optimal vibration control of laminated cylindrical shell panel

In this analysis a simply supported smart FRP composite cylindrical panel under the action of impulse load at the center as well as thermal load has been considered. Dimensions of this panel are $a = b = 20 \times 10^{-3}$ m, $R_1 = \infty$, $R_2 = 60 \times 10^{-3}$ m, $h = 2$ mm. This smart panel has been subjected to an impulse load of 10 N at the center for a duration of 3.84103 μs and impulse responses of the panel have been calculated with a time step of 0.9602594 μs. GA-LQR has been applied to control the displacement of the panel. Fig. 7.31 shows the uncontrolled and GA-LQR controlled histories for impulse loading. It could be observed from Fig. 7.31 that the closed loop damping ratio achieved with GA-LQR controlled is 8.74%. The maximum actuator voltage variations for GA-LQR control scheme under impulse loading is shown in Fig. 7.32 and it could be observed that input voltage required is much less from breakdown voltage of PZT actuators. Fig. 7.33 shows the convergence of calculated fitness with number of generation using GA-LQR control scheme for impulse loading.

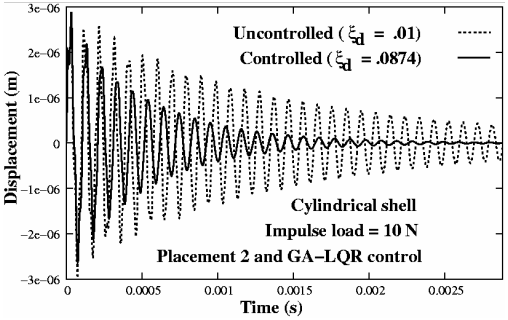

Fig. 7.31 Uncontrolled and controlled displacement history of cylindrical panel under impulse loading

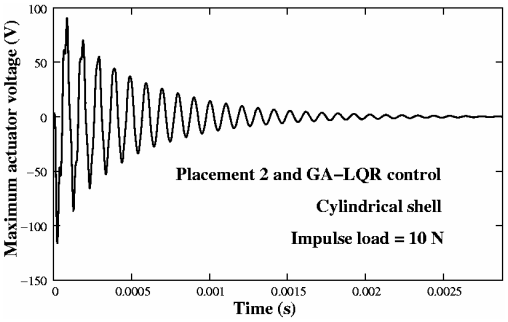

Fig. 7.32 Maximum actuator voltage variation of cylindrical panel under impulse loading

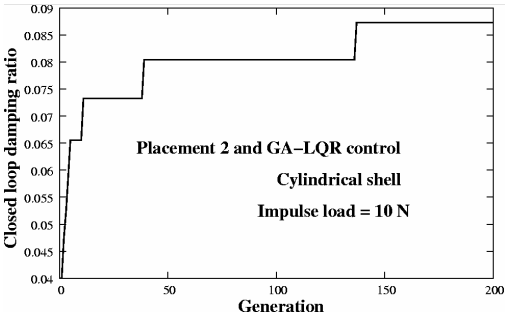

Fig. 7.33 Variation of closed loop damping ratio with generation for cylindrical shell under impulse loading

The Uncontrolled thermo-mechanical displacement histories with and without considering pyroelectric effect is shown in Fig 7.34. Fig. 7.35 shows the GA-LQR controlled displacement histories under thermo-mechanical loading without and with considering pyroelectric effect. In this case, the closed loop damping ratios for without and with pyroelectric effect are 17.85 % and 11.24 % respectively. The maximum actuator voltage variations for GA-LQR control scheme without and with considering pyroelectric effect is shown in Fig. 7.36. Fig. 7.37 shows the convergence of calculated fitness i.e. closed loop

damping ratio with number of generation considering without and with pyroelectric effect for GA-LQR search control scheme. It could also be observed that the damping ratio achieved is more in the case of without pyroelectric effect. However, better control of combined thermo-mechanical displacement has been achieved by considering pyroelectric effect which is clear from Fig. 7.35.

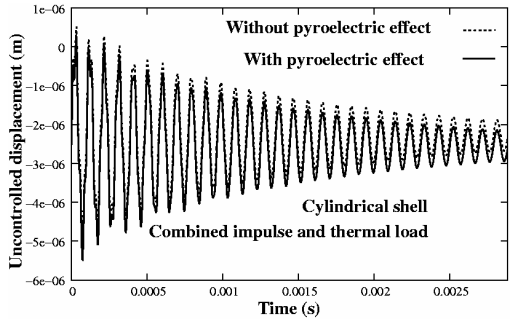

Fig. 7.34 Uncontrolled thermo-mechanical displacement history of cylindrical shell panel

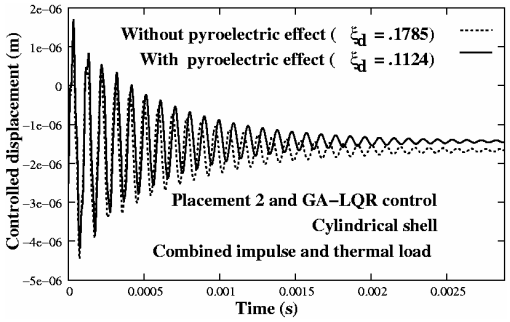

Fig. 7.35 Controlled displacement history of cylindrical shell panel

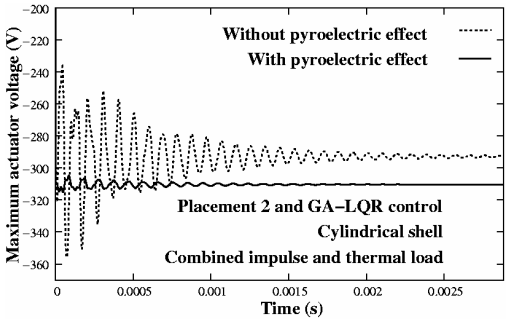

Fig. 7.36 Maximum actuator voltage variation of cylindrical panel due to thermo-mechanical loading

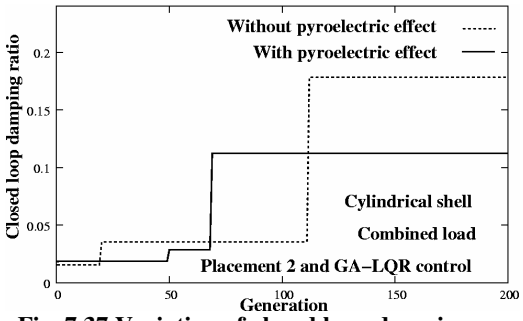

Fig. 7.37 Variation of closed loop damping ratio with generation of cylindrical shell panel due to thermo-mechanical loading

7.6 Summary

An improved GA based LQR control scheme has been developed in order to maximize closed loop damping ratio within the limit of input/actuator voltage for optimal active vibration control of smart FRP composite shell structures under mechanical as well as thermo-mechanical loading. In the present method only three weighting factors have been used to search optimal [*Q*] and [*R*] matrices using improved real coded genetic algorithm, which reduces chromosome length and hence minimizes computational time. Several composite shell panels have been analyzed for optimal vibration control of such structures using this module with different schemes of optimal placement of actuators. From this study the following important observations have been made

1. Optimal placement scheme based on control spillover has been observed to give maximum closed loop damping.

2. GA-LQR control scheme has been observed to find better optimal gain compared to conventional LQR scheme leading to a much higher effective closed loop damping.
3. The proposed GA-LQR control scheme could control both dynamic oscillation as well as static displacement due to thermal gradient under combined thermo-mechanical loading.

CHAPTER 8

Conclusions and Scope of Further Work

This chapter presents the important conclusions based on the finite element analysis and optimal active vibration control of different kinds of smart FRP composite shell structures using methodologies developed in the present work. Scope of further work in this direction has also been presented at the end of this chapter.

8.1 Conclusions

An eight noded improved layered shell finite element has been developed for piezo-thermo-elastic analysis of smart FRP composite structures with surface bonded PZT sensors and actuators patches for the analysis of deep as well as shallow shells based on the stress resultant-type Koiter's shell theory including transverse shear effect according to the Mindlin's hypothesis. An integer coded genetic algorithm with uniform crossover and a new mutation techniques has been developed for determination of optimal placement of collocated piezoelectric sensors and actuators in order to maximize the controllability index by minimizing control spillover of the higher modes. An improved real coded GA based LQR control scheme has been developed in order to maximize closed loop damping ratio within the limit of input/actuator voltage for optimal active vibration control of smart FRP composite shell structures under mechanical as well as thermo-mechanical loading. A complete computer code stating from finite element analysis of smart FRP composite shell structures, determination of optimal actuators placement using GA and GA based LQR control scheme has been developed for the analysis and active vibration control of FRP composite shell structures. The developed computer code has been validated for all possible kinds of load cases before using the same for analysis and design of smart shell structures. After validation of this module, several smart FRP composite shell panels have been analyzed for optimal vibration control of such structures using this module with different schemes of optimal placement of actuators. Important conclusions obtained from the present study has been categorized into two categorizes

1) Conclusions regarding FE analysis of smart FRP composite shell structures
2) Conclusions regarding optimal control of smart FRP composite shell structures

Conclusions based on FE Analysis

i. The developed layered shell finite element can model smart FRP composite shell structures for any number of layers of composite as well as piezoelectric materials.

ii. The present finite element formulation is capable of modeling distributed piezo sensors and actuators as well as piezo patches bonded at discrete locations.

iii. The present finite element can model both thick as well as thin smart FRP composite structures.

iv. Present finite element formulation can determine the complete electro-thermo-mechanical responses of both deep and shallow smart shell structures considering pyroelectric effect.

v. Incorporation of pyroelectric effect is of significant importance in accurate determination of responses of smart structures under thermo-mechanical loading.

vi. If pyroelectric effect is not considered in the coupled finite element formulation, then the sensors voltages are underestimated and the sensor voltage might exceed the breakdown voltage of the piezo patches without the knowledge of the analyst.

vii. Dependency of displacement and hence the sensors voltages on R/a ratio of shells is more pronounced in deep shell region up to $R/a = 50$ in all the cases.

viii. For the same thermo-mechanical loading, cylindrical shell shows maximum deflection and doubly curved shell shows the minimum deflection and this difference is more pronounced for $R/a>50$.

Conclusions based on Optimal Control

ix. The proposed integer coded GA (ICGA) along with new uniform crossover and mutation techniques for determination of optimal actuator placement leads to far better controllability compared to that of conventional binary coded GA.

x. Consideration of higher mode control spillover leads to better optimal placement of actuators compared to that of without considering spillover.

xi. Mode shape based placement will not be effective when more number of modes gets excited. In such cases, the proposed integer coded GA based scheme will work better.

xii. ICGA based optimal placement of actuators considering control spillover leads to almost four times more effective closed loop damping compared to that obtained from mode shape based placements.

xiii. GA-LQR control scheme developed in the present study could find better optimal gain compared to conventional LQR scheme leading to a much higher effective closed loop damping.

xiv. The proposed improved GA-LQR control scheme could control both dynamic oscillation due to mechanical loading and static displacement due to thermal gradient under combined thermo-mechanical loading which was not possible with conventional LQR method

xv. Combination of control spillover based placement along with GA-LQR control scheme leads to maximum effective closed loop damping.

xvi. GA-LQR control scheme could efficiently control the thermo-mechanical responses while keeping the actuator voltages within the limit of break down voltage.

xvii. Pyroelectric effect has a significant effect in design of optimal LQR control scheme. If the controller gain is designed without pyroelectric effect, then the actuator voltages could be overestimated for more control of thermally induced static offset.

xviii. Different kinds of shell structures have been analyzed for optimal vibration control under mechanical as well as thermo-mechanical loading using control spillover based actuators placement and GA-LQR control schemes and it has been observed that optimal vibration control of such shell structures are achieved using this combined module.

8.2 Scope of further work

- This work could be extended to non-collocated sensors and actuators optimal locations
- Optimal sensors and actuators placement of large structures requiring large number of sensors and actuators could be tried.
- Parallelizing the optimal placement evaluation could be tried.
- Multi-objective optimization considering both structural design as well as control performance could be tried.
- Strain dependent non-linear behavior of piezoelectric patches could be incorporated.

REFERENCES

[1] J. Curie, P. Curie, Piezo effect in quartz and some other materials, C. R. *Acad. Sci., Paris* (1880) 294-383.

[2] E. Fukada, Piezoelectricity in polymers and biological materials, *Ultrasonic* 6 (1968) 229-234.

[3] H. Kawai, The piezoelectricity of polyvinylidene pluoride, *Japan Journal of Applied Physics* (1969) 8-975.

[4] H. Allik, T. J. R. Hughes, Finite element method for piezoelectric vibration, *International Journal for Numerical Methods in Engineering* 2 (1970) 151-157.

[5] E. F. Crawley, J. D. Luis, Use of piezoelectric actuators as elements of intelligent structures, *AIAA J*. 25(10) (1987) 1373-1385.

[6] H. S. Tzou, C. I. Tseng, Distributed piezoelectric sensor/actuator design for dynamic measurement/control of distributed parameter systems: A Finite Element Approach, *Journal of Sound and Vibration* 138(1) (1990) 17-34.

[7] C. K. Lee, Theory of laminated piezoelectric plates for the design of distributed sensors/actuators Part 1: Governing equations and reciprocal relationships. *J. Acoustical Soc. Amer.* 87 (3) (1990)1144-1158.

[8] W. S. Hwang, H. C. Park, Finite element modeling of piezoelectric sensors and actuators, AIAA Journal, 31(5) (1993) 930-937.

[9] D. A. Saravanos, Mixed laminate theory and finite element for smart piezoelectric shell structure, *AIAA J.* 35(8) (1997) 1327-1333.

[10] H. Abramovich, B. Pletner, Actuation and sensing of piezolaminated sandwich type of structures, *Composite Structures* 38(1) (1997) 17-27.

[11] A. R. Faria, S. F. Muller, Axisymmetric actuation of composite cylindrical thin shells with piezoelectric rings, *Smart Mater. Struct.* 7 (1998) 843-850.

[12] J. S. Yang, Equations for thick elastic plates with partially electroded piezoelectric actuators and higher order electric fields, *Smart Mater. Struct.* 8 (1999) 73-82.

[13] D. H. Robins, J. N. Reddy, Analysis of piezoelectrically actuated beams using a layer wise displacement theory, *Composite Structures* 41(2) (1991) 265-279.

[14] C. K. Lee, W. W. Chaing, T. C. O'Sullivan, Piezoelectric modal sensor/actuator pairs for critical active damping vibration control, *The Journal of Acoustical Society of America* 90 (1991) 374-384.

[15] S. K. Agarwal, D. Tong, K. Nagaraja, Modeling and shape control of piezoelectric actuator embedded elastic plates, *Journal of Intelligent Material Systems and Structures* 5 (1994) 514-521.

[16] H. F. Tiersten, Equations for the control of the flexural vibrations of composite plates by partially electroded piezoelectric actuators. In: Anderson GL, Lagoudas DC editors, *Active materials and smart structures, SPIE Proceedings Series*, 1994, 2427, 326-42.

[17] M. Preiswerk, A. Venkatesh, Analysis of vibration control using piezoceramics in planar flexible-linkage mechanisms, *Smart Mater. Struct.* 3(2) (1994) 190-200.

[18] S. E. Miller, H. Abramoich, Y. Oshman, Active distributed vibration control of anisotropic piezoelectric laminated plates, *Journal of Sound and Vibration* 183 (1995) 797-817.

[19] J. S. Yang, Equations for the flexural motions of elastic plates with partially electroded piezoelectric actuators, *Smart Mater. Struct.* 6 (1997) 485-490.

[20] J. S. Yang, Equations for the flexural motions of elastic plates with partially electroded piezoelectric actuators in flexure with shear deformation and rotary inertia, *Journal of Intelligent Material Systems and Structures* 8 (1997) 444-451.

[21] D. Tong, R. L. Williams II, S. K. Agarawal, Optimal shape control of composite thin plates with piezoelectric actuators, *Journal of Intelligent Materials, Systems and Structures* 9 (1998) 458-467.

[22] K. Y. Lam, T. Y. Ng, Active control of composite plates with integrated piezoelectric sensors and actuators under various dynamic loading conditions, *Smart Mater. Struct.* 8 (1999) 233-237.

[23] K.S. Ha, C. Keilers and F.K. Chang, Finite element analysis of composite structures containing distributed piezoceramic sensors and actuators, *AIAA J* 30 (3) (1992) 772–780.

[24] M. C. Ray, R. Bhattacharyya, B. Samanta, Static Analysis of Intelligent Structure by the Finite Element Method, *Computers & Structures*. 52(4) (1994) 617-631.

[25] A. Suleman, V.B. Venkayya, Flutter control of an adaptive laminated composite panel with piezoelectric layers, *IDMEC-Instituto Superior Tecnico, Department de Engenharia Mecanica*, 1096 Codex, Portugal, 1995.

[26] A. Suleman, M. A. Goncalves, Optimization issues in application of piezoelectric actuators in panel flutter control, *MEC-Instituto Superior Tecnico, Department de Engenharia Mecanica*, 1096 Codex, Portugal, 1995.

[27] D. T. Detwiler, M. H. H. Shen, V. B. Venkayya, Finite element analysis of laminated composite structures containing distributed piezoelectric actuators and sensors, *Finite Elements in Analysis and Design* 20 (1995) 87-100.

[28] H. S. Tzou, R. Ye, Analysis of piezoelectric structures with laminated piezoelectric triangle shell elements, *AIAA J.* 34 (1996) 110-115.

[29] V. Piefort, N. Loix, A. Preumont, Modeling of piezolaminated composite shells for vibration control, *Active Structural Laboratories*, 1998.

[30] C. Y. K. Chee, L. Tong, G. P. Steven, A mixed model for composite beams with piezoelectric actuators and sensors, *Smart Mater. Struct.* 8 (1999) 417-432.

[31] S. H. Chen, G. F. Yao, C. Huang, A new intelligent thin shell element, *Smart Mater. Struct.* 9 (2000)10-18.

[32] K.Y. Sze, L. Q. Yao, Modeling smart structures with segmented piezoelectric sensors and actuators, *Journal of Sound and Vibration* 235(3) (2000) 495-520.

[33] A. Benejeddou, Advances in piezoelectric finite element modeling adaptive structural elements: a survey, *Computers & Structures* 76 (2000) 347-363.

[34] J. G. Wan, B. Q. Tao, Design and study on a 1-3 anisotropy piezocomposite sensor, *Materials & Design* 21 (2000) 533-536.

[35] V. Piefort, A. Preumont, Finite element modeling of piezoelectric structures, *Active Structure Laboratories*, 2001.

[36] V. Balagurugan, S. Narayanan, Active vibration control of smart shells using distributed piezoelectric sensors and actuators, *Smart Mater. Struct.* 10 (2001) 173-180.

[37] A. Mukherjee, S.P. Joshi, A. Ganguli, Active vibration control of piezolaminated stiffened plates, *Composite Structures* 55 (2002) 435–443.

[38] S. Lee, N. S. Goo, H. C. Park, K. J. Yoon, C. Cho, A nine-node assumed strain shell element for analysis of a coupled electro-mechanical system. *Smart Mater. Struct.* 12 (2003) 355-362.

[39] S. A. Kulkarni, K. M. Bajoria, Finite element modeling of smart plates/shells using higher order shear deformation theory, *Composite Structures* 62 (2003) 41-50.

[40] S. Zheng, X. Wang, W. Chen, The formulation of refined hybrid enhanced assumed strain solid shell element and its application to model smart structures containing distributed piezoelectric sensors/actuators, *Smart Mater. Struct.* 13 (2004) N43-N50.

[41] Z. K. Kusculuoglu, T. J. Royston, Finite element formulation for composite plates with piezoelectric layers for optimal vibration control applications, *Smart Mater. Struct.* 14 (2005) 1139-1153.

[42] S. Lentzen, R. Schmidt, Nonlinear finite element modeling of vibration control of piezolaminated composite plates and shells *Smart Structures and Materials 2005: Damping and Isolation (Bellingham, WA)*; *Proc. SPIE* , 2005, 5760-16.

[43] S. Lentzen, R. Schmidt, A geometrically nonlinear finite element for transient analysis of piezolaminated shells *Proc. Conf. on 5th EUROMECH Nonlinear Dynamics (Eindhoven)*, 2005, 2492–500.

[44] S. Lentzen, R. Schmidt, Large amplitude vibrations and modal sensing of intelligent thin piezolaminated structures *EURODYN 2005, Proc. 6th European Conf. on Structural Dynamics (Paris),* 2005, 569–74.

[45] S. Lentzen , R. Schmidt 2005 Nonlinear transient analysis, vibration control and modal sensing of smart piezolaminated shells *Advances in Computational & Experimental Engineering and Science* (Encino, CA: Tech Science Press) pp 2062–67

[46] O. Polit, I. Bruant, Electric potential approximations for an eight node plate finite element, *Computes and Structures* 84 (2006) 1480-1493.

[47] V. Balagurugan, S. Narayanan, A piezoelectric higher-order plate finite for the analysis of multi-layer smart composite laminates, *Smart Mater. Struct.* 16 (2007) 2026-2039.

[48] S. Lentzen, P. Klosowski, R. Schmidt, Geometrically nonlinear finite element simulation of smart piezolaminated plates and shells, *Smart Mater. Struct.* 16 (2007) 2265–2274.

[49] W.N. Akl, A. Baz, Finite element modeling of smart foam for active vibration and noise control applications, *Mechanics of Advanced Materials and Structures* 14 (6) (2007) 477-498.

[50] A. E. Sabbagh, W. Akl, A. Baz, Topology optimization of periodic Mindlin plates, *Finite Elements in Analysis and Design* 44 (2008) 439 – 449.

[51] K. S. S. Ram, S. K Kiran, Static behavior of laminated composite spherical shell cap with piezoelectric actuators, *Smart Mater. Struct.* 17 (2008) 015010 (9pp).

[52] D. Marinković, H. Köppe, U. Gabbert, Degenerate shell element for geometrically nonlinear analysis of thin-walled piezoelectric active structures, *Smart Mater. Struct.* 17 (2008) 015030 (10pp)

[53] V. Balagurugan, S. Narayanan, A piezolaminated composite degenerated shell finite element for active control of structures with distributed piezosensors and actuators, *Smart Mater. Struct.* 17 (2008) 015031 (18pp)

[54] L. H. Donnel, A Discussion of the thin Shell Theory, In: Proceeding of 5th International Congress of Applied Mechanics, John Wiley, New York, 1938, pp. 66-70.

[55] J. L. Sanders, An improved first approximation theory for thin shells, *NASA Tech Report*, R-24, 1955.

[56] V.V. Novozhilov, The theory of thin shells, *P. Noordhoff Ltd Lieden*, 1959.

[57] W. T. Koiter, A Consistent First Approximation of the General Theory of Thin Elastic Shell, *In: Proceeding of 1st IUTAM Symposium, North Holland, Amsterdam*, 1960, 12-33.

[58] J. L. Vlasov, General Theory of Shells and its applications in Engineering, *NASA TT F-99*, Washington, 1964.

[59] C.W. Bert, V. S. Reddy, Cylindrical Shells of bimodulus materials, *Journal of engineering Mechanics Division, ASCE*, 8 (EM5) (1982) 675-688.

[60] A. E. H. Love, On the small free vibrations and Deformations of the elastic shells, *Philosophical Transaction of the Royal Society* 17, (1988) 491-546.

[61] L. Sk, P. K. Sinha, Improved Finite Element Analysis of Multilayered Doubly Curved Composite Shells, *Journal of Reinforced Plastics and Composites* 24 (2005) 385-404.

[62] T. R. Tauchert, P. J. Beresford, E. L. Wilson, Piezothermoelastic behavior of a laminate, *Journal of Thermal stresses* 15 (1992) 25-37.

[63] K. D. Jonnalagadda, G. E. Blanford, T. R. Tauchert, Piezothermoelastic composite plate analysis using first-order Shear Deformation theory, *Journal of computers and structures*, 51 (1) (1994) 79-89.

[64] H. S. Tzou, R. Ye, Piezothermoelasticity and precision control of active piezoelectric laminates, *ASME Journal of* V*ibration and Acoustics* 114 (1994) 489-495

[65] K. Xu, A. K. Noor, Three dimensional analytical solutions for coupled thermoelectroelastic response of multilayered cylindrical shells, *AIAA J.* 34 (1996) 802-812.

[66] H. S. Tzou, R. Ye, Pyroelectric and Thermal Strain Effects Of Piezoelectric (PVDF and PZT) Devices, *Mechanical Systems and Signal Processing* 10 (4) (1996) 459-469.

[67] H. J. Lee, D.A. Saravanos, Coupled layerwise analysis of thermo piezoelectric composite beams, *AIAA J.* 34(6) (1996)1231-1237.

[68] F. L. Shang, Z. K. Wang, Z. H. Li, Cylindrical buckling of piezoelectric laminated plates, *Acta Mechanica Solida Sinica* 18 (1997) 101-108.

[69] R. C. Batra, X. Q. Liang, J. S. Yang, Shape control of vibrating simply supported rectangular plates *AIAA J.* 14 (1996)116–22l

[70] R. C. Batra, X. Q. Liang, Finite dynamic deformations of smart structures *Comput. Mech.* 20 (1997) 427–38.

[71] A. Chattopadhyay, L. Jingmei, G. Haozhong, A coupled thermo-piezoelectric-mechanical model for smart composite laminates, *AIAA*-98-2044.

[72] L. Jingmei, Z. Xu, G. Haohong, A. Chattopadhyay, Dynamic responses of smart composites using a coupled thermo-piezoelectricmechanical model, *AIAA*-99-1481.

[73] G. E. Blandford, T. R. Tauchert, Y. Du, Self-strained piezothermoelastic composite beam analysis using first-order shear deformation theory, *Composites Part B 30* (1999) 51-63.

[74] R. Ye, H. S. Tzou, Control of Adaptive Shells with Thermal and Mechanical Excitations, *Journal of Sound and* V*ibration* 231(5) (2000) 1321-1338.

[75] T. R. Tauchert, F. Ashida, N. Noda, S. Adali, V. Verijenko, Developments in thermo-piezoelasticity with relevance to smart composite structures, *Composite Structures* 48 (2000) 31–38.

[76] D. HaoJiang, G. FengLin, H. PengFei, A general solution for piezothermoelasticity of transversely isotropic piezoelectric materials and its applications, *International Journal of Engineering Science* 38 (2000) 1415–1440.

[77] H. S. Kim, A. Chattopadhyay, C. Nam, Implementation of a coupled thermo-piezoelectric-mechanical model in the LQG controller design for smart composite shells, *Journal of intelligent material systems and structures* 13 (2002) 713-724.

[78] G. A. Altay, M. C. Do¨kmeci, A non-linear rod theory for high-frequency vibrations of thermopiezoelectric materials, *International Journal of Non-linear Mechanics* 37 (2002) 225–243.

[79] S. S. Vel, R.C. Batra, Cylindrical bending of laminated plates with distributed and segmented piezoelectric actuators/sensors, *AIAA J.* (2000) 38, 857–867.

[80] S. S. Vel, R.C. Batra, Generalized plane strain thermopiezoelectric analysis of multilayered plates. *J. Thermal Stresses* 26 (2003) 353–377.

[81] G. Song, X. Zhou, W. Binienda, Thermal deformation compensation of a composite beam using piezoelectric actuators, *Smart Mater. Struct.* 13 (2004) 30–37.

[82] G. A. Altay, M.C. Do¨ kmeci, The consistent Mindlin's thermopiezoelectric equations and the principle of virtual work, *Mechanics Research Communications* 32 (2005) 115–119.

[83] K.M. Liew, Jordan Z. Zhang, C. Li, S.A. Meguid, Three-dimensional analysis of the coupled thermo-piezoelectro-mechanical behaviour of multilayered plates using the differential quadrature technique, *International Journal of Solids and Structures* 42 (2005) 4239–4257.

[84] F. Heidary, M. R. Eslami, Piezo-control of forced vibrations of thermoelastic composite plate, *Journal of composite structures* 74 (2006) 99-105.

[85] R. Kumar, B. K. Mishra, S. C. Jain, Thermally induced vibration control of cylindrical shell using piezoelectric sensor and actuator, *Int J Adv Manuf Technol*, DOI 10.1007/s00170-007-1076-y.

[86] J. P. Jiang, D. X. Li, A new finite element model for piezothermoelastic composite beam, *Journal of sound and vibration* 306 (2007) 849-864.

[87] S. L. Padula, R. K. Kincaid, Optimization strategies for sensor and actuator placement, *Technical Report* NASA/TM-1999-209126.

[88] M. I. Frecker, Recent advances in optimization of smart structures and actuators, *J. Intell. Mater. Syst. Struct.* 14 (2003) 207–216.

[89] J. J. Hollkamp, Multimodal passive vibration suppression with piezoelectric materials and resonant shunts, *J. Intell. Mater. Syst. Struct.* 5 (1994) 49–57.

[90] Y. K. Kang, H. C. Park, W. Hwang , K. S. Han, Optimum placement of piezoelectric sensor/actuator for vibration control of laminated beams, *AIAA Journal* 34 (1996) 1921–1926.

[91] N. Zhang, I. Kirpitchenko, Modelling dynamics of a continuous structure with a piezoelectric sensor/actuator for passive structural control, *Journal of Sound and Vibration* 249 (2) (2002) 251-261.

[92] J. A Main, E. Garcia, D. Howard, Optimal placement and sizing of paired piezoactuators in beam plate, *Smart Mater. Struct.* 3 (1994) 373-381.

[93] Y. Li, J. Onoda, K Minesugi, Simultaneous optimization of piezoelectric actuator placement and feedback for vibration suppression, *Acta Astronaut.* 50 (2002) 335–341.

[94] Y. K. Kang, H. C. Park, B. Agrawal, Optimization of piezoceramic sensor/actuator placement for vibration control of laminated plates, *AIAA Journal* 36 (1998)1763–1765.

[95] K. Hiramoto, H. Doki, G. Obinata, Optimal sensor/actuator placement for active vibration control using explicit solution of algebraic Riccati equation, *Journal of Sound and Vibration* 229 (5) (2000) 1057-1075.

[96] A. Mukherjee, S. P. Joshi, Design of Actuator Profiles for Minimum Power Consumption, *Smart Mater. Struct.* 10(2) (2001) 305–313.

[97] Q. Wang, C. Wang, A controllability index for optimal design of piezoelectric actuators in vibration control of beam structures, *Journal of Sound and Vibration* 242 (3) (2001) 507-518.

[98] F. Seeger, U. Gabbert, Optimal placement of distributed actuators for a controlled smart elastic plate, *Proc. Appl. Math. Mech.* 2 (2003) 262–263.

[99] D. Sun, L. Tong, D. Wang, Vibration control of plates using discretely distributed piezoelectric quasi-modal actuators/sensors, *AIAA Journal* 39 (2001) 1766–1772.

[100] D. Sun, L. Tong, Modal control of smart shells by optimized discretely distributed piezoelectric transducers, *Int. J. Solids Struct.* 38 (2001) 3281–3299.

[101] S. Leleu, H. Abou-Kandil, Y. Bonnassieux, Piezoelectric Actuators and Sensors Location for Active Control of Flexible Structures, *IEEE Transactions On Instrumentation And Measurement* 50 (6) (2001) 1577-1582.

[102] M. R. Kermani, M. Moallem, R. V. Patel, Optimizing the Performance of Piezoelectric Actuators for Active Vibration Control, *Proceedings of the* 2002 *IEEE, International Conference on Robotics & Automation, Washington, DC , May* 2002.

[103] M. Rose, Modal based correction methods for the placement of piezoceramic modules, *ASME Int. Mechanical Engineering Congr. and Exposition, Orlando, FL, Nov.* 2005.

[104] D. Halim, S. O. R. Moheimani, An optimization approach to optimal placement of collocated piezoelectric actuators and sensors on a thin plate, Mechatronics 13 (2003) 27–47.

[105] D. Sun, L. Tong, Design optimization of piezoelectricactuator patterns for static shape control of smart plates, *Smart Mater. Struct.* 14 (2005) 1353–1362.

[106] R. C. Carbonari, E. C. N. Silva, S. Nishiwaki, Optimum placement of piezoelectric material in piezoactuator design, *Smart Mater. Struct.* 16 (2007) 207–220.

[107] S. S. Rao, T-S Pan, V. B. Venkayya, Optimal placement of actuators in actively controlled structures using genetic algorithms, *AIAA Journal* 29 (1991) 942–943.

[108] Y. J. Yan, L. H. Yam, Optimal design of number and locations of actuators in active vibration control of a space truss, *Smart Mater. Struct.* 11 (2002) 496–503.

[109] J. A. Bishop, A. G. Striz, On using genetic algorithms for optimum damper placement in space trusses, *Struct. Multidisciplinary Optim.* 28 (2004)136–145.

[110] M. M.Abdullah, A. Richardson, J. Hanif, Placement of sensors/actuators on civil structures using genetic algorithms, *Earthquake Engineering & Structural Dynamics* 30 (8) (2001) 1167-1184.

[111] A. Richardson, M. M. Abdullah, Sensor/actuators placement on civil structures using a real coded genetic algorithm, *SPIE Smart Structures and Materials—Smart Systems for Bridges, Structures, and Highways , San Diego, CA,* pp. 244–255 2002.

[112] P. Gaudenzi, E. Fantini, V. K. Koumousis, C J Gantes, Genetic algorithm optimization for the active control of a beam by means of PZT actuators *J. Intell. Mater. Syst. Struct.* 9 (1998) 291–300.

[113] H. Zhang, B. Lennox, P. R. Goulding, A. Y. T. Leung, A float-encoded genetic algorithm technique for integrated optimization of piezoelectric actuator and sensor placement and feedback gains, *Smart Mater. Struct.* 9 (2000) 552–557.

[114] Y. Yang, Z. Jin, C. K. Soh, Integrated optimal design of vibration control system for smart beams using genetic algorithms, *Journal Sound and Vibration* 282 (2005) 1293–1307.

[115] Y. Yang, Z. Jin, C. K. Soh, Integrated optimization of control system for smart cylindrical shells using modified GA, *J. Aerosp. Eng.* 19 (2006) 68–79.

[116] J-H Han, I. Lee, Optimal placement of piezoelectric sensors and actuators for vibration control of a composite plate using genetic algorithms, *Smart Mater. Struct.* 8 (1999) 257–267.

[117] A. M. Sadri, J. R. Wright, R. J. Wynne, Modelling and optimal placement of piezoelectric actuators in isotropic plates using genetic algorithms, *Smart Mater. Struct.* 8 (1999) 490–498.

[118] A. M. Sadri, J. R. Wright, R. J. Wynne, LQG control design for panel flutter suppression using piezoelectric actuators, *Smart Mater. Struct.* 11 (2002) 834–839.

[119] S. T. Quek, S. Y. Wang, K. K. Ang, Vibration control of composite plates via optimal placement of piezoelectric patches, *J. Intell. Mater. Syst. Struct.* 14 (2003) 229–245.

[120] H. Y. Guo, L. Zhang, L. L. Zhang, J. X Zhou, Optimal placement of sensors for structural health monitoring using improved genetic algorithm, *Smart Mater. Struct.* 13 (2004) 528-534.

[121] Q. S. Li, D. K Liu, J. Tang, N. Zhang, C. M. Tam, Combinatorial optimal design of number and positions of actuators in actively controlled structures using genetic algorithm, *Journal of Sound and Vibration* 270 (2004) 611-624.

[122] F. Peng, A. Ng, Y-R Hu, Actuator placement optimization and adaptive vibration control of plate smart structures, *J. Intell. Mater. Syst. Struct.* 16 (2005) 263–271.

[123] S. Y. Wang, K. Tai, S. T. Quek, Topology optimization of piezoelectric sensors/actuators for torsional vibration control of composite plates, *Smart Mater. Struct.* 15 (2006) 253–269.

[124] W. Liu, Z. K.Hou, M. A. Demetriou, A computational scheme for the optimal sensor/actuator placement of flexible structures using spatial H-2 measures, *Mechanical Systems and Signal Processing* 20 (4) (2006) 881-895.

[125] A. K. Jha, D. J. Inman, Optimal sizes and placements of piezoelectric actuators and sensors for an inflated torus, *J. Intell. Mater. Syst. Struct.* 14 (2003) 563–576.

[126] A. Belloli, P. Ermanni, Optimum placement of piezoelectric ceramic modules for vibration suppression of highly constrained structures, *Smart Mater. Struct.* 16 (2007) 1662-1671.

[127] D. J. Inman, *Vibration: with control, measurement and stability*, Prentice Hall, Englewood Cliffs, London, 1989.

[128] L. Meirovitch, *Dynamics and control of structures*, John Wiley & Sons, New York, 1990.

[129] H. S. Tzou, *Piezoelectric shells: distributed sensing and control of continua*, Kluwer Academic Publishers, Dordrecht, 1993.

[130] C. R. Fuller, S. J. Elliott, P. A. Nelson, *Active control of vibration*, Academic Press, London, 1996.

[131] R. L. Clark, W. R. Saunders, G. P. Gibbs, *Adaptive structures: dynamics and control*, John Wiley & Sons, New York,1998.

[132] A. Preumont, *Vibration control of active structures: an introduction*, Kluwer Academic Publishers, 2nd edition Dordrecht, 2002.

[133] J. H. Han, K. H. Rew, I. Lee, An experimental study of active vibration control of composite structures with a piezo-ceramic actuator and a piezo-film sensor, *Smart Mater. Struct.* 6(5) (1997) 549–558.

[134] R. Alkhatib, M. F. Golnaraghi, Active structural vibration control: a review, *Shock Vib Dig* 35(5) (2003) 367–383.

[135] B. S. Chen, T. Y. Dong, LQG optimal control system design under plant perturbation and noise and noise uncertainty: A state-space approach, *Automatica* 25 (3) (1989) 431-436.

[136] M. C. Ray, Optimal Control of Laminated Plate with Piezoelectric Sensor and Actuator Layers, AIAA J., 36 (12) (1998) 2204–2208.

[137] S. M. S Alam, K. Yamada, S. Baba, A Kalman Filter approach for galloping control of a bridge tower, *Computers and Strutctures 57* (1) (1995) 67-79.

[138] B. J. Moore, X. Y. Zhou, A. E. B. Lim, Discrete time LQG controls with control dependent noise, *Systems and Control Letters* 36 (1999) 199-206.

[139] W. Chen, M. Buehler, G. Parker, B. Bettig, Optimal Sensor Design and Control of Piezoelectric Laminated beams, *IEEE Transactions on Control Systems and Technology* 12 (1), 2001.

[140] M. A Trindade, A. Benjeddou, R. Ohayon, Piezoelectric active vibration control of damped sandwich beams, *Journal of Sound and Vibration* 246(4) (2001) 653-677.

[141] P. Bhattacharya, H. Suhail, P. K. Sinha, Finite element analysis and distributed control of laminated composite shells using LQR/IMSC approach, *Aerospace Science and Technology* 6 (2002) 273–281.

[142] K. K. Ang, S.Y. Wang, S. T. Quek, Weighted energy linear quadratic regulator vibration control of piezoelectric composite plates, *Smart Mater. Struct.* 11 (2002) 98-106.

[143] A. M Sadri, J. R Wright, R J Wynne, LQG control design for panel flutter suppression using piezoelectric actuators, *Smart Mater. Struct.* 11 (2002) 834-839.

[144] V. Balamurugan, S.Narayanan, Finite element formulation and active vibration control study on beams using smart constrained layer damping (SCLD) treatment, *Journal of Sound and Vibration* 249(2) (2002) 227-250.

[145] I. R Petersen, H. R Pota, Minimax LQG optimal control of a flexible beam, *Control Engineering Practice* II (2003)1273-1287.

[146] S. Narayanan, V. Balamurugan, Finite element modeling of piezolaminated smart structures for active vibration control with distributed sensors and actuators, *Journal of Sound and Vibration* 262 (2003) 529–562.

[147] W. Chen, M. Buehler, G. Parker, B. Bettig, Optimal sensor design and control of piezoelectric beams, *IEEE Transanctions on Control Systems Technology* 12 (1), 2004.

[148] N. K. Chandiramani, L. I. Librescu, V. Saxena1 and A Kumar, Optimal vibration control of a rotating composite beam with distributed piezoelectric sensing and actuation, *Smart Mater. Struct.* 13 (2004) 433–442.

[149] G. E. Stavroulakis, G. Foutsitzi, E. Hadjigeorgiou, D. Marinova, C.C Baniotopoulos, Design and robust optimal control of smart beams with application on vibration suppression, *Advances in Engineering Software* 36 (2005) 806-813.

[150] S. H. Moon, J. S. Hwang, Panel flutter suppression with an optimal controller based on the nonlinear model using piezoelectric materials, *Composite Structures* 68 (2005) 371-379.

[151] R. Kumar, S.P Singh, H..N. Chandrawat, Multivariable adaptive vibration control of smart structures using iterative (LQG) control strategies, *Smart Mater. Struct.* 14(2005) 953-962.

[152] C. H. Park, A. Baz, Vibration control of beams with negative capacitive shunting of interdigital electrode piezoceramics, *Journal of vibration control* 11(3) (2005) 331-346.

[153] S. H. Moon, Finite element analysis and design of control system with feedback output using piezoelectric sensor/actuator for panel flutter suppression, *Finite Elements in Analysis and Design* 42 (2006) 1071-1078.

[154] C.M.A Vasques, J. D. Rodrigues, Active vibration control of smart piezoelectric beams: Comparison of classical and optimal feedback control strategies, *Computers and Structures* 84 (2006) 1402-1414.

[155] J. Wang, W. S. Shepard Jr, K. A. Williams, C. B. Gattis, Active vibration control of a plate-like structure with discontinuous boundary conditions, *Smart Mater. Struct.*15 (2006) N51-N60.

[156] F-H Hsiao, S-D Xu, S-L Wu, G-C Lee, LQG optimal control of discrete stochastic systems under parametric and noise uncertainties, *Journal of Franklin Institute* 343 (2006) 279-294.

[157] B. B. King, N. Hovakimyan, K. A. Evans, M. Bhul, Reduced order controller for distributed parameter systems: LQG balanced truncation and an adaptive approach, *Mathematical and Computer Modeling* 43 (2006) 1136-1149.

[158] J. Zarei, A. Montazeri, M R. J. Motlagh, J. Poshtan, Design and comparison of LQG/LTR and H_∞ controllers for a VSTOL flight control system, *Journal of Franklin Institute* 344 (2007) 577-594.

[159] C-C Ho, C-K Ma, Active vibration control of structural systems by a combination of the Linear Quadratic Gaussian and input estimation approaches, *Journal of Sound and Vibration* 301 (2007) 429-449.

[160] G. Kirchhoff, Uber das gleichgewicht and die bewegung einer elastischen scheibe. *Journal f'ur reine and angewandte Mathematik* 40 (1850) 51–88.

[161] V. Z. Vlasov, General Shell Theory and Its Technological Applications [in Russian],Gostekhizdat, Moscow-Leningrad, 1949.

[162] K. Z. Galimov, General theory of elastic shells with finite displacements, Izv. KFAN SSSR, Ser. Fiz. Mat. Tekh. Nauk, No. 2, 1950, 3-38.

[163] W. T. Koiter, Current trends in the theory of buckling, in: Buckling Structure,Berlin, 1976, 1-16.

[164] Kh. M. Mushtari and K. Z. Galimov, Nonlinear Theory of Elastic Shells [in Russian],Tatknigoisdat, Kazan, 1957.

[165] J. N Reddy, Exact solutions of moderately Thick Laminated Shells, *Journal of engineering mechanics*, ASCE 110(5) (1985) 794-809.

[166] J. H. Holland, Adaptation in Natural and Artificial Systems, The University of Michigan Press, Ann Arbor, MI, 1975.

[167] K. A. D. Jong, An Analysis of the Behavior of a Class of Genetic Adaptive Systems. PhD thesis, University of Michigan, Ann Arbor, MI. Deptartment of Computer and Communication Sciences, 1975

[168] D. E. Goldberg, Genetic Algorithms in Search, Optimization, and Machine Learning. Addison-Wesley, Reading, MA, 1989.

[169] J. E. Potter, Matrix quadratic solutions, *SIAM J. Appl. Math.* 14 (1966) 496–501.

[170] F. L. Lewis, Optimal control, Wiley, New York, 1986.

[171] J.C. Bruch, J.M. Sloss, I.S. Sadek, Optimal piezo-actuator locations/lengths and applied voltage for shape control of beams, *Smart Mater. Struct.* 9 (2002) 205-211.

[172] K. Deb, S. Gulati, Design of truss-structures for minimum weight using genetic algorithms, *Finite Elements in Analysis and Design* 37 (2001) 447-465.

[173] K. Deb, S. Kartick, T. Okabe, Self-Adaptive Simulated Binary Crossover for Real Parameter Optimization, *GECCO'07,* London, UK, 2007, 1187-1194.

[174] J. N. Reddy, C. F. Liu, A higher-order Shear Deformation theory of Laminated Elastic Shells, *International Journal of Engg. Science* 23(3) (1985) 319-330.

[175] J G Smits, S. I. Dalke, T. K. Cooney, The constituent equations of piezoelectric bimorphs, *Sensors and Actuators A* 28 (1991) 41-61.

[176] L. Meirovitch, Dynamics and control of structures, Singapore, Wiley, (1992).

[177] K. J. Bathe, Finite Element Procedures, New Jersey, Prentice Hall Inc., (1996).

APPENDIX

1. Displacement, Strain and Stress vectors

The degrees of freedom for i^{th} node on the midsurface of shell element

$$\{d_i\} = [u_{0i} \quad v_{0i} \quad w_i \quad \theta_{1i} \quad \theta_{2i}]^T \tag{A.1}$$

Total degrees of freedom for an 8 noded element

$$\{d^e\} = \left[\{d_1\}^T \quad \{d_2\}^T \quad \{d_3\}^T \quad \{d_4\}^T \quad \{d_5\}^T \quad \{d_6\}^T \quad \{d_7\}^T \quad \{d_8\}^T\right]^T \tag{A.2}$$

The stress components in material principal coordinate system

$$\{\sigma\}^{(12)} = [\sigma_{11} \quad \sigma_{22} \quad \tau_{12}]^T \tag{A.3}$$

$$\{\tau\}^{(123)} = [\tau_{23} \quad \tau_{13}]^T \tag{A.4}$$

The strain components in material principal coordinate system

$$\{\varepsilon\}^{(12)} = [\varepsilon_{11} \quad \varepsilon_{22} \quad \gamma_{12}]^T \tag{A.5}$$

$$\{\gamma\}^{(123)} = [\gamma_{23} \quad \gamma_{13}]^T \tag{A.6}$$

The stress components in global coordinate system

$$\{\sigma\}^{(xy)} = \left[\sigma_{xx} \quad \sigma_{yy} \quad \tau_{xy}\right]^T \tag{A.7}$$

$$\{\tau\}^{(xyz)} = \left[\tau_{yz} \quad \tau_{xz}\right]^T \tag{A.8}$$

The strain components in global coordinate system

$$\{\varepsilon\}^{(xy)} = \left[\varepsilon_{xx} \quad \varepsilon_{yy} \quad \gamma_{xy}\right]^T \tag{A.9}$$

$$\{\gamma\}^{(xyz)} = \left[\gamma_{yz} \quad \gamma_{xz}\right]^T \tag{A.10}$$

The stress-strain relationship in material principal coordinates system

$$\{\sigma\}^{(12)} = [Q_b]\{\varepsilon\}^{(12)} \tag{A.11}$$

$$\{\tau\}^{(123)} = [Q_S]\{\gamma\}^{(123)} \tag{A.12}$$

The stress-strain relationship in global coordinate system

$$\{\sigma\}^{(xy)} = \left[\overline{Q_b}\right]\{\varepsilon\}^{(xy)} \tag{A.13}$$

$$\{\tau\}^{(xyz)} = \left[\overline{Q}_S\right]\{\gamma\}^{(xyz)} \tag{A.14}$$

2. In-plane/bending stiffness matrix

$$\left[K_{bb}^{e}\right]=\int_{V}\left[B_{b}^{e}\right]^{T}\left[D_{b}\right]\left[B_{b}^{e}\right]dV$$

$$=\int_{\Omega}\left[B_{b}^{e}\right]^{T}\begin{bmatrix}[A] & [B]\\ [B] & [D]\end{bmatrix}\left[B_{b}^{e}\right]d\Omega \tag{A.15}$$

2.1. ABBD matrix

The resultant force per unit width is

$$\{N\}=\begin{bmatrix}N_{xx} & N_{yy} & N_{xy}\end{bmatrix}^{T} \tag{A.16}$$

The resultant moment per unit width is

$$\{M\}=\begin{bmatrix}M_{xx} & M_{yy} & M_{xy}\end{bmatrix}^{T} \tag{A.17}$$

In plane strains of mid-surface is

$$\{\varepsilon^{0}\}=\begin{bmatrix}\varepsilon_{xx}^{0} & \varepsilon_{yy}^{0} & \gamma_{xy}^{0}\end{bmatrix}^{T} \tag{A.18}$$

Curvatures of mid-surface is

$$\{k\}=\begin{bmatrix}k_{xx} & k_{yy} & k_{xy}\end{bmatrix}^{T} \tag{A.19}$$

The strain at any point on an element

$$\{\varepsilon\}^{(xy)}=\{\varepsilon^{0}\}+z\{k\} \tag{A.20}$$

The resultant force per unit width can be expressed as

$$\{N\}=\int_{-h/2}^{h/2}\{\sigma\}^{(xy)}dz$$

$$=[A]\{\varepsilon^{0}\}+[B]\{k\} \tag{A.21}$$

The resultant moment per unit width

$$\{M\}=\int_{-h/2}^{h/2}\{\sigma\}^{(xy)}zdz$$

$$=[B]\{\varepsilon^{0}\}+[D]\{k\} \tag{A.22}$$

Eqs. (A21) and (A22) can be expressed in matrix form as

$$\begin{Bmatrix}\{N\}\\ \{M\}\end{Bmatrix}=\begin{bmatrix}[A] & [B]\\ [B] & [D]\end{bmatrix}\begin{Bmatrix}\{\varepsilon^{0}\}\\ \{k\}\end{Bmatrix} \tag{A.23}$$

$$\{\sigma\} = \begin{bmatrix} [A] & [B] \\ [B] & [D] \end{bmatrix} \{\varepsilon\} \tag{A.24}$$

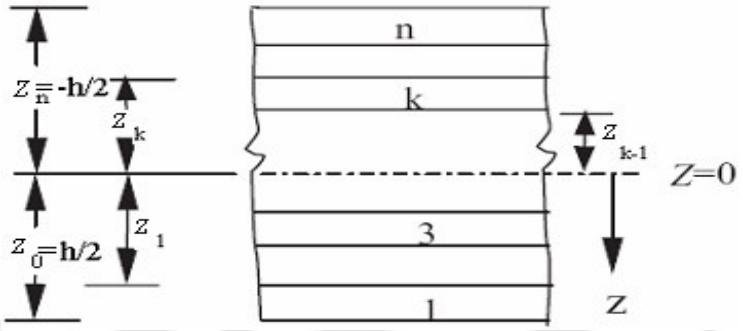

Fig.A.1.The stacking of laminas in the laminate

The extensional stiffness matrix

$$[A] = \sum_{k=1}^{n} \left[\overline{Q_b}\right]_k (Z_k - Z_{k-1}) \tag{A.25}$$

The extensional-bending coupling stiffness matrix

$$[B] = \frac{1}{2} \sum_{k=1}^{n} \left[\overline{Q_b}\right]_k \left(Z_k^2 - Z_{k-1}^2\right) \tag{A.26}$$

The bending stiffness matrix

$$[D] = \frac{1}{3} \sum_{k=1}^{n} \left[\overline{Q_b}\right]_k \left(Z_k^3 - Z_{k-1}^3\right) \tag{A.27}$$

The transformed elasticity matrix for bending

$$\left[\overline{Q_b}\right]_k = [R_T]_k^{-1} [Q_b]_k [R_T]_k^{-T} \tag{A.28}$$

The transformation matrix

$$[R_T]_k^{-1} = \begin{bmatrix} \cos^2\theta & \sin^2\theta & -2\sin\theta\cos\theta \\ \sin^2\theta & \cos^2\theta & 2\sin\theta\cos\theta \\ \sin\theta\cos\theta & -\sin\theta\cos\theta & \cos^2\theta - \sin^2\theta \end{bmatrix} \tag{A.29}$$

$$[R_T]_k^{-T} = \begin{bmatrix} \cos^2\theta & \sin^2\theta & \sin\theta\cos\theta \\ \sin^2\theta & \cos^2\theta & -\sin\theta\cos\theta \\ -2\sin\theta\cos\theta & 2\sin\theta\cos\theta & \cos^2\theta - \sin^2\theta \end{bmatrix} \tag{A.30}$$

The elasticity matrix in material principal coordinate system

$$[Q_b]_k = \begin{bmatrix} Q_{11} & Q_{12} & 0 \\ Q_{12} & Q_{22} & 0 \\ 0 & 0 & Q_{66} \end{bmatrix} \tag{A.31}$$

$$Q_{11} = \frac{E_1}{1-\nu_{12}\nu_{21}}, Q_{22} = \frac{E_2}{1-\nu_{12}\nu_{21}}$$

$$Q_{12} = \frac{\nu_{12}E_2}{1-\nu_{12}\nu_{21}} = \frac{\nu_{21}E_1}{1-\nu_{12}\nu_{21}}, \quad Q_{66} = G_{12}, \quad \frac{\nu_{12}}{E_1} = \frac{\nu_{21}}{E_2}$$

$$\nu_{12} = -\varepsilon_2 / \varepsilon_1, \quad \nu_{21} = -\varepsilon_1 / \varepsilon_2$$

3. Transverse shear stiffness matrix

The transverse shear stiffness matrix

$$\left[K_{ss}^e\right] = \int_V \left[B_s^e\right]^T [D_s] \left[B_s^e\right] dV$$

$$= \int_\Omega \left[B_s^e\right]^T \left[\overline{D}_s\right] \left[B_s^e\right] d\Omega \tag{A.32}$$

3.1. Transverse shear constitutive matrix

The resultant shear force per unit width is

$$\begin{Bmatrix} N_{yz} \\ N_{xz} \end{Bmatrix} = \int_{-h/2}^{h/2} \begin{Bmatrix} \sigma_{yz} \\ \sigma_{xz} \end{Bmatrix} dz$$

$$= \left[\overline{D}_s\right] \begin{Bmatrix} \gamma_{yz} \\ \gamma_{xz} \end{Bmatrix}$$

$$\left[\overline{D}_s\right] = \sum_{k=1}^{n} \left[\overline{Q}_s\right] (Z_k - Z_{k-1}) \tag{A.33}$$

The transformed elasticity matrix for transverse shear

$$\left[\overline{Q}_s\right] = [R_s]^T [Q_S][R_s] \tag{A.34}$$

The elasticity matrix in material principal material coordinate system

$$[Q_S] = \begin{bmatrix} KG_{23} & 0 \\ 0 & KG_{13} \end{bmatrix} \tag{A.35}$$

Where K denotes shear correction factor

The transformation matrix

$$[R_s] = \begin{bmatrix} \cos\theta & -\sin\theta \\ \sin\theta & \cos\theta \end{bmatrix} \tag{A.36}$$

4. Electromechanical coupling stiffness matrix

The Electromechanical coupling stiffness matrix is

$$\left[K_{u\phi}^{e}\right]=\int_{V_p}\left[B_u^e\right]^T[e]^T\left[B_\phi^e\right]dV_p$$

$$=\int_{\Omega}\left[B_u^e\right]^T\left[D_{u\phi}\right]d\Omega \qquad \text{(A.37)}$$

where $\left[B_u^e\right]=\begin{bmatrix}\left[B_b^e\right]\\ \left[B_s^e\right]\end{bmatrix}$

Since two kinds of electrical approximations are implemented in this work, the matrix $\left[D_{u\phi}\right]$ is different for different kind of electrical approximations. The matrix $\left[D_{u\phi}\right]$ for different electrical approximations is given below.

i. Electrical potential varies linearly in the thickness direction and only one electrical degree of freedom is taken for each piezo layer.

The resultant force per unit width due to the electromechanical coupling can be expressed as

$$\begin{Bmatrix}N\\ M\\ \tau\end{Bmatrix}=\sum_{k=1}^{nl}\begin{bmatrix}\{\bar{e}\}_k\\ h_{mk}\{\bar{e}\}_k\\ \{0\}\end{bmatrix}\phi_k$$

$$=\left[D_{u\phi}\right]\{\phi\} \qquad \text{(A.38)}$$

where

$$h_{mk}=\frac{h_k+h_{k-1}}{2} \quad \text{and} \quad \{\phi\}=\begin{bmatrix}\phi_1 & \phi_2 & \dots & \phi_{nl}\end{bmatrix}^T$$

ϕ_1 is the electrical potential for the first piezo layer, ϕ_2 is the electrical potential for the second piezo layer and so on. The transformed electromechanical coupling coefficient of k^{th} layer is given as

$$\{\bar{e}\}_k=\left[R_T\right]_k^{-1}\begin{Bmatrix}e_{31}\\ e_{32}\\ 0\end{Bmatrix}_k \qquad \text{(A.39)}$$

where e_{31} and e_{32} are the in plane mode piezoelectric coefficients of k^{th} layer in principle coordinates.

ii. Electrical potential varies linearly in the thickness direction and the elemental electrical degree of freedom is considered. The resultant force per unit width due to the electromechanical coupling for i^{th} element can be expressed as

$$\begin{Bmatrix} N \\ M \\ \tau \end{Bmatrix}^i = \sum_{k=1}^{nl} \begin{bmatrix} \{\bar{e}\}_k^i \\ h_{mk}^i \{\bar{e}\}_k^i \\ \{0\} \end{bmatrix} \phi_k^i$$

$$= \left[D_{u\phi}^i \right] \{\phi^i\} \qquad \text{(A.40)}$$

ϕ_1^i is the electrical potential difference for the first layer of i^{th} element, ϕ_2^i is the electrical potential difference for the second layer of i^{th} element and so on. The transformed electromechanical coupling coefficient of k^{th} layer of i^{th} element can be expressed as

$$\{\bar{e}\}_k^i = [R_T]_k^{-1} \begin{Bmatrix} e_{31} \\ e_{32} \\ 0 \end{Bmatrix}_k^i \qquad \text{(A.41)}$$

The transformation matrix for all above three cases is

$$[R_T]_k^{-1} = \begin{bmatrix} \cos^2\theta & \sin^2\theta & -2\sin\theta\cos\theta \\ \sin^2\theta & \cos^2\theta & 2\sin\theta\cos\theta \\ \sin\theta\cos\theta & -\sin\theta\cos\theta & \cos^2\theta - \sin^2\theta \end{bmatrix} \qquad \text{(A.42)}$$

θ is the angle of orientation of k^{th} layer

5. Dielectric stiffness matrix

The permittivity stiffness matrix is given as

$$\left[K_{\phi\phi}^e \right] = -\int_{V_p} \left[B_\phi^e \right]^T [\in] \left[B_\phi^e \right] dV_p$$

$$= -\int_{\Omega} \left[D_{\phi\phi} \right] d\Omega \qquad \text{(A.43)}$$

Since three kinds of electrical approximations are implemented in this work, the matrix $\left[D_{\phi\phi} \right]$ is different for different kind of electrical approximations. The matrix $\left[D_{\phi\phi} \right]$ for different electrical approximations is given below.

i. Electrical potential varies linearly in the thickness direction and only one electrical degree of freedom is taken for each piezo layer.

$$\left[D_{\phi\phi}\right]=\begin{bmatrix} \in_{31}/h_1 & 0 & \cdots & 0 \\ 0 & \in_{32}/h_2 & \cdots & 0 \\ \vdots & \vdots & \ddots & \vdots \\ 0 & 0 & \cdots & \in_{3nl}/h_{nl} \end{bmatrix} \tag{A.44}$$

where $\in_{31}$ is the dielectric permittivity of the first piezo layer, $\in_{32}$ is the is the dielectric permittivity of the second piezo layer and so on. h_{nl} is the thickness of nl^{th} piezo layer.

ii. Electrical potential varies linearly in the thickness direction and the elemental electrical degree of freedom is considered.

$$\left[D^i_{\phi\phi}\right]=\begin{bmatrix} \in^i_{31}/h^i_1 & 0 & \cdots & 0 \\ 0 & \in^i_{32}/h^i_2 & \cdots & 0 \\ \vdots & \vdots & \ddots & \vdots \\ 0 & 0 & \cdots & \in^i_{3nl}/h^i_{nl} \end{bmatrix} \tag{A.45}$$

where $\in^i_{31}$ is the dielectric permittivity of the first layer of i^{th} element, $\in^i_{32}$ is the dielectric permittivity of the second layer of i^{th} element and so on. h^i_{nl} is thickness of nl^{th} layer.

6. Thermoelastic stiffness matrix

Thermoelastic stiffness matrix is given as

$$\left[K^e_{ut}\right]=\int_V\left[B^e_u\right]^T\{\lambda\}\left[N^e_t\right]dV$$

$$=\int_\Omega\left[B^e_u\right]^T\left[D_{ut}\right]d\Omega \tag{A.46}$$

where $\left[B^e_u\right]=\begin{bmatrix}\left[B^e_b\right]\\ \left[B^e_s\right]\end{bmatrix}$ is the strain displacement matrix. Since two kinds of temperature variation are implemented in this work, the matrix $\left[D_{ut}\right]$ is different for different kind of temperature variation. The matrices $\left[D_{ut}\right]$ for different temperature variation are given below.

1. Linear temperature variation is considered in the thickness direction of laminate and only two thermal degrees of freedom are considered for whole laminate. One is temperature on top surface of laminate and another one is the temperature on bottom surface of laminate.

   The resultant force per unit width due to the thermal strain for whole laminate can be expressed as

$$\begin{Bmatrix} N \\ M \\ \tau \end{Bmatrix} = \sum_{k=1}^{nl} \int_{z_k}^{z_{k+1}} \begin{bmatrix} \{\bar{\lambda}\}_k \\ z\{\bar{\lambda}\}_k \\ \{0\} \end{bmatrix} t(z)dz$$

$$= \sum_{k=1}^{nl} \int_{z_k}^{z_{k+1}} \begin{bmatrix} \{\bar{\lambda}\}_k \\ z\{\bar{\lambda}\}_k \\ \{0\} \end{bmatrix} \lfloor N_t \rfloor dz\{t\}$$

$$= [D_{ut}]\{t\} \qquad \text{(A.47)}$$

   where $\{t\} = \begin{Bmatrix} t_t \\ t_b \end{Bmatrix}$ and $\lfloor N_t \rfloor = \begin{bmatrix} \frac{1}{2} - \frac{z}{h} & \frac{1}{2} + \frac{z}{h} \end{bmatrix}$

   t_t and t_b are temperatures on top and bottom surface of laminate, respectively and h is the thickness of laminate and subscript k defines the layer.

   Transformed temperature stress coefficient $\{\bar{\lambda}\}_k = [\bar{Q}]_k \{\bar{\alpha}\}_k$

   Transformed coefficient of thermal expansion $\{\bar{\alpha}\}_k = [R][T]_k^{-1}\{\alpha\}_k$

   Coefficient of thermal expansion along principal directions $\{\alpha\}_k = [\alpha_1 \quad \alpha_2 \quad 0]_k^T$

   Transformed inplane elastic stiffness matrix $[\bar{Q}]_k = [T]_k^{-1}[Q]_k[R][T]_k[R]^{-1}$

   Inplane elastic stiffness matrix: $[Q]_k = \begin{bmatrix} Q_{11} & Q_{12} & 0 \\ Q_{12} & Q_{22} & 0 \\ 0 & 0 & Q_{66} \end{bmatrix}$

2. Linear temperature variation is considered in the thickness direction of laminate and two thermal degrees of freedom are considered for every element. One is the temperature on top surface of an element and another one is the temperature on bottom surface of an element.

The resultant force per unit width due to the thermal strain for an i^{th} element can be expressed as

$$\begin{Bmatrix} N \\ M \\ \tau \end{Bmatrix}^i = \sum_{k=1}^{nl} \int_{z_k}^{z_{k+1}} \begin{bmatrix} \{\bar{\lambda}\}_k^i \\ z\{\bar{\lambda}\}_k^i \\ \{0\} \end{bmatrix} t^i(z)dz$$

$$= \sum_{k=1}^{nl} \int_{z_k}^{z_{k+1}} \begin{bmatrix} \{\bar{\lambda}\}_k^i \\ z\{\bar{\lambda}\}_k^i \\ \{0\} \end{bmatrix} \lfloor N_t \rfloor^i dz \{t\}^i$$

$$= [D_{ut}]^i \{t\}^i \qquad \text{(A.48)}$$

where $\{t\} = \begin{Bmatrix} t_t^i \\ t_b^i \end{Bmatrix}$ and $\lfloor N_t \rfloor^i = \begin{bmatrix} \frac{1}{2} - \frac{z}{h^i} & \frac{1}{2} + \frac{z}{h^i} \end{bmatrix}$

t_t^i and t_b^i are temperatures on top and bottom surface of i^{th} element, respectively, h^i, is the thickness of i^{th} element, subscript k defines the layer number and the superscript i defines the element number.

Transformed temperature stress coefficient $\{\bar{\lambda}\}_k^i = [\bar{Q}]_k^i \{\bar{\alpha}\}_k^i$

Transformed coefficient of thermal expansion $\{\bar{\alpha}\}_k^i = [R][T]_k^{-1} \{\alpha\}_k^i$

Coefficient of thermal expansion along principal directions $\{\alpha\}_k^i = [\alpha_1 \quad \alpha_2 \quad 0]_k^T$

Transformed inplane elastic stiffness matrix: $[\bar{Q}]_k^i = [T]_k^{-1} [Q]_k^i [R][T]_k [R]^{-1}$

Inplane elastic stiffness matrix: $[Q]_k^i = \begin{bmatrix} Q_{11} & Q_{12} & 0 \\ Q_{12} & Q_{22} & 0 \\ 0 & 0 & Q_{66} \end{bmatrix}$

Rotational matrix is $[T]_k^{-1}$ and Matrix $[R] = \begin{bmatrix} 1 & 0 & 0 \\ 0 & 1 & 0 \\ 0 & 0 & 2 \end{bmatrix}$

7. Structural Mass matrix

The structural mass matrix is given as

$$\left[M_{uu}^{e}\right]=\int_{V}\rho[N]^{T}[N]dV \tag{A.49}$$

The displacement at any point in the laminate cane be expressed as

$$\begin{Bmatrix}u\\v\\w\end{Bmatrix}=\begin{Bmatrix}u_0-z\theta_x\\v_0-z\theta_y\\w\end{Bmatrix}$$

$$=\sum_{i=1}^{nd}\begin{bmatrix}N_i & 0 & 0 & -zN_i & 0\\0 & N_i & 0 & 0 & -zN_i\\0 & 0 & N_i & 0 & 0\end{bmatrix}\begin{Bmatrix}u_{0i}\\v_{0i}\\w_i\\\theta_{xi}\\\theta_{yi}\end{Bmatrix}$$

$$=[N]\{d^{e}\}$$

$$\left[M_{uu}^{e}\right]=\int_{V}\rho[N]^{T}[N]dV$$

$$=\int_{\Omega}\int_{-h/2}^{h/2}\rho[N]^{T}[N]dzd\Omega \tag{A.50}$$

8. Transformation matrix used for isoparametric mapping

Since the integration is to be done in natural coordinates (ξ,η), the element is mapped into the isoparametric space (ξ,η) using the isoparametric shape functions. The transformation matrix used is given below. In Koiter's shell theory formulation the curvilinear coordinate (α_1,α_2) is mapped into isoparametric space (ξ,η) and any point within an element in the parametric space can be approximated as

$$\alpha_1=\sum_{i=1}^{nd}N_i\alpha_{1i}$$
$$\alpha_2=\sum_{i=1}^{nd}N_i\alpha_{2i} \tag{A.51}$$

The relation between the shape function derivatives in parametric space (α_1,α_2) and in isoparametric space (ξ,η) are given as

$$\begin{Bmatrix} \frac{\partial N_i}{\partial \alpha_1} \\ \frac{\partial N_i}{\partial \alpha_2} \end{Bmatrix} = \left[J^* \right]^{-1} \begin{Bmatrix} \frac{\partial N_i}{\partial \xi} \\ \frac{\partial N_i}{\partial \eta} \end{Bmatrix} \tag{A.52}$$

The jacobian matrix can be expressed as

$$\left[J^* \right] = \begin{bmatrix} \frac{\partial \alpha_1}{\partial \xi} & \frac{\partial \alpha_2}{\partial \xi} \\ \frac{\partial \alpha_1}{\partial \eta} & \frac{\partial \alpha_2}{\partial \eta} \end{bmatrix}$$

$$|J| = \sqrt{a}\,|J^*|$$

$$d\Omega = |J|\,d\xi d\eta$$

Hence all the element stiffness matrices can be expressed in its final form as

$$\left[K^e \right] = \int_{-1}^{1}\int_{-1}^{1} [K_h]\,|J|\,d\xi d\eta \tag{A.53}$$

Mass matrix in its final form can be expressed as

$$\left[M_{uu}^{e} \right] = \int_{-1}^{1}\int_{-1}^{1}\int_{-h/2}^{h/2} \rho [N]^T [N]\,dz\,|J|\,d\xi d\eta \tag{A.54}$$

9. Parametric equations

The parametric equations used for the mapping of global coordinate of midsurface of shell into curvilinear coordinate are given below.

$$\begin{aligned} x &= r_1 \sin\theta \sin\phi \\ y &= r_2 \cos\phi \\ z &= r_3 \cos\theta \sin\phi \end{aligned} \tag{A.55}$$

where,

$2r_1$ is the major axis length

$2r_2$ is the minor axis length

r_3 is the polar radius along z axis

θ, ϕ denotes the angles of revolution of shell panel.

The parametric equation for spherical surface is given as

$$x = r \sin\theta \sin\phi$$
$$y = r \cos\phi \qquad \text{(A.56)}$$
$$z = r \cos\theta \sin\phi$$

where r is the radius of sphere.

List of Publications from this Ph.D Thesis Work

1. Tarapada Roy and Debabrata Chakraborty, GA-LQR based Optimal Vibration Control of Smart FRP Composite Structures with bonded PZT patches, *Journal of Reinforced Plastics and Composites* Vol.28 No.11 (2009) 1383-1404

2. Tarapada Roy and Debabrata Chakraborty**,** Optimal Vibration Control of Smart Fiber Reinforced Composite Shell Structures using Improved Genetic Algorithm, *Journal of Sound and Vibration* 319 (1-2) (2009) 15-40.

3. Tarapada Roy and Debabrata Chakraborty, Genetic algorithm based optimal design for vibration control of composite shell structures using piezoelectric sensors and actuators, *International Journal of Mechanics and Materials in Design* 5 (1) (2009) 45-60.

4. Tarapada Roy, Debabrata Chakraborty and Rama Krishna Tammireddy, Optimal Vibration Control of Curved Smart FRP Composite Structures using GA based LQR, *Aerospace Science and Technology* (Under Review).

5. Tarapada Roy and Debabrata Chakraborty, Genetic algorithm based optimal vibration control of smart fiber reinforced composite shell structures under thermo-mechanical loading, *Smart Materials and Structures* (Under Review).

6. Tarapada Roy and Debabrata Chakraborty, Improved Shell Finite Element for Piezothermoelastic Analysis of Smart Fiber Reinforced Composite Structures, *Finite Elements in Analysis and Design* (Under Review).

7. Tarapada Roy and Debabrata Chakraborty, Optimal Vibration Control of Smart Composite Shell Structures, *International Conference on Smart Materials, Structures and Systems,* IISc Bangalore, India, 2008 (Accepted).

8. Tarapada Roy and Debabrata Chakraborty, Optimal Placement of Piezoelectric Actuators on the Curved Smart FRP Composites Structures using Integer Coded Genetic Algorithm, *International Conference on Aerospace Sciences and Technology*, National Aerospace Laboratory, Bangalore, India, 2008 (Accepted).

9. Tarapada Roy and Debabrata Chakraborty, LQG based Vibration Control of Curved Smart FRP Composite Structures, *International Conference on Theoretical Applied Computational and Experimental Mechanics (ICTACEM)*, IIT Kharagpur, India, 2007.

10. Tarapada Roy and Debabrata Chakraborty, Optimal Vibration Control of Smart FRP Composite Structures using GA and LQR, *Indian Society of Theoretical & Applied Mechanics (An International meet)*, B.N.M Institute of Technology, Bangalore, India, 2007.

11. Tarapada Roy, M. Mastan Pasa and D. Chakraborty, 3D Layered Finite Element for Modeling and Control of Smart FRP structures, *2nd International Congress on Computational Mechanics and Simulation (ICCMS),* IIT Guwahati, India, 2006.

V I T A

Mr Tarapada Roy was born to Mr Bhairab Ch Roy and Mrs Parul Roy in the year 1978 in Bankura district of West Bengal. He completed his class X and class XII from WBSEB and WBHSEB respectively in 1995 and 1997 securing first division in both. He completed his Bachelor of Engineering in Mechanical Engineering in 2002 and Master of Engineering in Solid Mechanics in 2004 both from Bengal Engineering College (Deemed University), Shibpur, West Bengal securing first class in both the examinations. He joined the PhD program in Mechanical Engineering Department of Indian Institute of Technology Guwahati in July 2004 and submitted the PhD Thesis in March 2009. His area of research interests is active vibration control of composite structures. Currently, he is working as a Lecturer in Mechanical Engineering Department at NIT Rourkela, Orissa.